UNIVERSITY OF OKLAHOMA

GRADUATE COLLEGE

Impacts of tropopause polar vortices on Arctic sea ice loss

A DISSERTATION

SUBMITTED TO THE GRADUATE FACULTY

in partial fulfillment of the requirements for the

Degree of

DOCTOR OF PHILOSOPHY

By

NICHOLAS SZAPIRO
Norman, Oklahoma
2019

Impacts of tropopause polar vortices on Arctic sea ice loss

A DISSERTATION APPROVED FOR THE
SCHOOL OF METEOROLOGY

BY

Dr. Steven Cavallo, Chair

Dr. Ronald Barnes

Dr. Jennifer Kay

Dr. Elinor Martin

Dr. Dave Parsons

Dr. David Turner

Dedication

To the reader,

Standing together we are all giants.

Acknowledgments

Our world and my family are my foundations. My sister is a medical doctor, like my mother. I followed my father into the physical sciences. The love, support, lessons, and experiences we have shared can never be repaid, only paid forward. Steven Cavallo is my academic father. He has guided and trained me from a CFD engineer to an employed Earth system scientist with respect, vision, rigor, kindness, and generosity. To my life partner Ana Raquel, thank you for joining our lives as we heal, grow, and build wherever the future holds. Life with the AaARG research group, graduate students, faculty, and staff in the University of Oklahoma School of Meteorology has given me a friendly, supportive, responsive, and eccentric community of peers. Grillfests are an institution. Chris Riedel ran the WRF limited-area simulations in Sect. 2.3.3.1. The MPAS group at NCAR MMM provided helpful discussions and software support, in particular Michael Duda for help with debugging, implementation of potential vorticity diagnostics, and MPAS-A within CESM along with Sang-Hun Park. Bill Skamarock discussed and edited content included in Ch. 2 and Ch. 3. All committee members have provided constructive feedback and challenged me with the best of intentions.

Primary funding has been under Office of Naval Research award N00014-15-1-2220. Additional funding for conference travel was provided by the University of Oklahoma graduate college. High-performance computing support for Yellowstone (`ark:/85065/d7wd3xhc`) and Cheyenne (`doi:10.5065/D6RX99HX`) was provided by NCAR's Computational and Information Systems Laboratory, sponsored by the National Science Foundation.

Thank you all.

Table of Contents

List of Tables

List of Figures

Abstract

The Arctic and sea ice cover play fundamental roles in the environment of the Earth system. Improved causal understanding of their changes is needed for meaningful predictions and planning. Among the linkages composing our understanding and predictions, hypothesized mechanisms and historical cases suggest that potentially long-lived, (sub-)synoptic coherent circulation features termed tropopause polar vortices (TPVs) can impact the evolution of Arctic sea ice on daily to seasonal time scales. Diagnostics and causal dynamical experiments are developed to evaluate whether there are mechanisms sufficient for TPVs to significantly impact Arctic summer sea ice loss.

A TPV's place, structure, and history are intimately related to its dynamics and associated impacts. A restricted regional watershed segmentation and major correspondence overlap TPV tracking method more robustly defines tracked TPVs' spatial structure (through restricted regional watershed basins with variable shapes and intensities) and time evolution (through similarity overlap with mergers and splits) relative to previous methods. Tracking with a more restrictive definition of lifetime and more robust, variable size, individual cyclonic TPVs can exceed radii of 1000 km, amplitudes of 40 K, and lifetimes of 2 months, coincide with multi-day extreme sea ice loss, and contribute seasonal-scale geographic anomalies.

To represent the potential, integrated impacts of TPVs on Arctic sea ice, it is argued that a comprehensive model should resolve TPVs and feedbacks with the larger polar circulation, consistently couple and realistically evolve sea ice, and be computationally tractable. Motivated by limitations in limited-area and coarser general circulation models to satisfy these requirements, the Model for Predictions Across Scales non-hydrostatic atmospheric dynamical core is embedded within the Community Atmospheric Model of the Community Earth System Model (CESM-CAM-MPAS). A global, Arctic-refined atmospheric configuration efficiently provides needed local resolution to TPVs with two-way feedbacks to the polar circulation. Coupling with an Earth system model evolves sea ice

through process-based exchanges. With mixed historical and analog initial conditions intended to balance considerations of realism and consistency, summer simulations capture mean polar circulation anomalies and yield competitive September sea ice extent forecasts with skill for the sea ice edge. An effective, localized tendency-based modification strategy permits sensitivity experiments to quantify causal responses throughout the Earth system to input TPV perturbations.

Sensitivity experiments are conducted with directly modified TPV intensity within the coupled Earth system to causally explore and evaluate whether TPVs can have extreme sea ice impacts. Strong intensification of cyclonic TPVs in the Arctic can cause less summer sea ice loss. Multi-scale, thermodynamic, mechanical, and multi-component mechanisms contribute to differences in sea ice mass, momentum, and energy, with reduced upward surface ocean heat fluxes the largest of the factors associated with maintaining ice cover. The artificial intensification sufficient to realize sensitivity beyond expectations from historical and internal variability in individual simulations of July through September 2006 is near -5 K d^{-1}. Larger than composite mean diabatic heating rates in TPVs, operational forecasts can exhibit initial forecast errors in TPV intensification of the same order.

Since large errors in individual vortices can change the trajectory of fundamental components of the simulated Earth system, characteristics and roles of TPV shape and place and integrated atmosphere-sea ice-ocean coupling emerge as important factors for linkages and predictions. Multi-scale, coupled system models offer one class of approaches that can provide qualitative depictions, quantitative sensitivities, and dynamical insights into relationships throughout the Earth system. The aggregated work motivates directions for future process and prediction studies.

Chapter 1

Introduction

Situated in the remote, extreme north of our planet, the Arctic plays important roles in Earth's energy (e.g., Gautier et al. (2009); Porter et al. (2010)), mass (e.g., Enderlin et al. (2014); Christiansen et al. (2014)) and momentum (e.g., Mauritzen and Häkkinen (1997)) budgets. Improving our limited understanding of the Arctic is essential for sustainable management of our resources (Reigstad et al. 2017). In a region experiencing amplified climate change (Serreze and Barry 2011), these limitations project onto native life, tourism, shipping, fishing, oil exploration, and lower latitude weather (e.g., Grebmeier et al. (2010); Lovecraft (2013); Meier et al. (2014); Overland et al. (2015); Melia et al. (2016); Crépin et al. (2017)). Furthered knowledge and improved predictions are expected from enhanced observations, more accurate model representation of key polar processes, refined data assimilation, and furthered understanding of linkages between the Arctic and lower latitudes (Jung et al. 2016).

Sea ice is a fundamental component of the Arctic. Its prediction has been labelled "a grand challenge of climate science" (Kattsov et al. 2010) with variability and impacts highlighted at its margins. Temporal variability of sea ice concentration is greatest along the time-mean sea ice edge (Fang and Wallace 1994). In the transition from the denser inner ice pack to the open ocean lies the seasonally varying marginal ice zone (e.g., Muench et al. (1983); Strong et al. (2017)). The transition region is dynamically important in both weather and climate with intense air–sea interactions (e.g., Rasmussen (1985)) and contrasts of fluxes associated with the bright, insulating ice cover to the dark, warmer open ocean (e.g., Maykut (1978)). The practical importance of the sea ice edge extends further, including constraining navigation (e.g., Mercator (1595); Nansen (1897); Greenert (2014))

and modulating conditions and nutrients in the ecosystem (e.g., Sutherland (1852); Melnikov (1997); Arrigo et al. (2012)).

Fundamental to improving our understanding, predictions, and projections of sea ice change are furthering our understanding of the driving variability and attribution of causes (Kattsov et al. 2010). Sect. 1.1 introduces background on characteristics of sea ice and examples of regimes of changes. Atmospheric forcing is both a driver of sea ice variability and limiter of predictability (e.g., Serreze and Stroeve (2015)). With potential to influence both, focus herein centers on coherent near-tropopause features termed tropopause polar vortices and their roles among the linkages (Sect. 1.2). For attribution among a panoply of interactions, the concept of causation can be usefully split into three questions (Barnes and Screen 2015): can X influence Y? Has X influenced Y? Will X influence Y? To contribute to a causal understanding of the driving variability of sea ice cover, a central question guides this work: to what degree and through what mechanisms can coherent near-tropopause features termed tropopause polar vortices impact variability of Arctic sea ice?

1.1 Overview of sea ice change

As described in National Snow and Ice Data Center (2018), sea ice forms when water in an ocean freezes. Needle-like crystals composed of nearly fresh water with brine rejected freeze and can float to the surface. The crystals can bond and link, and their aggregation depends on the local conditions. If the surface is calm, thin sheets form and can raft onto each other pushed by the wind. If the surface is rough, slushy pancakes with raised edges form from bumping into each other, particularly from wave action. Gas inclusions and brine can be trapped in the aggregating matrix. Over time, the sea ice contains less brine and more air pockets, with multi-year ice also more likely stiffer and ridged from a history of dynamical interactions. Thermodynamics (like bottom melt from warmer underlying waters) govern the growth and melt of sea ice. Mechanical dynamics (like wind dragging

the ice into drift) govern its motion. Over an annual average, thermodynamics tend towards a uniform thickness through accretion to thin ice and ablation from thick ice, while mechanics tend towards the extremes of open water and thick pressure ridges (Kwok and Sulsky 2010).

Numerous mass-, momentum-, and energy-transferring processes and interactions occur throughout the boundary layer (e.g., Fig. 1.1). In response, an emergent range of scales

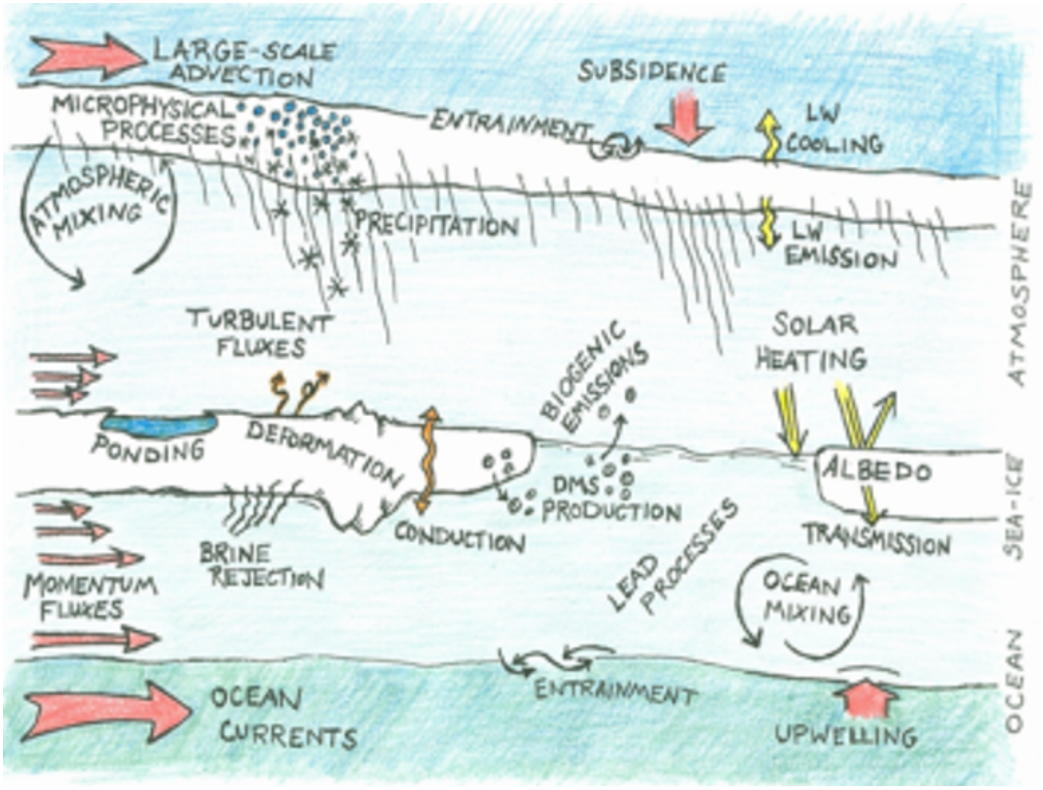

Figure 1.1: *Schematic of processes and interactions in the Arctic Ocean boundary layer (International Arctic Science Committee 2018).*

characterizes sea ice (Mcnutt and Overland 2003), including individual floes over hours to Arctic-scale over months. The main features of the large-scale mean drift pattern are of an anticyclone in association with the Beaufort Sea Gyre and transpolar transport out of the Arctic through the Fram Strait (Colony and Thorndike 1984). Sea ice thickness is generally greatest near the Canadian Arctic Archipelago and northern Greenland, less in

the central Arctic, and further decreasing to the margins (Kwok 2018). To contextualize the atmospheric (sub-)synoptic driven sea ice loss variability at the core of this dissertation, the following introduces seasonal, secular, and year-to-year characteristics of Arctic sea ice change.

1.1.1 Annual cycle

A dominant component of sea ice variability is an annual cycle driven by solar forcing (Fig. 1.2), with growth in the fall and winter and melt in the spring and summer. Differences in the conditions and dominant processes near the surface vary by season (e.g., Fig. 1.3). Below the ice (McPhee 2008), buoyant stability increases during summer with warmer, fresher upper waters and reduced mixing lengths and decreases in winter with colder, saltier near-surface and larger mixing lengths (Peralta-Ferriz and Woodgate 2015). Above the ice, less frequent surface-based inversions during warmer periods (Zhang et al. 2011b) enable stronger coupling to the atmosphere (Steeneveld et al. 2006). Pervasive, thick sea ice cover insulates air–sea fluxes (Maykut 1978) and damps higher-frequency wave energy (Squire 2007).

Physically, different times throughout the year are perhaps best considered as different regimes. Limiting breadth, focus hereafter is on the September minimum and preceding summer period of sea ice loss. Capabilities developed in this thesis can be used for other seasons, especially important as poleward reductions of ice cover develop into seasonally ice-free regions (Jahn et al. 2016; Onarheim et al. 2018). However, application would benefit from evaluation of the modelled representations of sea ice variability and drivers during periods not explored here.

1.1.2 Secular sea ice trends

Increased downwelling radiative flux at the top of the sea ice directly increases the internal energy of the ice (e.g., Eq. 3.1). If the accumulating flux is balanced by latent heat of

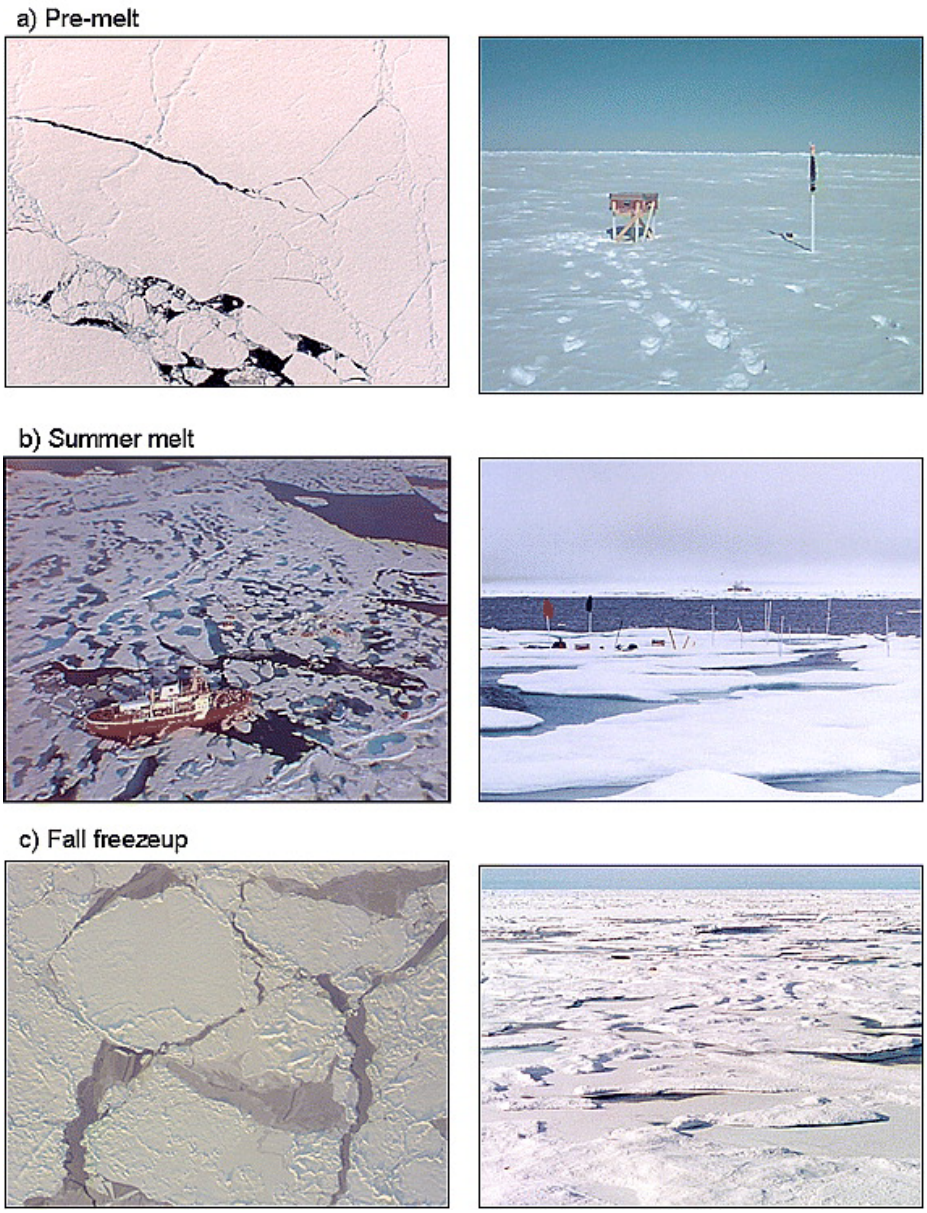

Figure 1.2: *Aerial and surface photographs illustrating changes in sea ice conditions from (a) pre-melt in May, to (b) melt in August, to (c) later freezeup in October near the drifting site of the Surface Heat Budget of the Arctic Ocean field experiment (Perovich (2005), Fig. 1)*

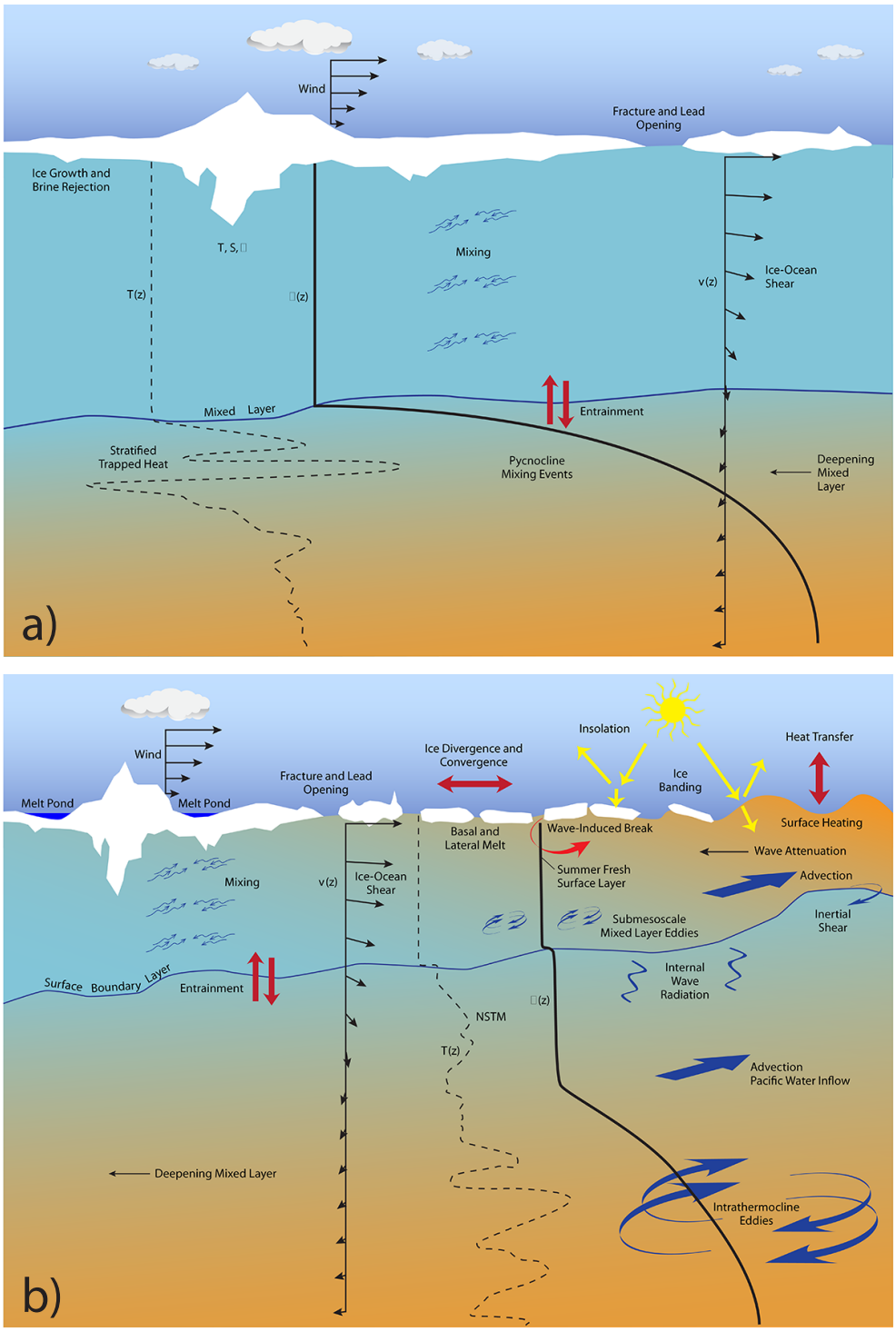

Figure 1.3: *Schematic of (a) winter and (b) summer processes that govern upper ocean stratification and sea ice evolution (Lee et al. 2016). NSTM - near-surface temperature maximum.*

fusion, sea ice melt results (Rothrock et al. 1999). Additional feedbacks further modify the response of the system. For examples, radiatively, meltwater at the surface collects into ponds (Polashenski et al. 2012), dramatically lowering the albedo of the formerly bright ice surface. Thermodynamically, generally warmer Arctic Ocean mixed layer and surface air temperatures reduce the possibility of sea ice recovery, lengthening the melt season (Markus et al. 2009). Mechanically, the internal strength of a younger, thinner ice pack is reduced, with sea ice subsequently more responsive to the atmospheric forcing (Zhang et al. 2012; Kwok et al. 2013). In addition to decreasing September sea ice extent (SIE), projections of seasonal sea ice loss show corresponding increased internal variability under climate change before an ice-free summer Arctic (e.g., Fig. 1.4 derived from the Community Earth System Model (CESM) Large Ensemble (Kay et al. 2015)).

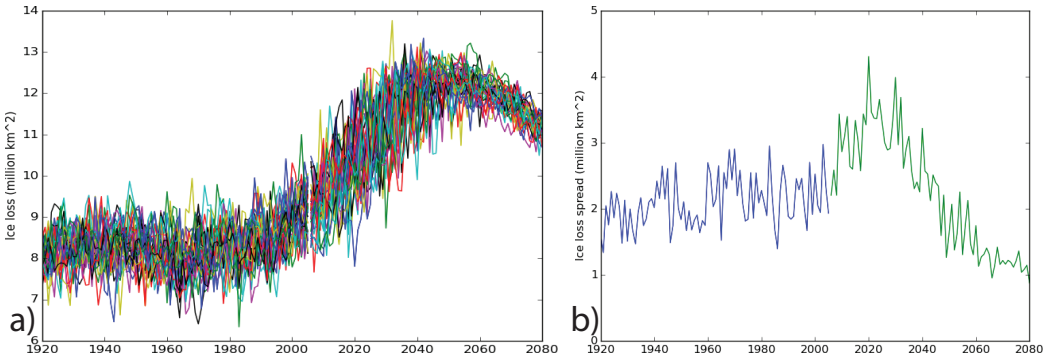

Figure 1.4: *CESM Large Ensemble March minus September (a) SIE colored by ensemble member and (b) ensemble range in SIE representing internal variability colored by historical (blue) and RCP8.5 (green) forcings. Both are by year in M km*^{2}.

1.1.3 Year-to-year variability

Expectations are that dramatic changes in the present and near-future Arctic are possible from anthropogenic change reinforced by growing intrinsic variability (Holland et al. 2008). Accentuated by changes in clouds (Vavrus et al. 2011), rapid, abrupt changes in SIE can be driven by poleward ocean heat transport (Holland et al. 2006). From the more

rapidly-varying atmospheric forcing, anomalous summer mean cyclonic patterns near the pole correlate with anomalous September ice gain, while anomalous summer mean anticyclonic patterns correlate with September ice loss (e.g., Screen et al. (2011); Knudsen et al. (2015); Serreze et al. (2016) and Sect. 3.3.1). A collection of sea ice forecasts suggests that years with larger year-to-year sea ice changes have larger prediction errors (Hamilton and Stroeve 2016).

The consecutive, dual years of 2006 with relatively high September SIE and 2007 with relatively low SIE (5.86 versus 4.27 M km^2 (Fetterer et al. 2017)) exemplify the sensitivity of sea ice to the polar circulation. In 2006, an anomalous summer mean cyclone near the pole extends from the surface through the tropopause (Fig. 1.5a) and is associated with cyclonic sea ice motion (Fig. 1.5c). In contrast, summer 2007 is characterized by a broader anomalous summer mean anticyclone in the western Arctic that extends from the surface through the tropopause (Fig. 1.5.b) associated with consistent anticyclonic and transpolar sea motion (Fig. 1.5.d) also in the presence of a central Siberian low. In 2007, warmer surface air temperatures, sea ice transport from the western to central Arctic, reduced cloudiness and enhanced shortwave, and intermittent bursts of warm, humid Pacific inflow with enhanced longwave and turbulent fluxes were all atmospherically-driven contributions to ice loss (Comiso et al. 2008; Kay et al. 2008; Wang et al. 2009; Maslowski et al. 2012). Correspondingly opposite patterns of colder surface air temperatures and increased relative humidity and cloud fraction (Kay et al. 2008), less transpolar sea ice drift, and decreased influxes of lower-latitude air masses (Graversen et al. 2011) are consistent with the summer mean circulation and larger SIE in 2006. A central aim of this thesis is to determine the degree to which integrated sea ice changes can be driven by a particular feature within the polar circulation.

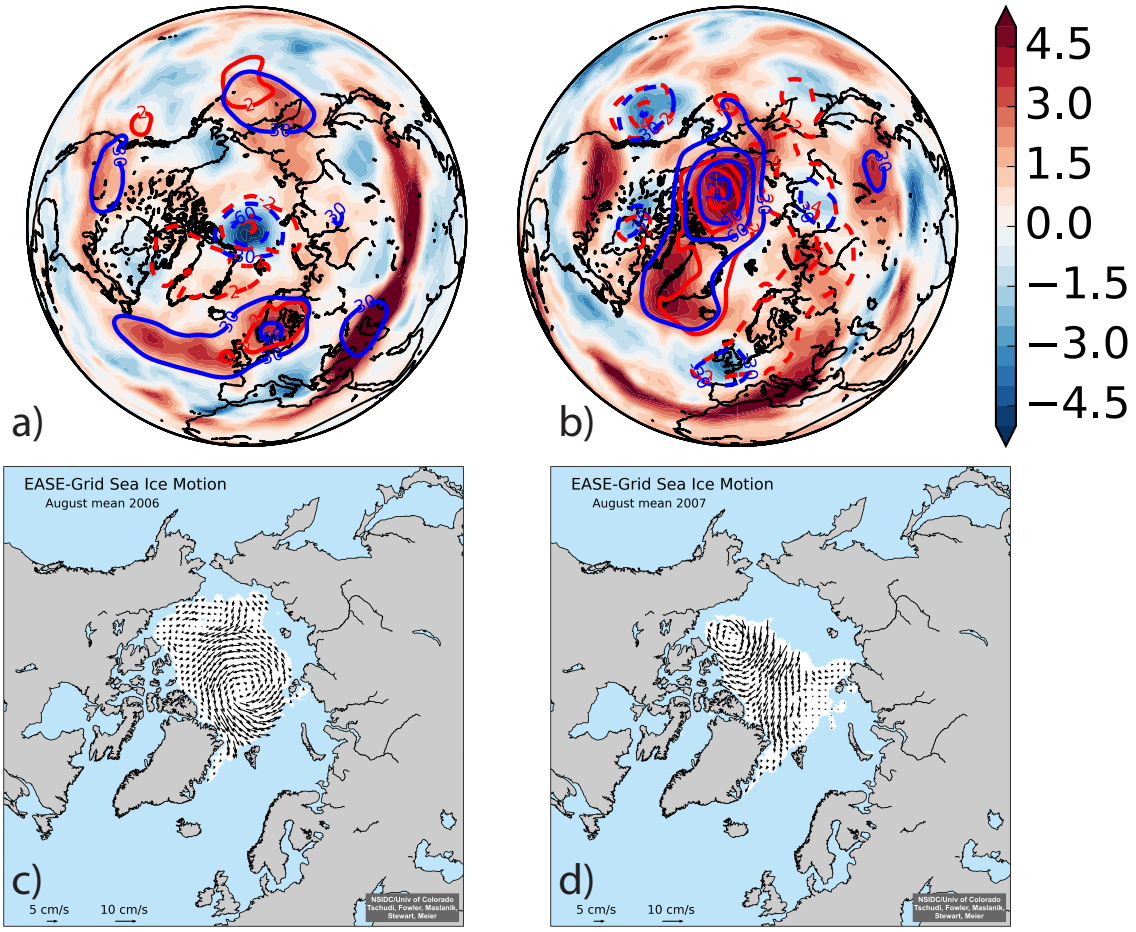

Figure 1.5: *Comparison of June, July, and August (a) 2006 and (b) 2007 anomalies in tropopause potential temperature (color, 0.5 K interval), sea level pressure (red contour, 2 hPa interval), and Z500 (blue contour, 30 m interval) from the 1979 to 2014 June, July, and August mean. (c,d) Mean sea ice motion for August 2006 and 2007, respectively (Tschudi et al. 2016). Dashed contours are negative. Data in (a,b) are from ERA-Interim (Dee et al. 2011).*

1.2 Linkages in a multi-scale, coupled system

Components in the Arctic region are part of larger systems, with characteristic scales in the Earth system varying over orders of magnitude (e.g., Fig. 1.6). Couplings exist across

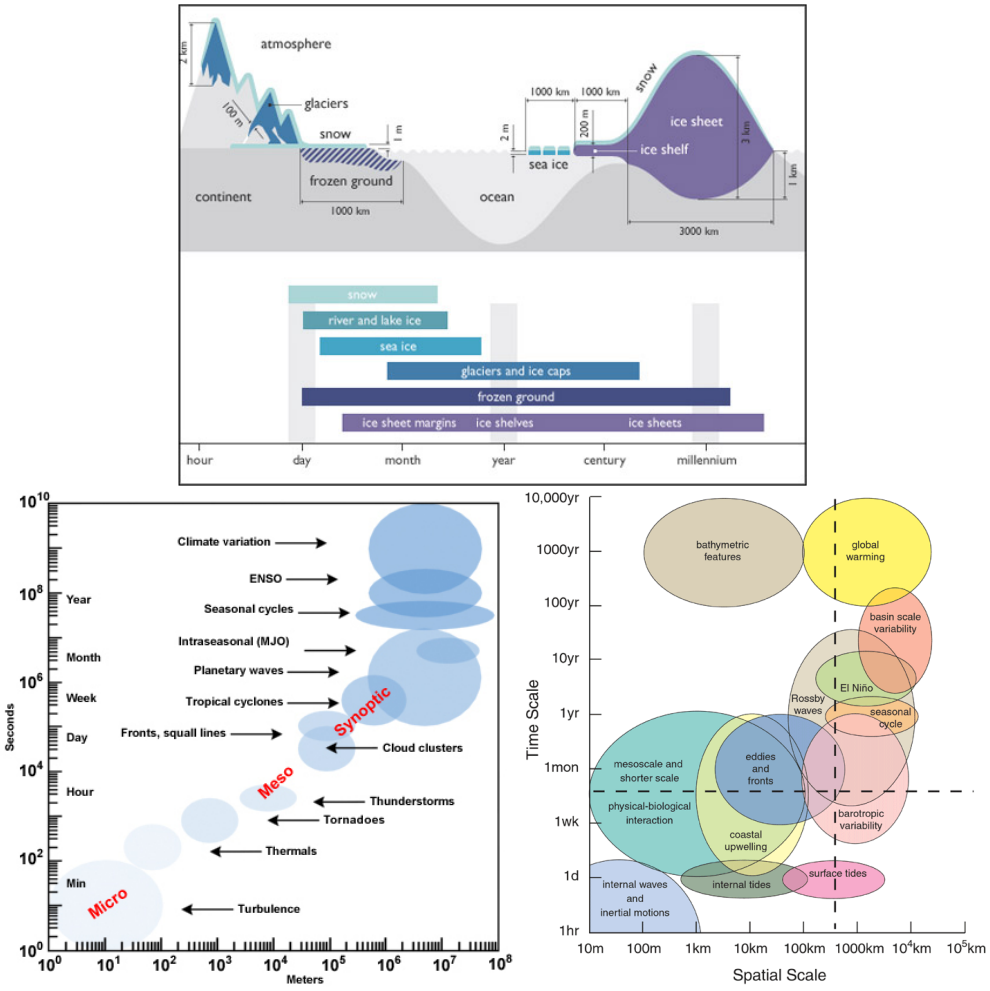

Figure 1.6: *Schematics of characteristic scales for cryosphere (IPCC 2007), atmosphere (Laing and Evans 2011), and ocean domains (Chelton 2001)*

time and length scales, latitudes, vertical levels, and components, as exemplified by sea ice change (Sect. 1.1). Disentangling the roles of components and couplings is fundamental to a causal understanding of the system.

Given the importance of sea ice variability and the sea ice edge in particular, there is a substantial literature on the roles of different factors of atmospheric forcing and implications for predictability (Serreze and Stroeve 2015; Guemas et al. 2016). Studies span a range of scales and phenomena for sea ice locally and Arctic-wide in statistical, idealized, and comprehensive dynamical models, including individual events (Brümmer and Hoeber 1999; Heinemann 2003; Zhang et al. 2013), longer-range with teleconnections (Fang and Wallace 1994), seasonally (Olason and Notz 2014), decadally (Mysak and Venegas 1998), and longer (Petty et al. 2016; Ding et al. 2017). Case studies are used consistently to explore linkages. For example, a historic surface cyclone in August 2012 (Simmonds and Rudeva 2012) contributed to the following September record SIE minimum but did not cause it alone based on a forced ice-ocean model (Zhang et al. 2013). Coherent atmospheric features termed tropopause polar vortices (TPVs; Ch. 2) have been noted to be associated with changes in Arctic sea ice (Simmonds and Rudeva 2012; Yamazaki et al. 2015; Ono et al. 2016) as precursors to surface cyclones.

However, neither the linkages nor the scales for the impacts of TPVs on sea ice have been tested. As transient, (sub-)synoptic features in chaotic flow far from the surface, TPVs may be evanescent with negligible integrated impacts. As coherent, potentially long-lived dynamical features, TPVs could be prominent eddy components of driving year-to-year variability (Sect. 2.5). The central question of this work is: to what degree and through what mechanisms can TPVs impact variability of Arctic sea ice? Novel focus on contributions from TPVs in their own right and methods developed towards evaluating this feature-based question causally within an integrated, complex system further direct this work. If TPVs have meaningful impacts on sea ice, realizing the increased potential predictability associated with the reduced chaoticity in coherent vortices (Provenzale 1999) and extended timescales of the stratosphere (Tripathi et al. 2015; Kidston et al. 2015) could extend limits on sea ice predictability imposed by atmospheric variability and predictability

(Serreze and Stroeve 2015). If not, conceptual and predictive sea ice models can develop towards other considerations.

Ch. 2 further defines TPVs and explores their model representations and diagnosed characteristics. To integrate the possible linkages between TPVs and sea ice, dynamical model sensitivity experiments are pursued. A comprehensive coupled, global, and variable-resolution atmosphere model of the Earth system satisfying proposed necessary requirements for representing impacts of TPVs on sea ice is the focus of Ch. 3. The model is employed to quantify impacts of TPVs on Arctic sea ice and the associated mechanisms (Ch. 4). Ch. 5 concludes and discusses directions for future work.

Chapter 2

TPV thinking

Among the disturbances on the extratropical tropopause (Gettelman et al. 2011), a functional, qualitative definition of TPVs is as coherent features based on the dynamic tropopause associated with the larger polar vortex that have a regional minimum in potential temperature and cyclonic circulation or regional maximum in potential temperature and anticyclonic circulation that last over time (Szapiro and Cavallo 2018). In manifestation, TPVs are common, coherent upper-level potential vorticity (PV) anomalies with typical radii of 100 to 1000 km and lifetimes of days to months (Hakim 2000; Hakim and Canavan 2005; Cavallo and Hakim 2010). TPV-like features play documented roles in so-called PV thinking (e.g., Hoskins et al. 1985; Holton and Hakim 2013), surface cyclogenesis and high-impact weather (e.g., Davis and Emanuel 1991; Morgan and Nielsen-Gammon 1998; Grams et al. 2011; Simmonds and Rudeva 2012), geographic climate (e.g., Shapiro et al. 1987; Nieto et al. 2008; Kew et al. 2010), stratosphere-troposphere exchange (e.g., Sprenger et al. 2007), potential predictability (e.g., Provenzale 1999), and evaluation of model skill (e.g., Béguin et al. 2012).

Knowledge of where a TPV is, how it is shaped and changing, and what is nearby can aid further systematic and reproducible approaches in these and more areas. For example, TPV tracks can relate how information from distant radiosonde observations can impact the simulated development of a surface cyclone days later (Yamazaki et al. 2015). Accurate, automated tracking of TPVs in gridded data contributes to improving our knowledge of TPV structure and history (Sect. 2.1). Model experiments and dynamical budgets further our understanding of their driving mechanisms (Sect. 2.2).

While useful, models have errors (Box 1979). To explore the uncertainties and sensitivities associated with choices in model design, the modelled representation of TPVs is the

focus of Sect. 2.3. Introducing known changes/errors into a model is a step in classical one-factor-at-a-time sensitivity analysis (e.g., Murphy et al. (2004); Razavi and Gupta (2015)). With effective strategies for modifying TPVs during simulations (Sect. 2.4), TPV-based sensitivity experiments within coupled systems are possible.

2.1 Identification/definition of the dynamic tropopause and TPVs

2.1.1 Diagnosis of the dynamic tropopause

One approach to define the extratropical tropopause (Gettelman et al. 2011; Ivanova 2013) is through PV (definition and derivation of Ertel's potential vorticity (EPV) is included in Appendix A). Reduced stability and increased density in the troposphere typically yield relatively lower PV than in the stratosphere above. Conventionally, the dynamic tropopause is found by searching downwards for a PV threshold within each column independently, possibly with thickness criteria (e.g., Zängl and Hoinka (2001)). However, vertical mixing, folding, and convective-scale vorticity can generate ambiguity with multiple candidates for the tropopause within a column, occurring globally (Añel et al. 2008) with smaller scales less smoothed for increasing model resolution (e.g., Skamarock (2011)). Fig. 2.1 simplifies such a problematic case.

Beyond thickness conditions, the tropopause as a surface can be identified more robustly by including consistency with information outside the column. To identify the tropopause as a layer between the respectively connected high PV stratosphere and low PV troposphere, flood-fill segmentations of the stratosphere and troposphere can be utilized. For example, starting with initial seed cells near the surface with low PV, all connected values below a chosen PV threshold can be found by iterating through valid nearest neighbors. This identification of the connected troposphere yields the tropopause as the top of the tropospheric volume. Note that the top of the troposphere is above the bottom of the stratosphere, and the bottom of the stratosphere may reach the surface, especially within

PV towers (e.g., Pang and Fu (2017), Fig. 6c). If model data is archived with sparse vertical levels, post-output diagnosis may have larger uncertainties. Also note that the chosen isertelic level can impact TPV metrics quantitatively (e.g., Fig. 4 in Cavallo and Hakim (2009)).

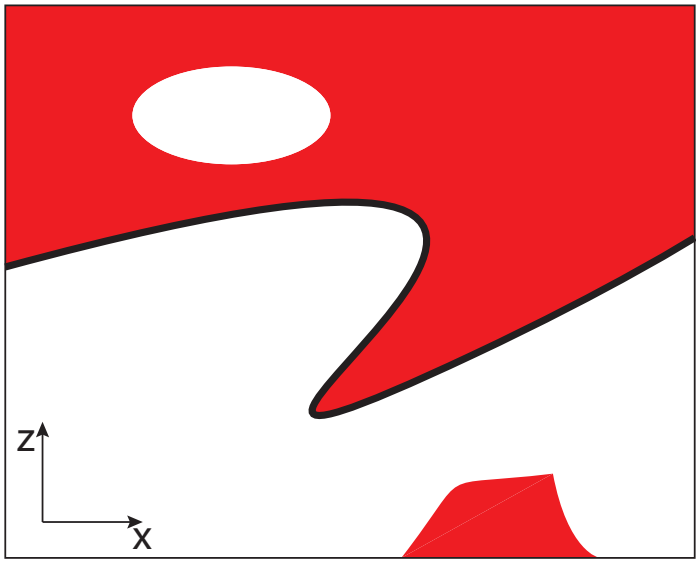

Figure 2.1: *Schematic vertical cross-section of an atmospheric state with high (red) and low (white) potential vorticity. Complicating diagnosis of the tropopause (thick black contour) in this example are a tropopause fold, a low potential vorticity feature above (e.g., stratospheric wave break), and a high potential vorticity feature near the surface (e.g., surface cyclone or low-level inversion layer).*

2.1.2 TPV tracking

Further definition of "coherent", "regional", "associated", and "last" in the functional, qualitative definition of TPVs is fundamental to a rule-based scheme. Szapiro and Cavallo (2018) includes a review of known TPV tracking methods and discussion and evaluation of a novel restricted regional watershed segmentation and major correspondence overlap tracking method. A summary of the approach and implications for TPV shape and lifetime

are highlighted below to support following arguments. The openly-available publication, user's guide, and software provide more complete information.

TPVTrack is designed to improve representation of TPV (1) spatial structure, with variable shapes and intensities, and (2) time evolution, with mergers and splits. Spatially, locally-based methods like Hakim and Canavan (2005); Simmonds and Rudeva (2014) suffer from sensitivities of gradients to local perturbations and require smoothing, while Kew et al. (2010) prescribes size. Temporally, Hakim and Canavan (2005); Kew et al. (2010) create tracks for features that are sufficiently near or overlapping in the horizontal. If one vortex splits into multiple, all share the previous history, yielding inconsistencies between tracks and counts. Simmonds and Rudeva (2014) weights expected evolution of TPV metrics to estimate a probability of association, requiring an expected evolution of TPV metrics. Problematically, radius changes occur when TPVs split or merge. Intensity and amplitude can jump from data assimilation increments or strong interactions with surface lows and terrain. For TPVs defined via TPVTrack, the main rules are

- Core is a regional extremum: TPV core of an (anti)cyclone is a minimum (maximum) in tropopause potential temperature within a neighboring disk of prescribed size.

- Feature is spatially coherent: Preliminary watershed basins are composed of cells that drain by steepest descent to the core (or local extremum within the core's regional neighborhood). With watersheds for the surface and its opposite, cells with positive (negative) local relative vorticity are associated to the (anti)cyclonic core. Shape is further restricted to an enclosing isentrope within the associated watershed basins, varying by feature as a user-defined percentile of amplitudes.

- Feature is temporally similar: Using similarity as a function of "horizontal" overlap under advection and "vertical" overlap in intensity, tracks are constructed from 1-1 correspondences between basins at consecutive times, where each is the most similar to the other out of all possible matches.

Operating natively on gridded structured or unstructured input data, the initial watershed basins segment the undulations of the tropopause without prescribed size or intensity (through steepest descent) and with more robustness to smaller scales (through modified descent to regional extrema cores). The 1-1 correspondences reduce false positive tracking of nearby features. A track begins when a basin has no major correspondence to a basin at the previous time and ends when a basin has no major correspondence to a basin at the next time. For example, a TPV breaking off from a parent would be tracked from the timestep after the break through the chain of major correspondences.

There are four user-specified parameters: size of the filtering disk for regional extrema, percentile for watershed basin restriction, minimum lifetime, and polar classification. For the first two parameters, default settings are a 300 km filtering disk for regional extrema and 5^{th} percentile of the amplitudes of the basin's boundary cells with respect to the core for restriction. The scale of the filtering disk should be larger than the grid scale but smaller than a TPV. The percentile should be between $(0, 100)$ for more robust and consistent spatial shape than using the last closed contour or the full watershed basin. TPVTrack output does not depend on the latter two parameters; rather, the user imposes them in post-processing TPVs from tracks. Minimum lifetime should be chosen larger than the time interval of the input data but less than the lifetime of a TPV. TPVs are classified to be directly associated with the polar vortex if polewards of the (flow-dependent) polar jet (e.g., at genesis or during their lives). Fundamentally, these are imposed filters, with sensitivities that can propagate through the algorithm. Comparison among several settings, different tracking approaches, and manual interpretation increases confidence in the robustness of results.

With tracks of multiple features, a central problem is to diagnose and justify when they interact. Sensitivity analyses (e.g., diagnosed from ensembles (Torn and Hakim 2008) routinely produced operationally) may provide dynamical and statistical evidence of ties under the span of sampled historical or projected conditions.

2.2 Dynamics

In terms of EPV, TPV dynamics can be diagnosed from states and tendencies of winds, mass, and temperature within the object (Cavallo and Hakim (2009); Appendix A). In a composite sense over modelled TPV lifetimes, a coherent vortex advects about with modifying diabatic rates of O(1 K d^{-1}; 0.1 PVU d^{-1}) (Cavallo and Hakim 2010). Frictional PV tendencies are smaller near the vortex core (Cavallo and Hakim 2009). Diabatic tendencies are mainly a difference between near-tropopause longwave cooling creating EPV and mid-level cloud production destroying EPV (Cavallo and Hakim 2009, 2010, 2013). A similar formulation is applied to an individual case of a long-lived summer TPV below.

2.2.1 Methods

To explore the roles of the terms in the PV budget (for TPVs) in a global atmospheric model, the atmospheric component of the Model for Prediction Across Scales (MPAS-A; Skamarock et al. (2012)) v4.0 is used with a zonally-variable mesh density and corresponding Arctic-refined mesh with approximate spacing near 25 km north of 60 °N smoothly transitioning to 90 km south of 30 °N. 41 vertical levels to a model top at 30 km with time step of 120 s are used on the global domain. Vertical velocity is damped (Klemp et al. 2008) above 22 km to reduce reflections from the model top. Physics parameterizations include WSM6 microphysics (Hong and Lim 2006) with 8 time steps per dynamics time step, Rapid Radiative Transfer Model for General circulation models shortwave and longwave radiation (RRTMG; Iacono et al. (2008)) with a multilayer upper-boundary condition (Cavallo et al. 2011) and time step of 20 minutes, Yonsei University planetary boundary layer (Hong et al. 2006), Tiedtke deep and shallow convection (Tiedtke 1989), and Unified Noah land surface model (Tewari et al. 2004). Initial conditions are interpolated from ERA-Interim analyses (Dee et al. 2011), with sea surface temperatures and sea ice concentration updated every 6 h from interpolated ERA-Interim.

The tropopause is diagnosed natively during the model integration by interpolating potential temperature to a conventional potential vorticity isosurface (2 PVU; 1 PVU= 1.0×10^{-6} m^2 K s^{-1} kg^{-1}). Calculation of EPV $q = \frac{\omega_a}{\rho} \cdot \nabla\theta$ for absolute vorticity ω_a, dry air density ρ, and potential temperature θ is performed at cell centers, with the product in the vertical generally dominating. Vertical derivatives are computed using centered differencing in the column, except for one-sided differencing at the top and bottom levels. Horizontal derivatives are approximated by applying the Green-Gauss theorem to each axis, with values across a face averaged for the flux. Since the integration is conducted in parallel using tiled sub-domains over separate processors, at least one neighbor of information is exchanged across the domain-decomposed boundaries for the horizontal stencil. Vertical vorticity is area-weighted from the Voronoi corners. Horizontal velocities reconstructed to the cell centers are differenced to derive horizontal vorticity.

To more robustly identify the dynamic tropopause, particularly in cases of multiple candidates within a column as recommended in Szapiro and Cavallo (2018), the tropopause is found at the bottom of the connected stratosphere. The connected stratosphere is identified through an iterative flood-fill of high-PV cells connected to initial seeds near the model top (similar to the so-called forest fire algorithm, e.g., Torbert (2016)). The tropopause layer is defined as the bottom of the identified stratosphere, which is at the surface if the entire column is above 2 PVU and at the model top if the entire column is below 2 PVU. For values on the tropopause (e.g., potential temperature on the 2 PVU surface, which is a primary metric for TPVs in this study), vertical interpolation (of potential temperature) to the PV isovalue is linear in q from the trapping vertical levels. The software for calculation of PV and the tropopause is publicly available since the standalone MPAS v5.0 release.

EPV budgets are calculated in three components during the integration: transport, diabatic, and frictional tendencies of EPV. For transport, diagnosed EPV is first split into two non-negative scalars: $q = q(q \geq 0) + q(q < 0) = q_+ - q_-$. The non-negative q_+ and q_- are transported separately by the dynamical core as additional mass species and re-combined

to define the transported EPV. Diabatic tendencies are calculated from potential temperature tendencies generated by the individual physics parameterizations and explicit mixing at each timestep. Similarly, frictional tendencies are calculated from wind tendencies generated by the individual physics parameterizations and explicit mixing at each timestep. A version of the source code with the additional tracer transport is publicly available from `https://github.com/nickszap/MPAS-Release.git` in the "pvConservation" branch.

Closure of the budget can be evaluated by comparing the local time rate of change of EPV (differenced by diagnosing EPV over consecutive times) to the transport, diabatic, and frictional components. Local rate of change and transport tendencies tend to be large and cancelling, with smaller diabatic and frictional components (not shown). Residuals can be on the order of O(0.1 PVU d^{-1}) or larger (10^{-12} in model units). Given these uncertainties in EPV budget closure, for the following, only diabatic and frictional contributions to the EPV budgets calculated explicitly are considered as two separate terms.

2.2.2 Formation, maintenance, and decay of a long-lived summer TPV

Towards further describing the dominant mechanisms in TPVs' lifecycles and devising strategies for physically-motivated TPV-based perturbations (e.g., Sect. 2.4), the diagnosed EPV budget is used to analyze the dynamics of one of the longest-lived TPVs in the satellite era, manually tracked from 02 July 2006 to 30 September 2006. This TPV is associated with episodic surface forcings and time-mean polar circulations, with connections to summer sea ice loss (Sect. 2.5.1).

To explore genesis, MPAS-A is initialized over a day earlier on 00 UTC 01 July 2006 from ERA-Interim. The simulated formation as a separate vortex occurs through deformation of the parent vortex, filamentation, and eventual splitting into a separate feature near 50 °E (Fig. 2.2). Frictional tendencies dominate diabatic tendencies near the splitting, with diffusion driving the frictional tendencies. Note that advection can also contribute to the evolutions of the vortices and filaments (e.g., Ottino and Ottino (1989)).

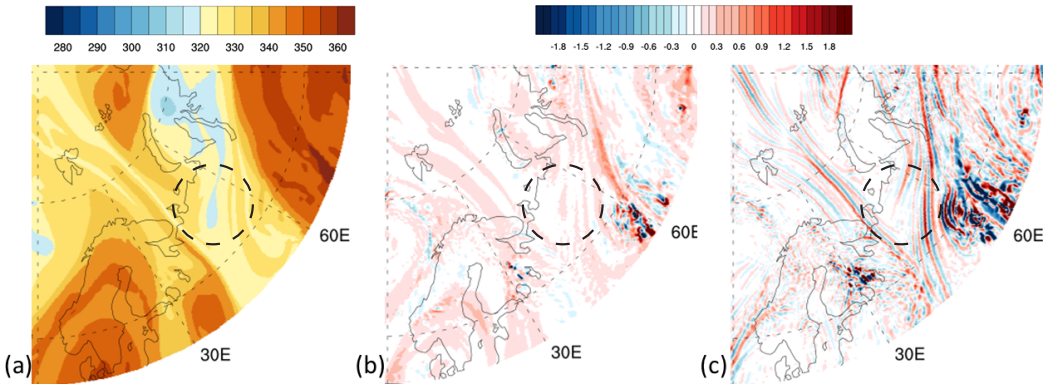

Figure 2.2: *MPAS-A simulated 18 UTC 02 July 2006 (a) tropopause potential temperature (K; 5 K interval). (b) Diabatic and (c) frictional potential vorticity tendencies on the tropopause (0.1 PVU d^{-1} interval). TPV of interest is encircled (dashed black).*

To explore maintenance and intensification, the model is initialized on 00 UTC 15 August 2006 during an extended period of intensification of over one month (Sect. 2.5.1). Diabatic tendencies dominate frictional tendencies near the core (Fig. 2.3), with longwave radiation the largest of the diabatic tendencies (Fig. 2.4).

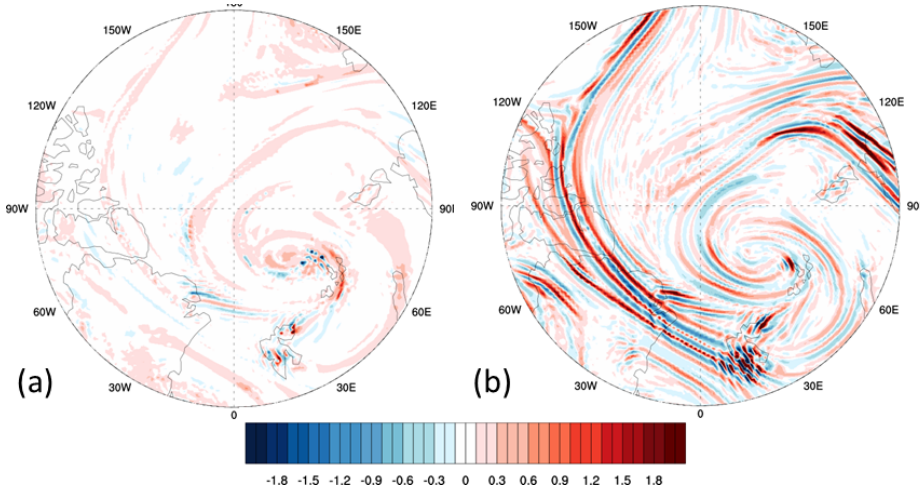

Figure 2.3: *MPAS-A simulated 18 UTC 18 August 2006 (a) diabatic and (b) frictional potential vorticity tendencies on the tropopause (0.1 PVU d^{-1} interval)*

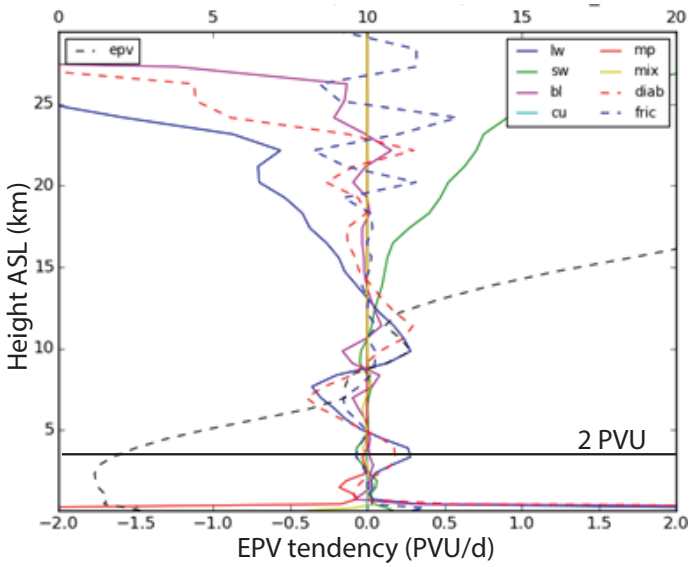

Figure 2.4: *MPAS-A simulated 18 UTC 18 August 2006 vertical profiles of potential vorticity tendencies (PVU d^{-1}, bottom axis) averaged on model levels within 5 K of the TPV core. Colors are blue: longwave radiation, green: shortwave radiation, red: planetary boundary layer, cyan: convection, red: microphysics, yellow: explicit diffusion, dashed red: net diabatic, and dashed blue: net frictional. Potential vorticity (dashed black, (PVU, top axis)) shows the tropopause below 5 km (denoted in black).*

To explore decay, the model is initialized over a day before on 00 UTC 28 September 2006. Frictional tendencies dominate diabatic tendencies near the TPV, with orographically-driven gravity wave drag and diffusion both contributing to the frictional tendencies (Fig. 2.5) over the Verkhoyansk Range in Eastern Siberia for the apparently geographically-trapped vanishing TPV.

Considered separately, the diabatic and frictional components appear to have distinct, coherent regions at scales of the contributing processes. Frictional tendencies are large near wind gradients, like in deformation regions between strong cyclones and anti-cyclones, and oscillations from orographic wave effects. Diabatic tendencies can be coherent about the core, associated with a TPV's anomalous structure. However, there is a non-negligible

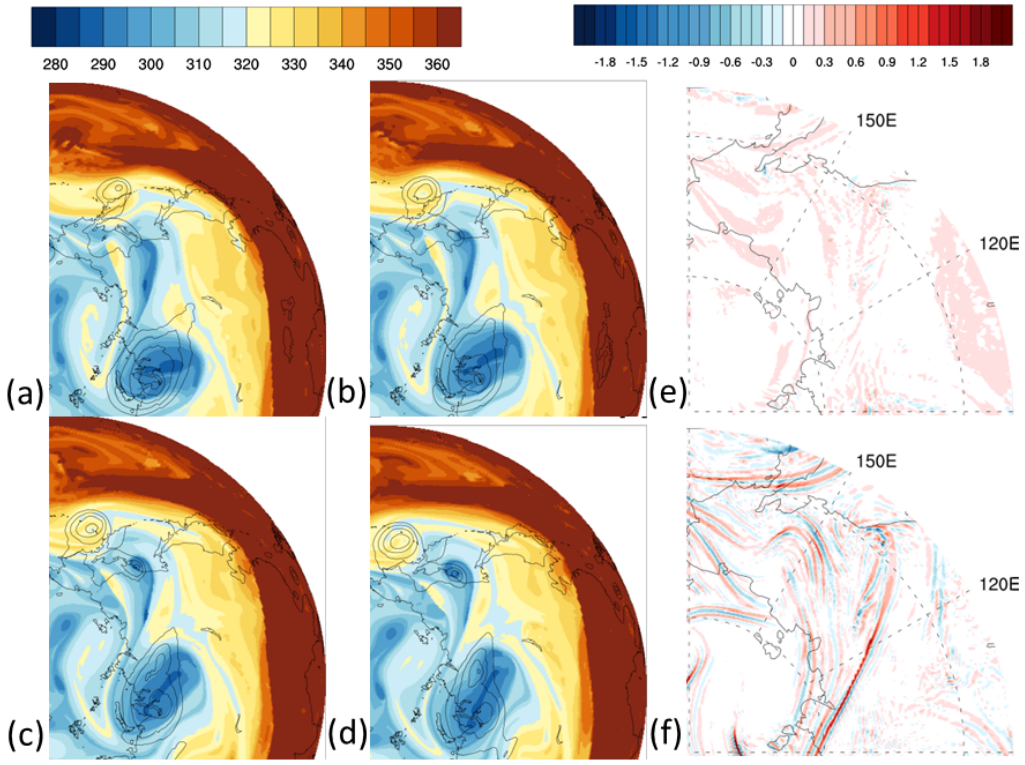

Figure 2.5: *MPAS-A simulated 6-hourly 06 UTC 29 to 00 UTC 30 September 2006 (a,b,c,d) tropopause potential temperature (K; 5 K interval). 06 UTC 29 September 2006 (e) diabatic and (f) frictional potential vorticity tendencies on the tropopause (0.1 PVU* d^{-1} *interval).*

residual between local changes and advective, diabatic, and frictional terms calculated separately. Other models similarly exhibit non-conservation (Saffin et al. 2016). Even with a finite volume form for fluxes used in integration, deviations from conservation are expected for non-state model variables. To potentially reduce the magnitude of the residual, the implemented finite differencing or moist variant of the formulation (e.g., Guoxiong et al. (1995)) could be more consistent with the dynamical core. A variation based on the model's state variables would perhaps be more direct.

A TPV in 2006 lives as an individual coherent feature for months, which is remarkable for a transient, (sub)synoptic feature. During genesis, maintenance, and lysis, it exhibits physically coherent characteristics and dynamics. Beyond identifying TPVs, attention now

switches to how simulated TPVs impact the future and can inform the models used to do so.

2.3 Sensitivities in a hierarchy of model complexity

Model design, resolution, and associated filters impact simulated processes (Williamson 2002; Catto et al. 2010), variability (Nutter et al. 2004; Skamarock 2011), climate and extremes (Jung et al. 2006; Tilinina et al. 2014; Hagos et al. 2015; Jun et al. 2018), cost and use (Wedi et al. 2015; Michalakes et al. 2015), and our understanding (Held 2005). With physical process rates driving dynamically consistent TPV evolution (Sect. 2.2), numerical experiments may also introduce systematic uncertainties tied to the model design. Previous limited-area simulations exhibit coherent vortex-relative model biases (Cavallo and Hakim (2010), Fig. 4). The following analyses sample sensitivities of modelled TPVs to choices in resolutions and parameterizations in model configurations ranging from single columns to the global atmosphere. The goals are to better understand the characteristics of modelled TPVs and inform the design of suitable model configurations for TPV-based sensitivity experiments.

2.3.1 TPV intensity in an operational model

Operational numerical weather predictions (and simulation archives) provide an ensemble of opportunity to further explore characteristics and sensitivities of modelled TPVs. The Observing System Research and Predictability Experiment (THORPEX) Interactive Grand Global Ensemble (TIGGE) project (Bougeault et al. 2010) offers a collection of daily global 1- to 2-weeks ensemble forecasts from operational weather forecasting centers. Here, the European Centre for Medium-Range Weather Forecasts (ECMWF) operational forecasts are assumed to represent state-of-the-art TPV forecasts, with modelling system most comparable to that of the default tracks dataset derived from ERA-Interim (Szapiro and Cavallo 2018) used as the reference analysis.

Since forecasts are available starting in October 2006, we first consider a period of intensification for the longest-lived TPV that occurred in 2007 instead of 2006. Considering the forecast initialized on 00 UTC 20 July 2007 (Fig. 2.7.a), ECMWF ensemble TPV intensification error is over 3 K d^{-1} for all members over the first 3 days. The higher-resolution forecast is also weak relative to ERA-Interim analysis but more intense than the ensemble forecasts. The United Kingdom Met Office ensemble is similar (not shown). While the archived vertical levels are sparse, initial conditions for the forecasts have an O(100 hPa) deep boundary layer, westerly winds, and dewpoint depressions that nearly vanish throughout the troposphere, in contrast to ERA-Interim with a deeper boundary layer, west-northwesterly winds, and larger free-troposphere dewpoint depressions (Fig. 2.6). Differences in winds do not affect the intensity of a materially-advecting core di-

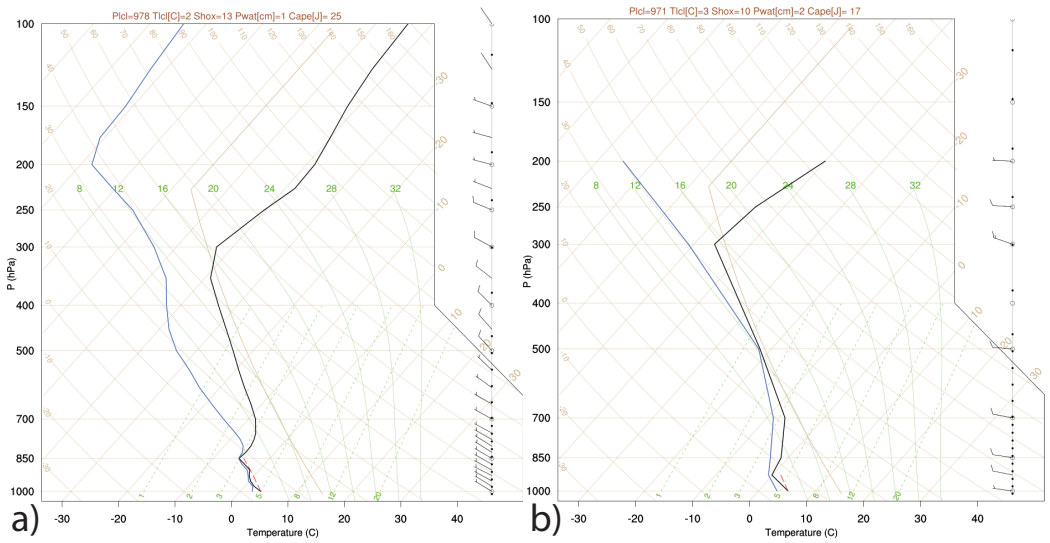

Figure 2.6: *Skew T - log p diagrams through TPV core on 00 UTC 20 July 2007 from (a) ERA-Interim analysis and (b) operational ECMWF high-resolution forecast initial conditions.*

rectly. Vertical moisture profiles are central to the diabatic intensification of TPVs through competing effects of weakening from latent heating and strengthening from longwave radiation (Cavallo and Hakim 2010, 2013). Below-tropopause latent heating reduces upper tropospheric stability, diabatically destroying PV near the tropopause (e.g., Sect. 2.2).

However, differences in data assimilation (additional observations and improved bias correction for radiosondes and radiances (Dee et al. 2011)) and model versions (Cycle 31r2 to 32r2) complicate further diagnostic attribution.

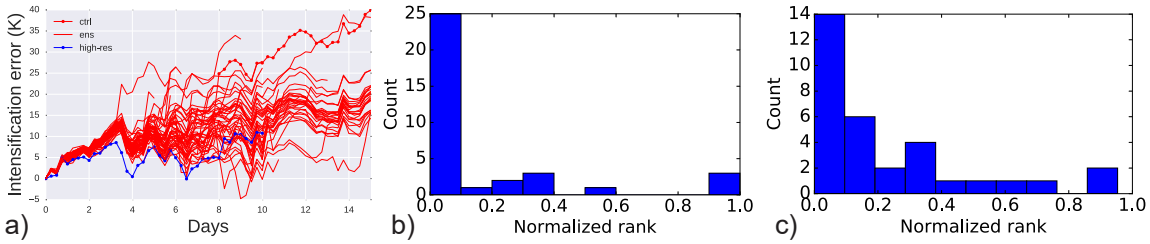

Figure 2.7: *(a) Forecast minus analysis TPV intensification (K; change in tropopause potential temperature of the core from the initial time) for the ECMWF ensemble initialized on 00 UTC 20 June 2007 for the high-resolution (blue) and ensemble (red; control with circles) members. A perfect forecast is zero for all days, and positive indicates weaker intensification than the analysis. Rank histograms of 1-d TPV intensification for forecast dates with intensifying analysis TPVs for (b) analysis in the ensemble and (c) high-resolution member in the ensemble. Rank is normalized by ensemble size so 0 is smaller and 1 is larger than all members with forecast TPVs.*

To explore whether the forecast for the long-lived TPV in 2007 is symptomatic of a systematic model error of weak intensification, forecasts for historical TPVs are considered during October 2006 through 2015 in the operational ECMWF higher-resolution deterministic and coarser ensemble. Since obtaining all forecasts was not feasible due to retrieval time and storage and requests to the TIGGE server suffered from non-negligible failure rates addressed through case-by-case manual intervention, analysis is limited to long-lived analysis TPVs. These are of primary interest due to their long physical maintenance and associated potential for extended predictability. Imposing a minimum lifetime requirement of 28 d to balance sample size and retrieval constraints, of the 28961 analysis tracks lasting at least 2 d during this period, 66 tracks last at least 28 d, with the genesis or lifetime-mean core latitude of all but one of the long-lived tracks polewards of 60 °N. Since the

one equatorward track reaches a maximum latitude of 74 °N, all tracks are associated with the (mean) tropospheric polar vortex during their lifetimes. Forecasts for these 66 longest-lived cyclonic TPVs are obtained with initialization at 00 UTC 4 to 5 d after genesis of each analysis TPV, requiring that there be a coherent TPV in each forecast's initial conditions. Further selecting the cases with intensifying TPVs (those with a negative change in core tropopause potential temperature in analysis over the first forecast day), forecast TPVs are found by searching for the longest track within 300 km of the initial analysis TPV (matching the minimum distance required between regional tropopause potential temperature extrema used to generate tracks). Since a matching forecast TPV track may not exist (e.g., the forecast TPV track terminates within 2 d), only the ensemble members with a matching track for each date are considered. In effect, this creates an ensemble size varying by case and improves the ensemble forecasts by disregarding non-matching members.

Rank histograms (Hamill 2001) across dates for the 1-d intensification of analysis in the ensemble (Fig. 2.7.b) and the higher resolution forecast in the ensemble (Fig. 2.7.c) show that both the analysis and high-resolution forecast frequently fall in the left tail of the ensemble distribution. That is, intensification in the ensemble is consistently weaker than both the analysis and the higher-resolution forecast, consistent with the single, independent case from 2007 described above.

In this exploratory analysis based on ECMWF forecasts and analysis TPVs derived from ERA-Interim, ensemble forecasts exhibit a systematic model error of weak TPV intensification, where errors in individual forecasts can exceed 3 K d^{-1}. Inclusion of more forecasts (e.g., from other operational centers) and alternate reference truths (e.g., from operational analyses, other reanalyses, or in-situ observations) may qualify the robustness of these conclusions. If robust, understanding and addressing the error sources may contribute to continuing the steady improvement of weather predictions (Bauer et al. 2015).

2.3.2 Single column TPVs

Sensitivities in diagnosed TPVs in operational models could originate from differences in both initial conditions and model configurations (Sect. 2.3.1). Towards exploring the sensitivities of changes in model configurations (Sect. 2.3.2.1) and initial conditions (Sect. 2.3.2.2), the following uses a simplified 3x3 single column model (SCM) configuration (Hacker et al. 2009) of the Advanced Research Weather (ARW) version of the Weather Research and Forecasting (WRF) model (Skamarock et al. 2008), version 3.7.1.

2.3.2.1 Perturbed model configurations: Vertical profiles and dynamic tropopause

To explore whether varying the formulations of process rates within model vertical columns generates substantial differences, atmospheric initial conditions from ERA-Interim are vertical columns through the cores of the 100 longest-lived tropopause polar cyclones 1979 to 2015 (using the default ERA-Interim tracks dataset of Szapiro and Cavallo (2018)) 5-d after genesis. The surface is treated as ocean at 274 K for simplicity and uniformity, and the date and location correspondingly vary by case. For each TPV, a control and 7 perturbation simulations are run for 5 d (Table 2.1), constructing an ensemble sampling the sensitivity to single column model configuration. These experiments are designed to test whether there

Simulation	Boundary layer	Convection	Microphysics	Radiation	Δt	Δt_{rad}	Levels
Control	YSU	Kain-Fritsch	WSM6	RRTMG	2 min	2 min	61
Perturbations	MYNN 2.5	Grell-Freitas	Morrison 2-M	CAM	30 min	20 min	121

Table 2.1: *Single column model configurations for the control and individually perturbed settings. References for the parameterizations are in the text.*

are sensitivities to TPV intensity from boundary layer, convective, microphysical, and radiative processes, vertical resolution, and frequency of physics and radiation couplings in

a convectively-parameterized column of a model configuration suitable for (sub)seasonal forecasts (e.g., Sect. 3.3.3).

For the control, physics parameterizations include Yonsei University planetary boundary layer (YSU PBL) (Hong et al. 2006), Kain-Fritsch convection (Kain and Fritsch 1993), WRF single moment microphysics (WSM6; Hong and Lim (2006)), Rapid Radiative Transfer Model longwave radiation (RRTM-LW; Mlawer et al. (1997)), RRTM for General circulation models shortwave radiation (RRTMG-SW; Iacono et al. (2008)), and Unified Noah land surface model (Tewari et al. 2004) using a constant physics and dynamics timestep of 120 s on a 20-km spacing grid in the horizontal with 61 vertical levels to 20 km. Then the following one-by-one perturbations to PBL (MYNN 2.5; Nakanishi and Niino (2004)), convection (Grell-Freitas; Grell et al. (2014)), microphysics (Morrison 2-moment; Morrison et al. (2009)), radiation (CAM; Collins et al. (2004)), physics timestep (30 minutes, as in CESM-CAM), radiation timestep (20 minutes, corresponding to the grid spacing), and vertical levels (121) form the ensemble.

Simulations are compared throughout the column and on the tropopause. To compare simulations of each TPV throughout the column, especially given changes to the number of vertical levels, values are linearly interpolated to a reference column with heights from 0 to 20 km with 0.1 km spacing. Height is calculated from pressure hydrostatically. For the tropopause, with a horizontally uniform domain, column PV $q = -gf\frac{\partial\theta}{\partial p}$ for gravity g, Coriolis frequency f, potential temperature θ, and pressure p. The vertical derivative is computed by differentiating a third-order spline of $\theta(p)$. Searching down vertical levels from the model top until 2 PVU is trapped (i.e., the level beneath is less than 2 PVU), tropopause potential temperature is computed by linear interpolation in q to 2 PVU from the neighboring levels (or surface values if the entire column is above 2 PVU).

After 5-d integrations, vertically, heights from 7 to 14 km exhibit the smallest sensitivity to model configuration in terms of range or standard deviation (Fig. 2.8.a). Spread above 14 km is mainly introduced due to changing the number of vertical levels, while

all configurations introduce considerable variations below 7 km with range of O(10 K). Focusing on the diagnosed 2 PVU tropopause (Fig. 2.8.b), the bulk of tropopause potential temperatures from integrating the same initial states with different formulations for the process rates fall within 1 K of the control (96% of all simulations and at least 86% for all simulations within each configuration). The sensitivities among these configurations are not sufficient to generate O(1 K d^{-1}) differences in TPV intensification. Since the expected physical process rates within TPVs are larger (Cavallo and Hakim 2010), they are expected to dominate the uncertainties associated with configurations of individual columns if the latter are non-systematic.

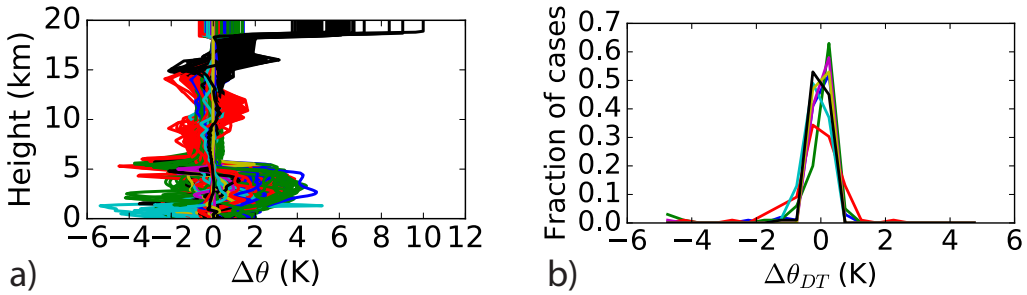

Figure 2.8: *(a) Perturbed minus control potential temperature (K) after 5-d simulations by height for WRF single column model configurations perturbed by convection (blue), microphysics (green), PBL (red), radiation (cyan), Δt_{rad} (magenta), Δt (yellow), and Δz (black). (b) Fraction of cases (100 total within each configuration) with given difference dynamic tropopause potential temperature (K; bin interval 0.5 K) after 5-d simulations. Colors denote model configuration as in (a).*

A greater space can be sampled with these simulations. In addition to perturbed model configurations, initial conditions are available from over O(10^4) distinct TPVs. However, there are strong near-tropopause consistencies among the above 800 simulations, with diminishing increases of confidence from more simulations quantitatively dependent on the underlying distributions (e.g., Krejcie and Morgan (1970)). Alternate surface types and profiles can also be sampled, although several tests with soil categories failed to integrate

when the initial atmospheric and land temperatures vastly differed. Spread in the troposphere suggests that consistency near the tropopause is not caused by a collapse of the ensemble near the surface.

2.3.2.2 Perturbed initial conditions

Returning to the operational intensification errors exhibited in the summer 2007 TPV (Sect. 2.3.1), limited sensitivity in TPV intensity would be expected from perturbed single column model configurations (Sect. 2.3.2.1). Similar perturbed physics SCM experiments initialized from ERA-Interim on 00 UTC 20 July 2007 are consistent with the larger dataset, all within 0.5 K of the control after 3 d (not shown). The following uses the "Control" WRF SCM configuration to quantify impacts of initial condition moisture perturbations on tropopause intensification, with the initial tropopause near 300 hPa.

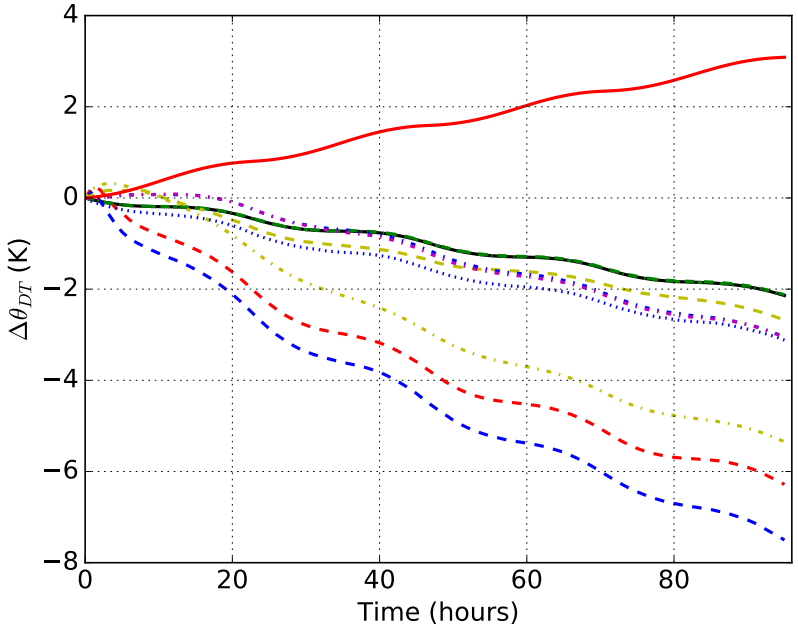

Figure 2.9: *Dynamic tropopause intensification (K) time series for WRF SCM simulations restarted on 00 UTC 21 July 2007, for the control (solid black) and initial condition perturbations to variable (linestyle) and vertical layer(s) (color) defined in Table 2.2. An additional simulation is without longwave radiation (red; solid).*

Variable	Layer	Linestyle
$q_v + 5$ g kg^{-1}	[surface, 300 hPa]	red, dash
$q_v + 5$ g kg^{-1}	[400 hPa, 300 hPa]	blue, dash
$q_v + 5$ g kg^{-1}	[surface, 850 hPa]	green, dash
$q_v + 0.5$ g kg^{-1}	[300 hPa, top]	yellow, dash
$q_v - 0.5$ g kg^{-1}	[300 hPa, top]	yellow, dash-dot
$q_i + 5$ g kg^{-1}	[400 hPa, 300 hPa]	blue, dot
$q_c + 5$ g kg^{-1}	[surface, 850 hPa]	green, dash-dot
$q_c + 5$ g kg^{-1}	[surface, 850 hPa] + [400 hPa, 300 hPa]	magenta, dash-dot

Table 2.2: *Summary of SCM initial condition perturbation experiments.*

Using the restart file output after 1 d of the control integration, experiments are conducted by introducing perturbations within specified vertical layers directly to model state variables of water vapor, cloud ice, and cloud water mixing ratios. The introduced perturbations are not small, in order to realize an impact if a sensitivity exists. An additional simulation is with longwave radiation turned off.

Consider the resulting intensification of the tropopause (Fig. 2.9). Without longwave radiation, the tropopause warms rather than cools as in the control. Longwave radiation causes the SCM cyclone core to intensify. Addition of tropospheric water vapor leads to the greatest rate of intensification, mainly driven by enhanced longwave cooling in the layer with the added moisture (Fig. 2.10). Simulations with added liquid clouds and ice clouds are within 1 K of the control after 3 d, with little added cloud mass persisting for more than 12 h (not shown). These results support Cavallo and Hakim (2013) with the qualification that if clouds vanish rapidly then they have little forcing. In terms of sensitivities to initial conditions, large errors in tropospheric water vapor can generate over 1 K d^{-1} differences in intensification.

2.3.3 Horizontal grid sensitivity of a summer 2006 TPV and surface cyclone

TPV intensification is systematically stronger in the high-resolution than the coarser ensemble members in an operational model (Sect. 2.3.1). Surface cyclone characteristics

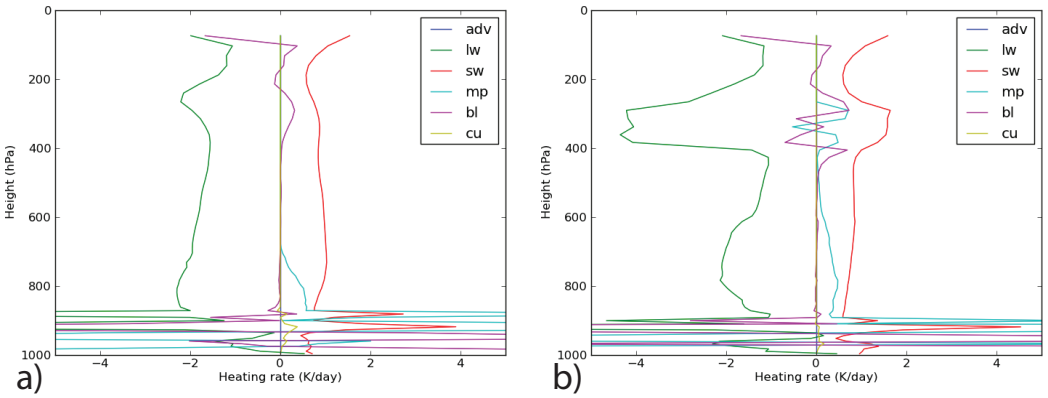

Figure 2.10: *Time-mean WRF SCM heating rates (K d^{-1}) from (a) control and (b) initial $+5$ g kg^{-1} of water vapor in $[400\,hPa, 300\,hPa]$. Tendencies are decomposed into (adv; 0) advection, (lw) longwave radiation, (sw) shortwave radiation, (mp) microphysics, (bl) planetary boundary layer, and (cu) convection.*

such as counts, track densities, and intensities depend on model and resolution (e.g., Jung et al. (2006); Tilinina et al. (2014)). Better understanding the mesh-dependence of the summer 2006 TPV and surface cyclone structure and process rates (Sect. 2.3.3.1) with associated forcings that propagate to sea ice evolution (Sect. 3.3.2) help guide and contextualize the mesh design in future experiments. Especially since variable-resolution allows for flexibility, mesh design could strive to balance sufficient local refinement with a maximum global cost. Note that, given the eventual use within a climate configuration (Sect. 3.1.2) with tuned set of vertical levels, exploration of the sensitivity to vertical resolution is not considered here. In the above SCM experiments, little near-tropopause impact is exhibited.

2.3.3.1 WRF limited area model

To explore the dependence of TPV and surface cyclone structure and process rates on resolution, WRF-ARW version 3.8.1 is used to construct an ensemble of atmospheric, limited area simulations with model grid spacing from 3 to 240 km (or 2000×2000 to 24×24 grid points in the horizontal). The domain is approximately 6000 km by 6000 km in the

horizontal centered on the north pole (Fig. 2.11.a) with 41 vertical levels up to 10 hPa with a time step of $\Delta t = 5\Delta x$ (e.g., 600 s for 120 km). Initial conditions on 00 UTC 15 August 2006 are from the National Center for Environmental Prediction's Global Forecast System (GFS) analysis with lateral boundary conditions updated every 3 h from alternating GFS 6-h analyses and 3-h forecasts (obtained via Rutledge et al. (2006)). Sea surface temperatures and sea ice concentration are constant, as input from the GFS initial conditions. Physics parameterizations include Morrison 2-M microphysics, RRTM-LW, RRTMG-SW, Unified Noah land surface model, and YSU planetary boundary layer. Simulations with greater than 10-km grid-spacing use a modified Tiedtke convective scheme (Zhang et al. 2011a).

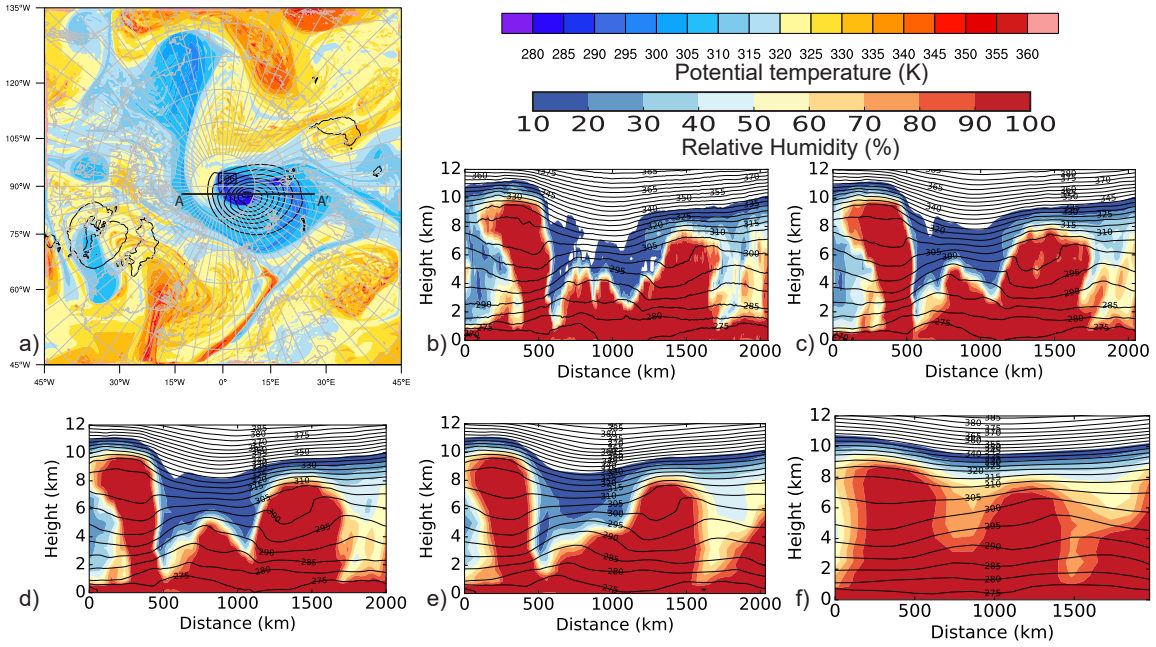

Figure 2.11: *00 UTC 18 August 2006 (a) dynamic tropopause potential temperature (colors in K; 5 K interval) and sea level pressure* $\leq$ 1000 *hPa (contours in hPa; 4 hPa interval) from 12 km WRF simulation, and A-A' vertical cross sections of relative humidity (colors in %; 10% interval) and potential temperature (contours in K; 5 K interval) for (b) 3-, (c) 12-, (d) 24-, (e) 45-, and (f) 120-km WRF simulations after 3 d.*

Synoptically, the tightly coupled TPV and surface cyclone (Sect. 2.5.1) are similarly positioned in the central Arctic in all simulations after 3 d (e.g., Fig. 2.11.a). Structural differences in mass, energy, and momentum variables are reflected in TPV-relative cross sections (Fig. 2.11.b-f). Cross-sections are taken along the model grid centered on the TPV core, with the core defined ad hoc by domain minimum perturbation pressure on model level $\eta = 0.4$ (16^{th} model level near a height of 6.6 km and pressure of 400 hPa). For relative humidity, the moist column at $x = 500$ km is broadest at 120 km, less broad at 45 km, and similar for the smaller grid spacings. The upper level dry intrusion at $x = 1000$ km is more intense with sharper gradients and finer structures as grid spacing decreases. For potential temperature, the contours are progressively smoother as the grid spacing increases. Differences in horizontal winds (not shown) are co-located with differences in the isentropes. Beyond the imposed mesh sampling, finer scales in the states can impact the process rates and TPV intensification, such as modifying vertical gradients in optical depth important in longwave radiative flux.

2.3.3.2 MPAS-A global atmospheric model

To explore whether the limited-area mesh sensitivities are also evident in a global atmospheric model, MPAS-A v4.0 is used with quasi-uniform 30 km and 60 km meshes and zonally variable Arctic-refined and mid-latitude-refined meshes (Fig. 2.12). 41 vertical levels to a model top at 30 km with timestep $\Delta t = 4\Delta x_{min}$ are used on the global domain. Since fewer physics options are available in MPAS-A than WRF, WSM6 microphysics, Tiedtke convection (Tiedtke 1989), RRTMG-LW, RRTMG-SW, Unified Noah land surface model, and YSU planetary boundary layer physics parameterizations are used.

Initializing on 00 UTC 15 August 2006 from ERA-Interim, over 5 d of simulation, the core of the central-Arctic TPV intensifies -5.2 K and -4.7 K in the 30 km and Arctic-refined meshes versus -1.7 K and -1.2 K in the 60 km and mid-latitude-refined meshes. As in WRF (Fig. 2.11), comparing TPV-centered cross-sections between the Arctic- versus

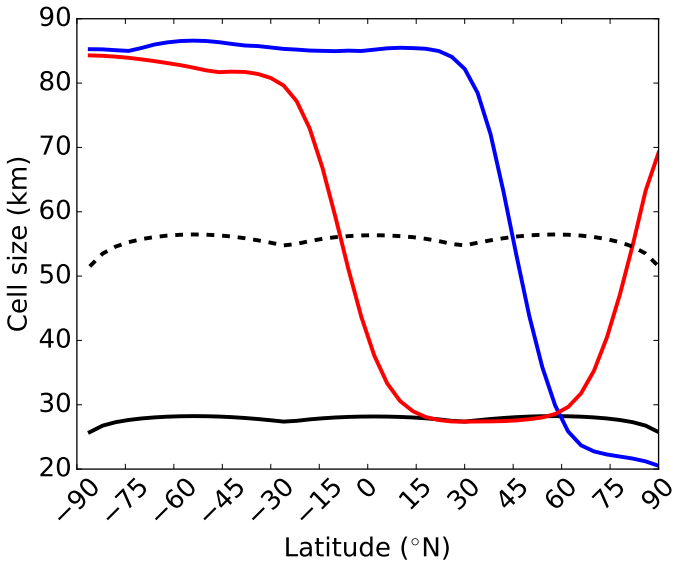

Figure 2.12: *Average grid spacing (square root of cell area) by latitude for quasi-uniform 30-km (solid black), quasi-uniform 60-km (dashed black), Arctic-refined (blue), and mid-latitude refined (red) MPAS meshes.*

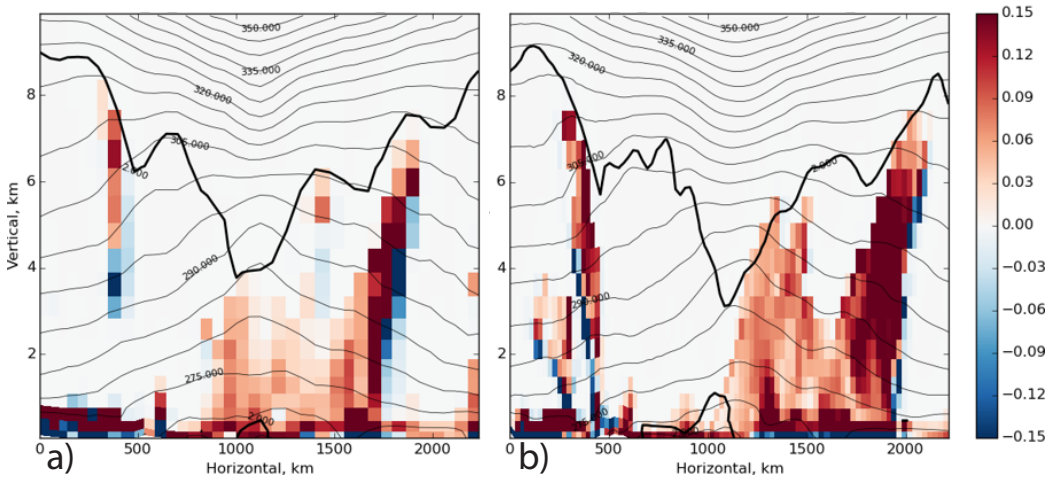

Figure 2.13: *Vertical cross-sections centered on the TPV across* 30° *of latitude of heating rate from microphysics (K* h^{-1}*) on 00 UTC 20 August 2006 after 5-d MPAS-A simulations on (a) mid-latitude-refined and (b) Arctic-refined meshes. Thick black contour denotes 2 PVU. Thin black contours are isentropes (5 K interval).*

mid-latitude-refined meshes (Fig. 2.13) reveals smoothing of features in the locally-coarser mesh. In addition to weakening from diffusion at coarser scales (Mariotti et al. 1994), latent heating is vertically beneath the core in the mid-latitude mesh, versus offset and deeper for the more intense TPV (and near-surface PV maximum). For the TPV in the mid-latitude-refined mesh, the below-tropopause heating reduces upper tropospheric stability, consistent with destruction of PV and a relatively weaker vortex. Note that intensities of the TPV in additional perturbed physics simulations (to convection (Kain-Fritsch), radiation (CAM), or a modified longwave water vapor continuum absorption model (Turner et al. 2012)) from the 30 km control are less than 1 K, further supporting the perturbed configuration SCM results (Sect. 2.3.2.1). TPVs in experiments with a hierarchy of model complexity exhibit little sensitivity to physics options and larger differences in structure and process rates to model states and horizontal mesh spacing, with finer features evident at higher resolution.

2.4 Tendency-based TPV modification

Sensitivity experiments using a realistic, coupled process model with perturbed TPVs may permit quantification of the sensitivities (e.g., of sea ice) to the TPV perturbations, the mechanisms, and their significance and robustness. Initial condition sensitivity experiments with prescribed input perturbations to TPVs are one strategy. For a perfect model, differences in model simulations arise from differences in initial conditions and corresponding error growth (e.g., Lorenz (1969b); Judt (2018)). For input perturbations (to TPVs) at synoptic-scale or below (e.g., Browning et al. (2000)), chaotic growth of differences would be expected to convolute impacts caused by the initial perturbation (and attribution) beyond several weeks, since it would be no less rapid than error growth from smaller scales (Durran and Gingrich 2014). Towards quantifying the impacts of TPVs over longer periods, we systematically modify the model by introducing an additional tendency to a state variable X:

$$\frac{\partial X}{\partial t}_{\text{experiment}} = \frac{\partial X}{\partial t}_{\text{dynamics}} + \frac{\partial X}{\partial t}_{\text{physics}} + F_{\text{TPV}} \tag{2.1}$$

where a TPV-associated perturbation $F_{\mathrm{TPV}} = W_{\mathrm{TPV}} \frac{\partial X}{\partial t}_{\mathrm{TPV}}$ is introduced in the interface from CAM to the MPAS dynamical core like a tendency from a physics parameterization described by a spatial weight W and tendency. Specifying F_{TPV} requires formulation of the spatial weight and applied perturbation tendency to, for examples, X the modified moist potential temperature, C-grid velocity, or mixing ratio model variables in MPAS-A.

Several approaches exist to define TPVs for tracking diagnostically from model output (Hakim and Canavan 2005; Kew et al. 2010; Szapiro and Cavallo 2018). The task in model space is to identify those grid cells in the horizontal and vertical to be directly modified. With access to the full model state and history, any approach may be applied. For one instance in time over a proper subset of the domain (e.g., during an integration over multiple processors using domain decomposition with quasi-instantaneous model state), practical definitions may be more reproducible across a wider range of models.

Fig. 2.14.a,b illustrates an example of a binary TPV weight defined horizontally by dynamic tropopause potential temperature ($\theta_{DT} < 305$ K) and vertically by distance from the column's tropopause in terms of potential temperature ($\theta \in [\theta_{DT} - 10, \theta_{DT})$ K). Explicitly, $W_{\mathrm{TPV}}(x,y,z) = (\theta_{DT}(x,y) \geq 305 \text{ K}) \cdot (\theta(x,y,z) \geq \theta_{DT}) \cdot (\theta(x,y,z) < \theta_{DT} - 10 \text{ K})$ in a boolean sense where True is 1 and False is 0. Inclusive or exclusive endpoints tend to be unimportant given the rarity of two bit-equal floating point numbers. Alternately, regions of initialized passive tracers have also been used to prescribe the regions to modify. Trapping of fluid within the vortex then allows genesis and control of the feature through direct modification (Sect. 2.4.2).

2.4.1 Applied tendency

Under integration, TPV profiles illustrate the impacts of added tendencies, for example $\frac{\partial X}{\partial t}_{\mathrm{TPV}} = \frac{\partial \theta}{\partial t}$ within a binary TPV spatial weight (Fig. 2.14.c). The instantaneous shape of the control TPV is characterized by a dominant 1000 km scale undulation with a sharper

left (southern) edge, cooling to the core, and broader warming to the right (north). Below-tropopause heating warms the profile, with flattening corresponding to the imposed relaxation. Below-tropopause cooling increases the TPV's intensity, with a sharper left edge cooling more over a shorter distance, an interior offset cooler, and right edge warming to the same intensity. Relaxation cooling versus a uniform tendency directly amplifies the minimum as larger deviations of the tropopause receive larger tendencies. Spurious artifacts from the binary spatial weight are not evident (e.g., "ringing" at the edges), possibly products of steadily applying the tendencies throughout the integration (e.g., Bloom et al. (1996)) or sharpening of the edge through vortex stripping (e.g., Legras et al. (2001)). The response to a range of uniform cooling rates (Fig. 2.14.d) appears monotonic with the rate, with -10 K d^{-1} of additional cooling resulting in a -10.5 K cooler core after 1 d.

2.4.2 Examples of TPV modifications

In addition to heating rate tendencies applied within regions of specified tropopause potential temperature, a number of other strategies for TPV modifications are possible. The following illustrates several alternatives using the stand-alone MPAS-A v4.0. Table 2.3 summarizes the explored tendency-based TPV modifications.

Initialized passive tracers can be used to flag cells subsequently within transported regions. Heating rates applied within these tracer regions can generate, intensify, and maintain new TPVs (Fig. 2.15). Continual addition of water vapor beneath the tropopause generates large latent heating rates leading to coherent anticyclonic TPVs under integration (Fig. 2.16).

Individual vortices can also be tracked over time. Finding the diagnosed core of a cyclonic TPV as the regional minimum in θ_{DT} near the core from the previous timestep, imposed vorticity tendencies can counteract or reinforce the cyclone (Fig. 2.17). Tendencies can also be more complexly calculated rather than prescribed. One option is to modify the states input into the physics parameterizations without changing the actual model state.

In an example case (Fig. 2.18), longwave cooling associated with the water vapor profile causes the TPV intensification. Thus, the TPV modifications can be used to (1) change the shapes of TPVs within simulations and (2) explore the roles of potential driving mechanisms.

Description	Variables	Effects on TPV
No water vapor for lwrad in vortex	lwrad(q_v)	With lwrad($q_v = 0$), no intensification and rapid surface cooling
Heating in upper troposphere in vortex	θ_m	Heating (cooling) diabatically weakens (strengthens) vortex
Heating in lower stratosphere in vortex	θ_m	Heating (cooling) diabatically strengthens (weakens) vortex
Heating in lower troposphere or upper stratosphere in vortex	θ_m	No rapid effects unless trigger convection
Heating in upper troposphere in advected tracer	θ_m	Cooling (heating) diabatically forms (anti-)cyclones. Scalar largely trapped in vortex.
Moisten upper troposphere in vortex	q_v	Latent heating diabatically weakens vortex
Add clouds in troposphere in vortex	q_c, q_i	If evaporate, like q_v. If precipitate, little effect.
Force near-tropopause vortex circulation	u, v	Amplifying (countering) core-relative vorticity frictionally strengthens (weakens) vortex
Force vortex translation	u, v	Ineffective, with gross artifacts of divergence near vortex edge for large tendencies

Table 2.3: *Summary of tested TPV modification strategies, with a description of each strategy, model variables (tendencies) modified, and brief comments on the main effects. Variables are longwave radiation lwrad, modified moist potential temperature θ_m, mixing ratio of water vapor, cloud, or ice $q_{v,c,i}$, respectively, zonal velocity u, and meridional velocity v.*

2.4.3 Discussion of TPV modifications

Impacts from the explored TPV modifications (Table 2.3) are qualitatively consistent with a PV perspective, where heating rates and vorticity tendencies can modify TPV intensities.

Heating (cooling) beneath the tropopause weakens (strengthens) a cyclone. The opposite occurs for heating above the tropopause or for anticyclones. Impacts from moisture occur through heating rates. Moreover, artificial heating rates applied near the tropopause are (1) quantitatively effective at dynamically modifying TPVs since change in TPV intensity is consistent with the added heating rate and (2) directly localized to the TPV by construction. An imposed cooling is an energy sink, within the TPV of scale (Eqn. 2.2)

$$\frac{DQ}{Dt} \approx mc\frac{DT}{Dt} \approx -10^{13}\ J\ s^{-1} \rightarrow -50\ W\ m^{-2} \tag{2.2}$$

for heating rate $\frac{DT}{Dt} = -10\ K\ d^{-1}$, mass $m = \rho(\Delta x \Delta y)\Delta z = 0.4\ kg\ m^{-3} \times \pi(300\ km)^2 \times 1\ km$, and specific heat $c = 1\ kJ\ kg^{-1}\ K^{-1}$. Considered over the global domain, the input energy sink is $-0.1\ W\ m^{-2}$. Incorporating additional conservation constraints to the tendencies modifying TPVs may be important for longer simulations or smaller domains to avoid climatic drift (e.g., Gupta et al. (2012)) from the introduced perturbations. Compensating tendencies could be introduced in the same columns or elsewhere. Since global conservation could be "fixed" using balancing perturbations with presumably little impact on the variables of interest here (for example, compensating tendencies far from the Arctic to deep soil or ocean), it is not deemed necessary here.

A small set of case studies suggest limits on size but not lifetime for a modified TPV that can be artificially maintained. In TPV modification experiments that drive the tropopause to the surface (e.g., -50 K d^{-1} below-tropopause cooling), mature surface cyclones persist on the enclosing PV wall. The coupled surface cyclones have large mid-tropospheric latent heating, bounding growth of the horizontal extent of the TPV (Fig. 2.19). Tendencies applied using passive tracers within smooth initial fields can create new TPVs lasting for the duration of several week simulations. Similarly, TPVs from geographic tendencies fixed over the pole can also be long-lived. For TPVs that dissipate or newly form, TPV identification based on neighborhood criteria from a past state is less reliable. Since core-relative (vorticity) tendencies require identification of a core and passive tracers follow the initial seeding, both are most applicable for modifying existing TPVs.

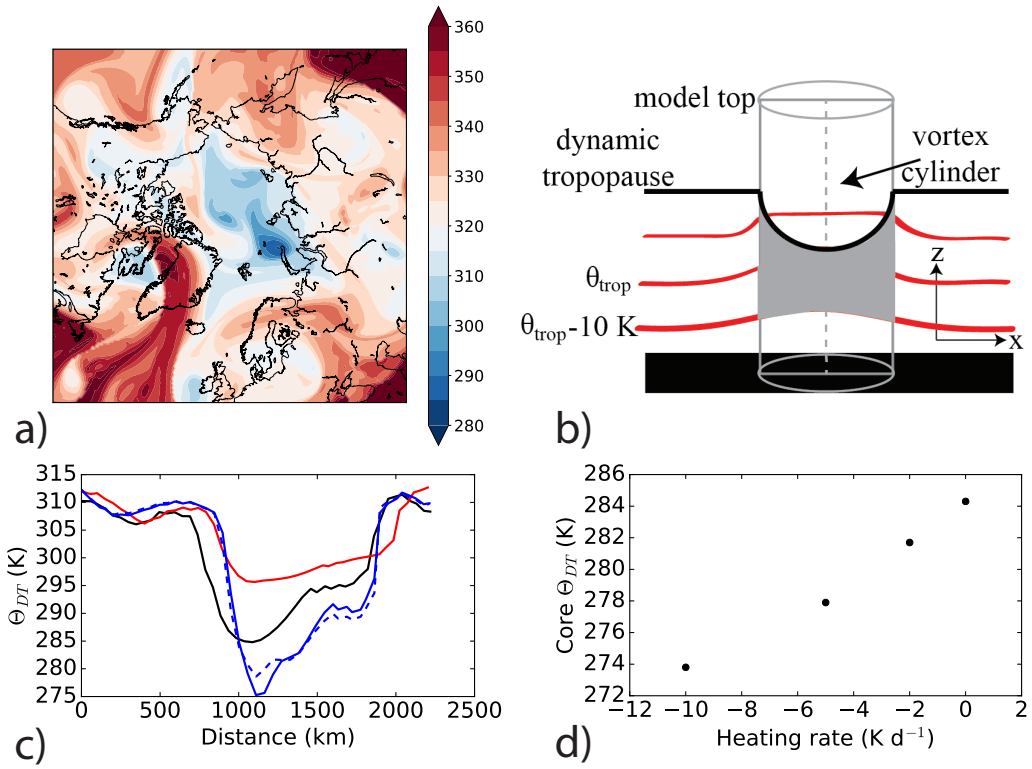

Figure 2.14: *Summary of heating tendency-based TPV modifications. (a) Tropopause potential temperature from quasi-uniform 60-km CESM-CAM-MPAS on 00 UTC 16 August 2006 (K, 5 K interval). (b) Schematic of binary TPV weight (gray) localized horizontally by a tropopause potential temperature threshold and vertically to 10 K beneath the tropopause. (c) South to north profiles (tropopause potential temperature; K) centered on the TPV (near 77 °N, 65 °E) after one simulation day under varying TPV modifications of (black) control, (red)* $(\theta_{ref} - \theta_{DT})$ *K* d^{-1}*, (solid blue)* $-\frac{1}{3}(\theta_{ref} - \theta_{DT})$ *K* d^{-1}*, and (dashed blue)* -5 *K* d^{-1} *for* $\theta_{ref} = 305$ *K. (d) TPV core potential temperature after 1-d simulations as a function of uniform heating rate TPV modifications (as for the dashed blue in c). TPV modifications for c,d are localized as in b.*

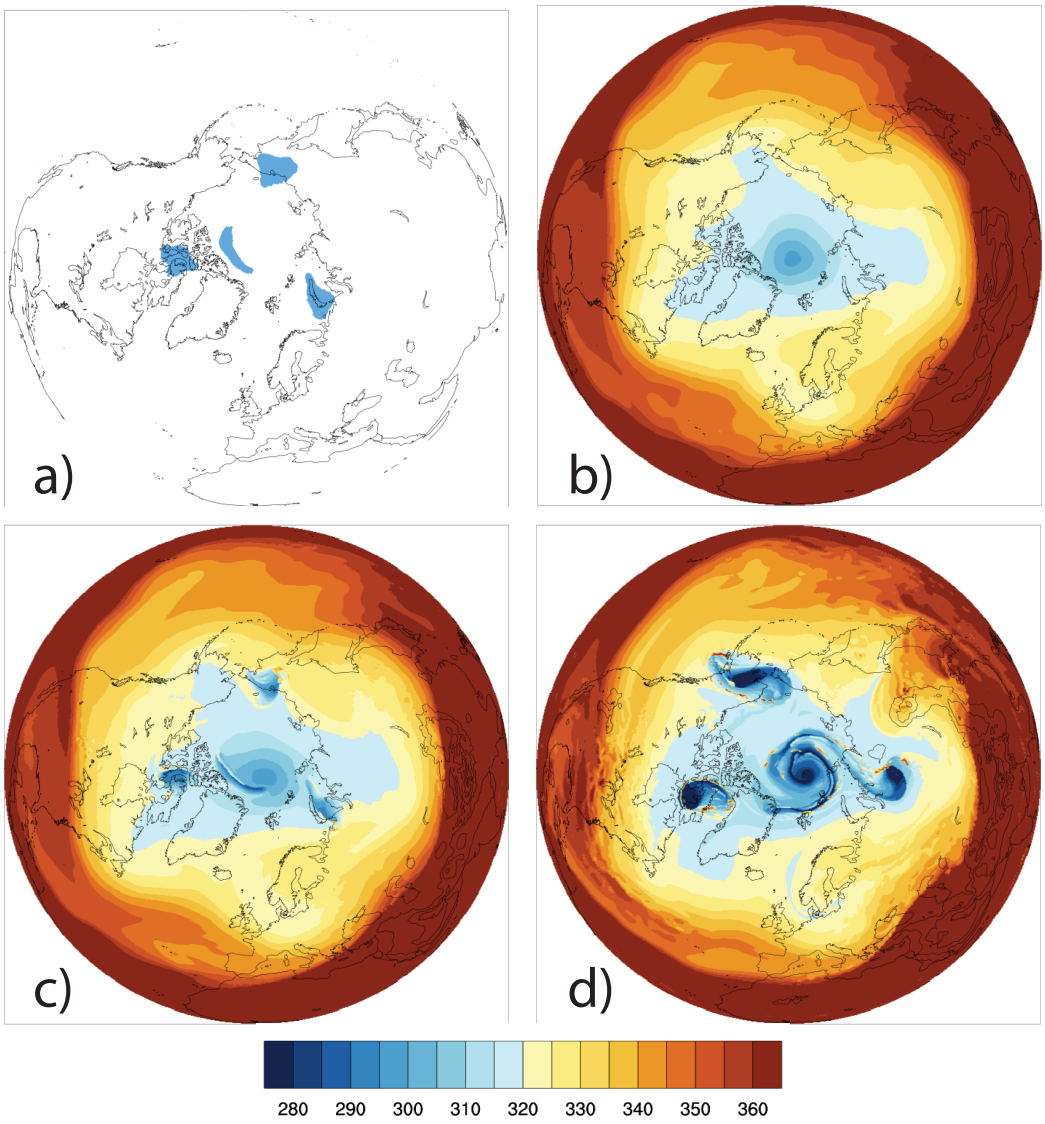

Figure 2.15: *Example TPV modification applying additional heating (± 20 K d^{-1} above/below the tropopause) within regions of an initialized passive tracer. (a) Initialized passive tracer after 6 h. (b,c,d) Tropopause potential temperature (K; 5 K interval) after 0 d, 1 d, and 3 d. Initial conditions are from the monthly mean of August 2006 from ERA-Interim containing only a smooth, planetary-scale polar vortex. The tropopause is identified above the highest level below 2 PVU, not via flood fill.*

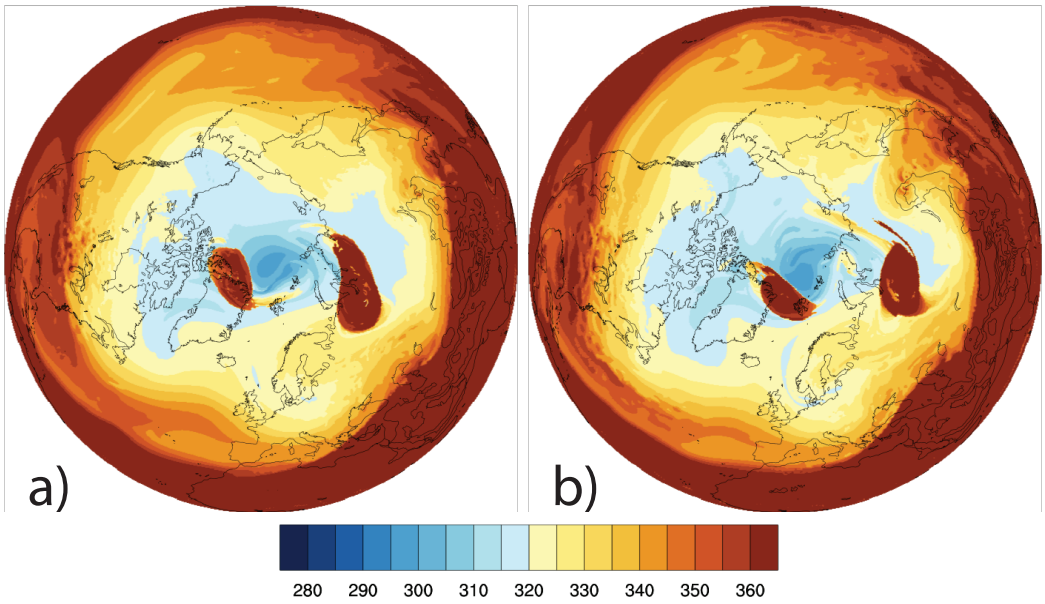

Figure 2.16: *Example TPV modification applying added water vapor mixing ratio* ($+20\ g\ kg^{-1}\ d^{-1}$ *in* $[\theta_{DT} - 20\ K, \theta_{DT}]$) *within regions of an initialized passive tracer. (a,b) Tropopause potential temperature (K; 5 K interval) after 1 d and 2 d. Initial conditions are from the monthly mean of August 2006 from ERA-Interim containing only a smooth, planetary-scale polar vortex. Note that the initial passive tracer is different than in Fig. 2.15, with only two regions here.*

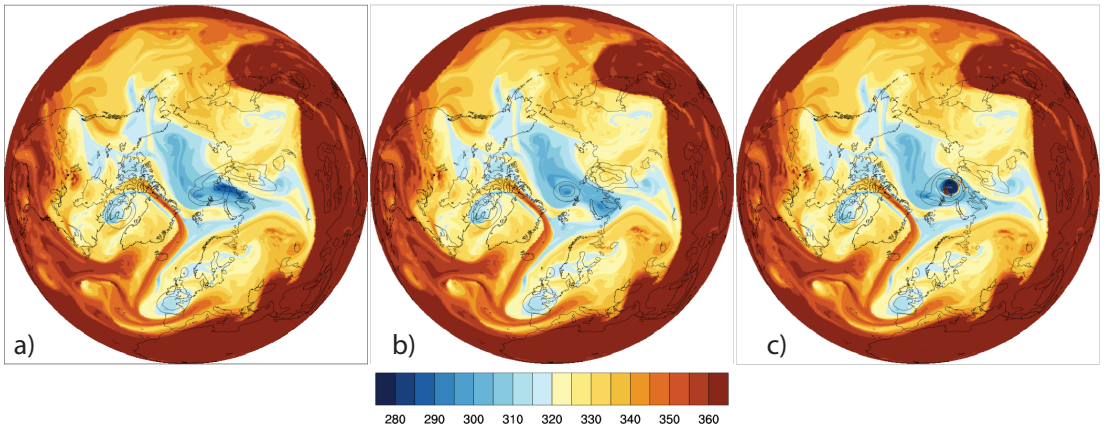

Figure 2.17: *Example TPV modification applying vorticity tendencies through horizontal wind tendencies* ($\pm(\vec{u}-\vec{u_0})\ d^{-1}$ *in* $[\theta_{DT}-20\ K, \theta_{DT}+10\ K)$) *about a tracked cyclonic TPV core with horizontal wind* $\vec{u_0}$. *Tropopause potential temperature (K, colors in 5 K intervals) and mean sea level pressure* $\leq$ *1004 hPa (hPa, contours in 4 hPa intervals) maps are plotted after 2 d for the (a) control, (b) anticyclonic tendency, and (c) cyclonic tendency. The selected TPV is the most intense one northeast of Novaya Zemlya in the control. Initial conditions on 00 UTC 15 August 2006 are from ERA-Interim. The tropopause is identified above the highest level below 2 PVU, not via flood fill.*

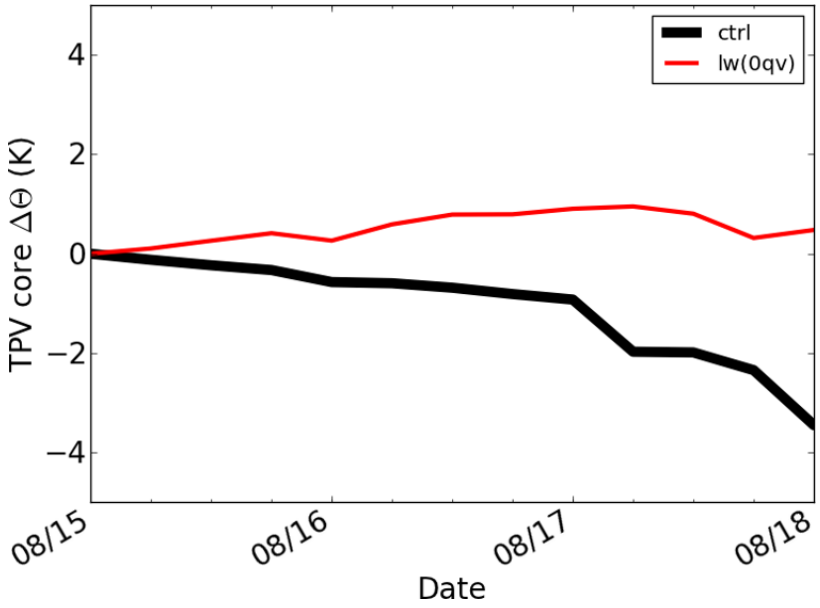

Figure 2.18: *Example TPV modification of denying water vapor throughout the column within the TPV for the profile used in calculating longwave radiation. Plotted time series for change from initial TPV core* θ_{DT} *for the (black) control and (red) experiment intensify and slightly weaken, respectively. Initial conditions on 00 UTC 15 August 2006 are from ERA-Interim.*

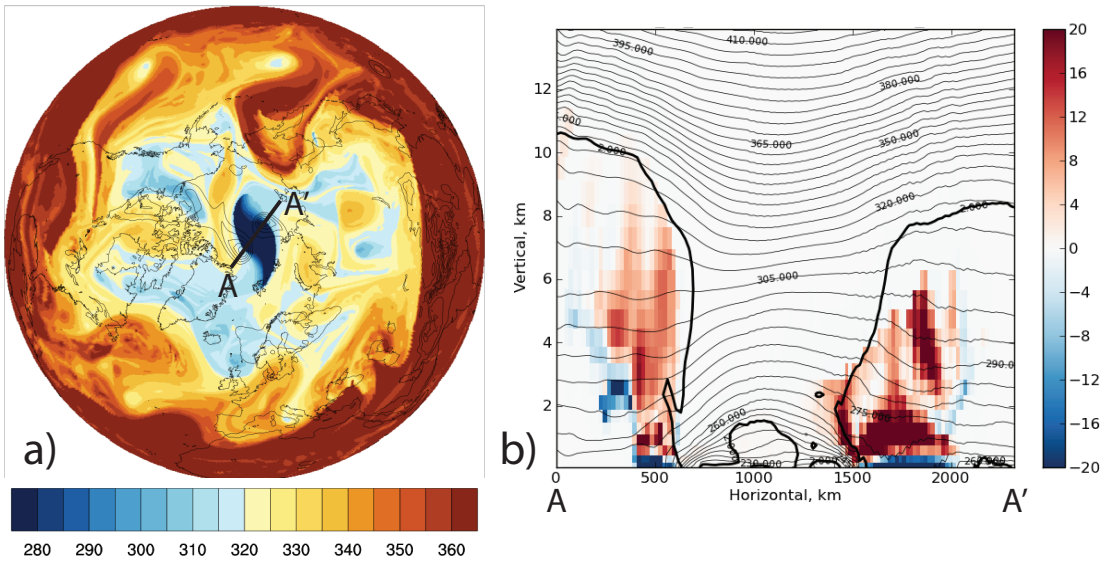

Figure 2.19: *Snapshot after 8.5 d of MPAS-A TPV modification experiment with -20 K* d^{-1} *cooling in the troposphere under* $\theta_{DT} < 300$ *K. (a) Tropopause potential temperature (K, colors in 5 K intervals) and mean sea level pressure* $\leq$ *1004 hPa (hPa, contours in 4 hPa intervals). (b) Vertical A-A' cross-section of heating rate from microphyics (color; K* $d-1$*) with isentropes (thin black; 5 K spacing) and 2 PVU contour (thick black). Initial conditions on 00 UTC 15 August 2006 are from ERA-Interim.*

2.5 Potential mechanisms for TPVs to impact sea ice change

The following highlights mechanisms to propose that (the shapes of) TPVs may be able to impact sea ice variability from days through seasons, directly and indirectly. Directly, TPVs and their associated anomalies may reach the surface, depending on the location and scale of the induced circulation (e.g., Thorpe (1986)). Considering the composite mean structure of a cyclonic TPV (Cavallo and Hakim 2010), colder temperatures are expected to reduce the sensible heat and downwelling radiative flux into the ice. Higher relative humidity and increased cloudiness decrease shortwave and increase longwave downwelling radiation (e.g., Intrieri et al. (2002)). Enhanced winds increase latent and sensible heat fluxes at the surface (Friehe and Schmitt 1976).

Indirectly, TPVs can couple with surface cyclones, the polar jet, and the mean circulation leading to sea ice impacts. Theoretically, TPVs can play a central role in surface cyclogenesis and intensification as the upper-level precursor disturbance (Eady 1949; Petterssen and Smebye 1971) or anomaly (Hoskins et al. 1985) over a surface baroclinic zone. The Eady growth rate (Eady 1949)

$$E_{GR} = 0.3098 g \frac{|f|}{N} \left| \frac{\partial u}{\partial z} \right| \tag{2.3}$$

where g is gravitational acceleration, f is Coriolis frequency, N is the Brunt-Väisälä frequency, u is horizontal wind, and z is height encapsulates a simplified, idealized relationship between lower- and upper-tropospheric layers. The measure of baroclinic instability is greater for reduced static stability and increased vertical wind shear. Increasing the intensity of a cyclonic TPV then directly increases E_{GR} by lowering of a cooler tropopause and increased upper-level winds consistent with a thermal wind relationship. The structure, dynamics, and prediction of individual surface cyclones can be intimately tied to TPVs (e.g., Simmonds and Rudeva (2014); Yamazaki et al. (2015); Tao et al. (2017); Yamagami et al. (2018)). Episodic storms apparently drive local sea ice concentration change with larger loss from stronger surface cyclones (Kriegsmann and Brümmer 2014). Both mechanical

and thermodynamic processes contribute to the linkages between storms and sea ice loss (McPhee et al. 2005; Asplin et al. 2012; Zhang et al. 2013; Boisvert et al. 2016; Itkin et al. 2017). Moreover, cyclones at lower latitudes can inject extratropical air masses to the Arctic that can locally enhance downwelling shortwave and longwave radiation and generate mean anticyclonic circulations in the Arctic (Wernli and Papritz 2018). Surface cyclones also respond and contribute to the anomalous summer mean (anti)cyclonic patterns corresponding to anomalous ice gain (loss) (Screen et al. 2011; Knudsen et al. 2015). Like surface cyclones, TPVs can interact with the mean flow by following the larger-scale circulation and contributing eddy tendencies, with an individual long-lived TPV sufficient to contribute a seasonal-scale anomaly (Sect. 2.5.1). Regarding TPVs near the polar eddy-driven jet (Hartmann 2004), the introduced anomaly and enhanced PV gradients can strengthen wind speeds (Pyle et al. 2004) or induce amplified waviness (Wirth et al. 2018), with feedbacks to circulation patterns potentially driving sea ice variability like the Arctic Oscillation (Rigor et al. 2002) or Arctic Dipole (Wang et al. 2009).

2.5.1 August 2006 very rapid ice loss event and Summer 2006 TPV

Historical events in summer 2006 illustrate aspects of the above mechanisms. On 21 August 2006, microwave satellite imagery (Fig. 2.20.a; Spreen et al. (2008)) shows reduced sea ice cover in the central Eurasian Basin (in $[80,90]$ °N $\times$ $[0,90]$ °E). The change in SIE from 2 d before (Fetterer et al. (2017); 2-d records before 20 August 1987) of -0.29 M km^2 is the 1.15% smallest change (i.e., largest loss) in 1979 to 2016. With a high-pass SIE ($<$ 18 d Butterworth filter), 0.54% of dates have a larger 2 d high-pass loss than the corresponding -0.2 M km^2. However, note that effects from weather (Maslanik 1992) and open water (Kwok 2002) contribute uncertainties in sea ice concentration derived from passive microwave, with impacts from surface melt in summer (Cavalieri et al. 1990). Errors can exceed $\pm$20% concentration (Ivanova et al. 2015).

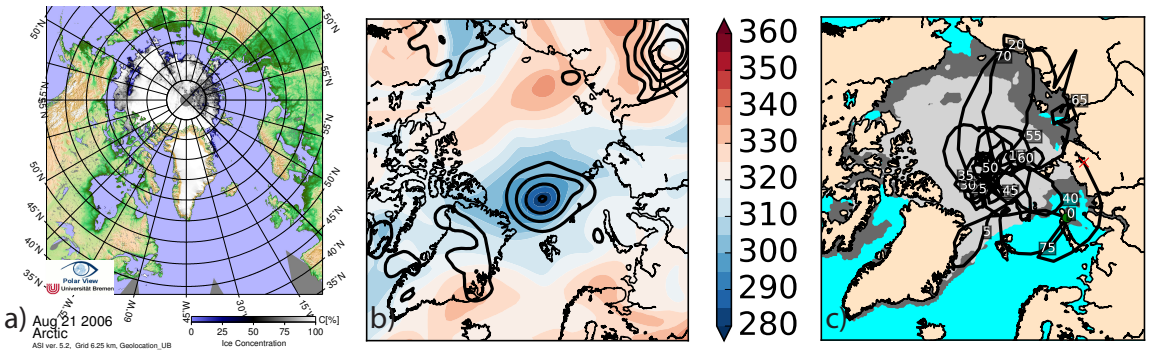

Figure 2.20: *(a) 21 August 2006 sea ice concentration (Spreen et al. (2008), via University of Bremen). (b) 00 UTC 21 August 2006 tropopause potential temperature (K, 5 K interval) and mean sea level pressure $\leq$ 1004 hPa (hPa, 4 hPa interval). (c) TPV track over 06 July (dark gray) to 17 September 2006 (light gray) sea ice concentration of at least 15%. TPV's lifetime in days is annotated every 5 days.*

Overlying and west of the rapid, extreme sea ice loss is a surface cyclone (Fig. 2.20.b), with a lifetime of at least 12 days (Serreze 2009). Conceptually, northward flow to the east of the cyclone (with the anticyclone further east further enhancing the zonal pressure gradient) would transport air from over the ocean to over the ice as well as advect marginal ice towards the central Arctic. Circulating with the surface cyclone for all of its tracked life is one extremely long-lived cyclonic TPV, manually tracked for 86 days. Over the automatically tracked TPV's life (Szapiro and Cavallo 2018), the core traverses much of the central and eastern Arctic (Fig. 2.20.c), and geometric metrics (Fig. 2.21) quantify its exhibited range of synoptic and smaller scales. Time series of the tracked TPV's metrics are not smooth, with apparent multi-day, episodic oscillations. An extended period covering August of core potential temperature cooling averages weaker than -1 K d^{-1}. Radius and amplitude changes of O(100 km) and O(10 K) are often coincident, possibly from deformation during multiple vortex interactions. Forward speed increases near the end of the track as the TPV nears the polar jet.

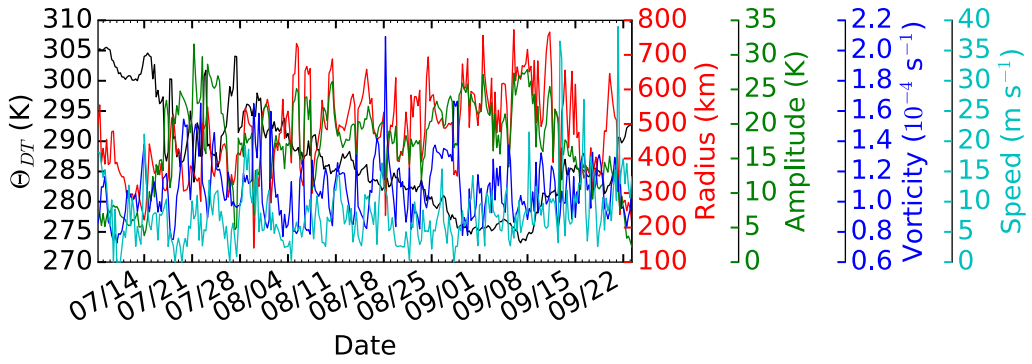

Figure 2.21: *Tracked summer 2006 TPV radius (red; km), amplitude (green, K), vertical vorticity (blue, s^{-1}), and forward speed (cyan, m s^{-1}) as a function of date over its tracked lifetime.*

While components of the August 2006 ice loss event are extreme, note that the conditions are not unique. For example, observations of a similarly located concentration loss event in 2010 are documented in Kawaguchi et al. (2012), where winds associated with a mid-August synoptic-scale surface low force ice divergence that enhances the absorption of shortwave radiation at the surface through more exposure of the darker ocean. On further inspection, the 2010 persistent surface low is also coincident with TPVs (not shown). Surface cyclones with overlying TPVs are frequently present near large several-day sea ice losses (Frank 2019).

To diagnose the role of the TPV in the summer 2006 circulation, the tracked feature is used as a horizontal mask to accumulate coincident fields. In order to capture the coincident (sub)synoptic variability, the spatially varying expected anomaly for a field θ associated with a TPV is defined as Eq. 2.4:

$$E[\theta'(x)] = \frac{1}{n(x)} \sum_{n(x)} \theta(x) - \bar{\theta}(x)_{\text{climo}} - \bar{\theta}(x)_{\text{season}} \tag{2.4}$$

for geographic or core-relative location x inside a TPV n times, climatological value for the datetime of the year $\bar{\theta}(x)_{\text{climo}}$ from a 1979 to 2014 mean, and seasonal anomaly $\bar{\theta}(x)_{\text{season}}$ of the year with respect to the climatological mean. The $\bar{\theta}$ adjustments discount long term, intraseasonal, and diurnal variations. Geographically, the single long-lived TPV contributes

-2 to -5 K to the summer 2006 tropopause potential temperature anomaly near the pole (Fig. 2.22). Patterns in anomalous downwelling longwave (shortwave) radiation (Fig. 2.23) correspond to anomalous total column liquid water (cloud ice) (Fig. 2.24.b,c). As would occur for a cooler column underneath the lower tropopause, total column water vapor is less within the TPV (Fig. 2.24.a).

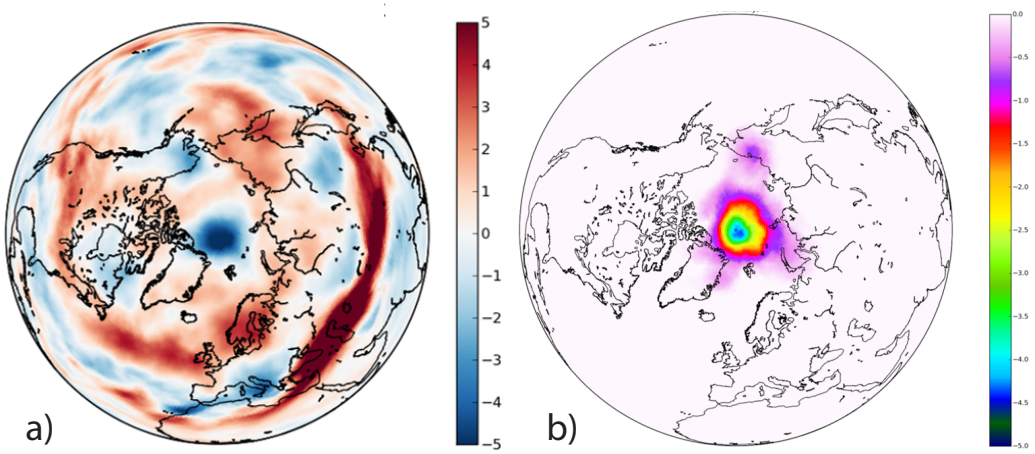

Figure 2.22: *(a) Summer 2006 seasonal anomaly in tropopause potential temperature (K) from the 1979 to 2014 summer mean. (b) Contribution of the long-lived 2006 TPV to the summer tropopause potential temperature anomaly (K).* $\frac{n(x)}{N} \cdot E[\theta'_{DT}(x)]$ *(Eq. 2.4) for N total times in the period. Data are from ERA-Interim.*

Attribution (of the degree) that TPVs cause changes in sea ice or the mean circulation requires further testing. Since nonlinear forcings and coupled feedbacks to transient features across integrated timescales with possible tilting in the vertical characterize the possible interactions, causal, dynamical model experiments are pursued.

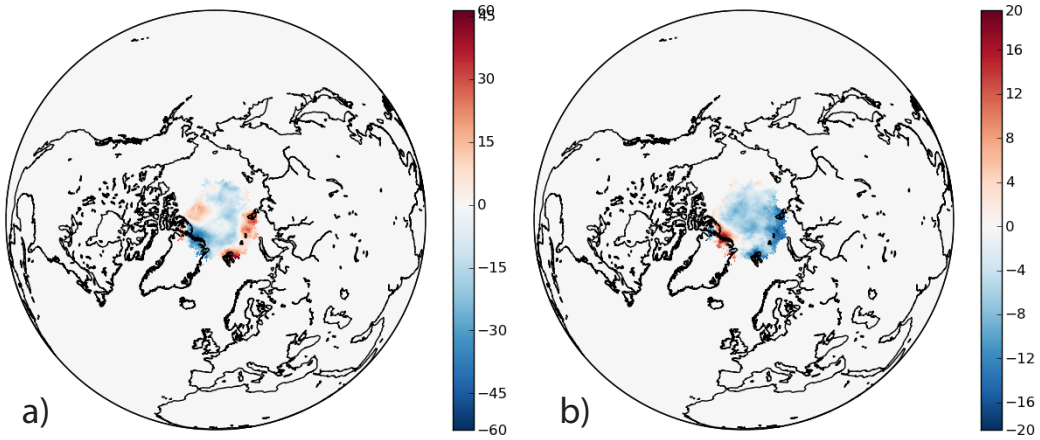

Figure 2.23: *Expected anomalous downwelling (a) shortwave and (b) longwave radiation (W m^{-2}) coincident with the long-lived 2006 TPV in summer 2006. Colorbars differ. Locations with fewer than 2 weeks of samples are not plotted. Data are from ERA-Interim.*

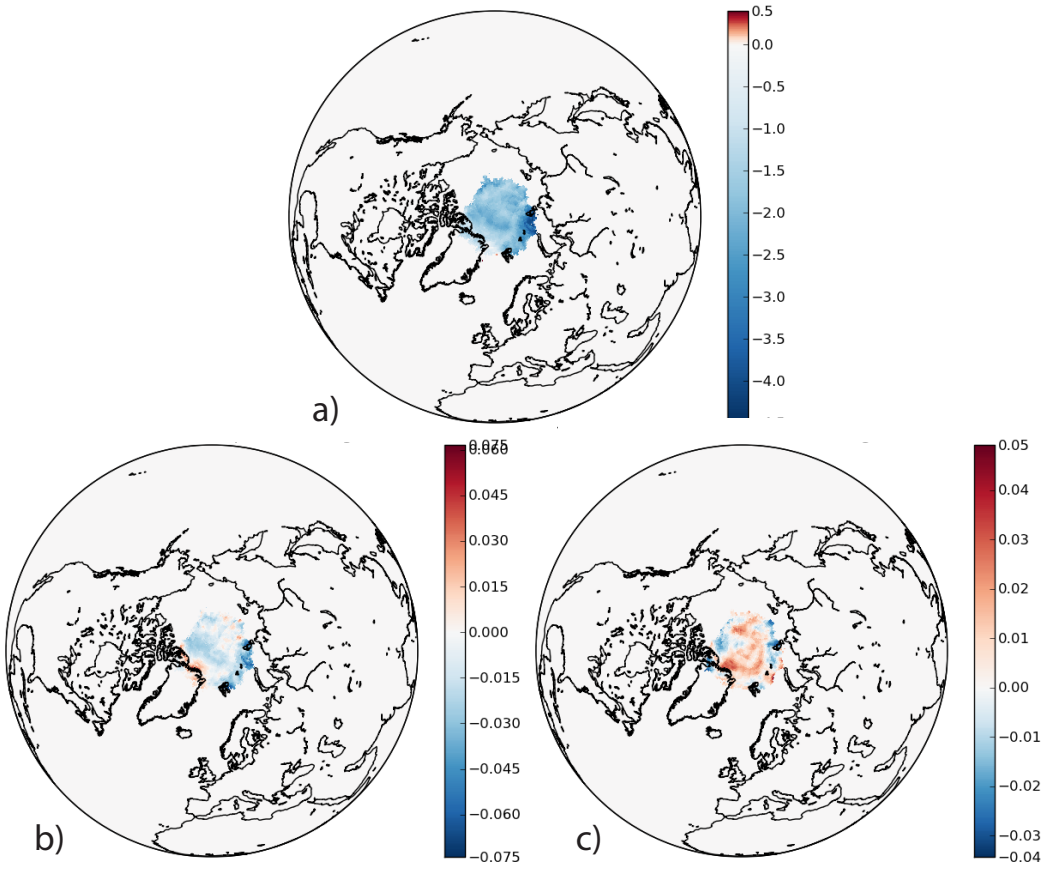

Figure 2.24: *Expected anomalous total column (a) water vapor, (b) liquid water, and (c) cloud ice (kg m^{-2}) coincident with the long-lived 2006 TPV in summer 2006. Colorbars differ and are not symmetric. Locations with fewer than 2 weeks of samples are not plotted. Data are from ERA-Interim.*

Chapter 3

Model capabilities to represent impacts of TPVs on sea ice change

Since a closed model defines the relationships among all of its components, model design is fundamental. Representing the hypothesized mechanisms for TPVs to impact sea ice change (Sect. 2.5) in the Arctic of the Earth system imposes several related requirements on a model:

- Representation of TPVs
- Feedbacks between Arctic and extra-Arctic latitudes from the surface through the tropopause
- Atmospheric spatial scales cover O($<$ 100 km, 5000 km)
- Temporal integration covers O($<$day,season)
- Consistent coupling of realistically evolving sea ice
- Sufficient computational efficiency to be able to conduct experiments

as individual TPVs, the mean summer polar circulation, and corresponding sea ice evolution are all among what must be included. Coverage of (feedbacks with) the meandering polar jet and summer polar circulation motivate the extents of the larger scales. For the finer scales, recommendations for minimum resolution of air–sea fluxes are application dependent, typically 3 h and 50 km but higher-resolution for high-impact weather (WGASF 2000; Bourassa et al. 2013). The following describes limitations of existing approaches and a model (Sect. 3.1) satisfying these stated necessary conditions to qualified degrees for the atmosphere (Sect. 3.2), sea ice (Sect. 3.3), and computations (Sect. 3.4) with supporting arguments.

While the Earth system exhibits interactions across a continuum of spatial and temporal scales, traditional modeling relies on ideas of scale separation (Stensrud 2009) and artificial boundaries (Brunet et al. 2010). Two categories of models used for process and prediction experiments are limited area models (LAMs) and general circulation models (GCMs) (e.g., Maslowski et al. (2012)). Particularly problematic for the potentially integrated linkages between TPVs and sea ice, existing LAM and GCM tools exhibit systematic artifacts tied to their constructions.

GCM simulations are relatively coarse in order to reduce the expense of simulations (e.g., Small et al. (2014)). With coarse resolution in the Arctic, simulated surface cyclones and TPVs are systematically filtered to exclude smaller-scale processes or high frequency variability (Sect. 2.3.3). Excluding higher frequency variability extends to sea ice as well (Sect. 3.3.1).

By reducing the extent of the computational domain, LAMs reduce the cost of simulations. Fundamentally, the introduced boundaries in LAMs inconsistently couple domains (e.g., Laprise et al. (2008); Park et al. (2014)) with treatment of boundary conditions a central issue (Rummukainen 2010; Giorgi and Gutowski Jr 2015). Realistic LAMs need to introduce external information near the artificial lateral boundaries of the domain (e.g., Davies (1976)). The resulting sensitivity to boundary data depends on domain size: for small area domains, imposed information from lateral boundaries can dominate internal, smaller scale features; for large domains, circulations inconsistent with the boundary data can develop (Leduc and Laprise 2009). Nudging within domains to known large scales can reduce the mismatches (Miguez-Macho et al. 2004). Since a central aim here is to explore the evolution of local TPV changes to possibly polar-scale differences unknown a priori, it is difficult to justify any lateral boundary conditions or interior nudging and (sensitivities to) candidate strategies would need to be evaluated.

Stimulated by increased computational capacity, bridging the seam between GCMs and LAMs is a generation of global, variable-resolution models (Ullrich et al. 2017). The

atmospheric component of the Model for Prediction Across Scales (MPAS-A) is a fully compressible non-hydrostatic atmospheric model discretized using unstructured centroidal Voronoi meshes incorporating split-explicit time-integration (Skamarock et al. 2012). The Community Earth System Model (CESM) is a fully-coupled, community global climate model that provides state-of-the-art computer simulations of the Earth's past, present, and future climate states (Hurrell et al. 2013). The main appeals to their combination are to leverage a global atmospheric dynamical core with transport, time integration, and filtering design guided by theory and practical experience in weather modeling (Skamarock et al. 2012) without additional polar filtering (e.g., Neale et al. (2010), Sect. 3.1.4), capabilities for variable horizontal refinement, and coupling to a state-of-the-art Earth system model. The aim is to leverage flexibility in horizontal refinement to better resolve TPVs and comprehensive coupling to better represent physical interactions throughout the Earth system.

3.1 Model descriptions

3.1.1 CESM1(CAM5) summary

The so-called CESM1(CAM5) configuration of CESM (used for CMIP5) is summarized in Hurrell et al. (2013). With further details in the references for the constituting atmosphere, land, ocean, sea ice, river, and coupling components, aspects of the sea ice model are summarized below. Importantly for this work, CAM5 improves the overt grid-scale dependence of the previous version due to differences in configuration and parameterizations (Zarzycki et al. 2014; Zhao et al. 2016), benefiting the physical basis in variable resolution simulations.

Each grid cell in the sea ice domain contains an ice thickness distribution describing the fractional area within the cell covered by horizontally uniform columns of ice in prescribed thickness ranges. The basic problem of the sea ice model is to evolve the ice thickness distribution in time and space (Hunke and Lipscomb 2010). Algorithmically, the evolution is split into three steps: horizontal transport geographically from drift, transport in thickness

space from ridging and other mechanical processes, and transport in thickness space from thermodynamic growth and melting. The net energy flux to the sea ice decomposed into the contributions from the atmosphere to the sea ice/snow cover and ocean to the sea ice is formulated as Eq. 3.1

$$F_{net} = F_s + F_l + F_{L\downarrow} + F_{L\uparrow} + (1-\alpha)(1-i_0)F_{sw} + \rho_w c_w c_h u_* (T_w - T_f) \tag{3.1}$$

for sensible heat flux F_s, latent heat flux F_l, longwave flux F_L, downwelling shortwave flux at the surface F_{sw}, shortwave albedo α, fraction of absorbed shortwave flux that penetrates through the ice i_0, density of seawater ρ_w, specific heat of seawater c_w, heat transfer coefficient c_h, friction velocity u_*, sea surface temperature T_w, and freezing temperature T_f, with fluxes positive downwards by convention. Fluxes are balanced by changes in enthalpy, with growth or melt if required. The vertical salinity profile is prescribed and constant over time. Integrating through thickness in the vertical direction, the two-dimensional momentum equation is formulated as Eq. 3.2

$$m\frac{\partial u}{\partial t} = \nabla \cdot \sigma + \tau_a + \tau_w - \hat{k} \times mfu - mg\nabla H_0 \tag{3.2}$$

for the combined mass of ice and snow per unit area m, horizontal velocity u, time t, internal stress tensor σ, wind stress τ_a, ocean stress τ_w, unit vertical $\hat{k}$, Coriolis frequency f, gravitational acceleration g, and sea surface slope H_0.

3.1.2 CESM-CAM-MPAS summary

3.1.2.1 Implementations of $v1.4.\beta07$ and $v2.0.\beta05$

MPAS is designed for the rapid prototyping of dynamical cores leveraging the horizontal discretization described in Thuburn et al. (2009) and Ringler et al. (2010) on variable-resolution spherical centroidal Voronoi tessellations discussed in Ju et al. (2011). Here, rather than the default finite-volume dynamical core (Lin 2004), CESM-CAM-MPAS $v1.4.\beta07$ uses MPAS-A v2.1 as the dynamical core within Community Atmosphere Model (CAM)

5.3, with interfaces to convert between state variables for each. For CESM-CAM-MPAS v2.0.β05, MPAS-A is updated to v4.0. Physics and dynamics are split, with physics parameterizations called every 30 minutes and tendencies applied constantly over the interval. Dynamics timesteps are a function of the minimum spacing in the grid (typically $4\Delta x$ to $6\Delta x$), e.g., for 25 km grid spacing, a 100 s timestep. Vertical spacing mimics the CAM default with 30 levels to the model top at 44.6 km. The so-called CESM1(CAM5) configuration (Hurrell et al. 2013) is used for the other components. At nominal 1° horizontal grid spacing, the non-atmospheric components and scales intentionally match those used in the CESM Large Ensemble (CESM-LE) (Kay et al. 2015), which is used additionally as a reference for model variability. Components are coupled to the atmosphere over 1800 s, 1800 s, 10800 s, and 86400 s intervals for the land, sea ice, river runoff, and ocean, respectively, with fluxes between the atmosphere and ocean computed on the atmospheric grid.

Verification ("solving the equations right") and validation ("solving the right equations") provide evidence for the correctness or accuracy of computational results (Oberkampf and Roy 2010). From animations of global maps from summer simulations (e.g., Sect. 3.3.3), variables output as in the CESM-LE in the atmosphere, land, ocean, sea ice, and river components, integrations follow expected geographic, diurnal, and subseasonal patterns (not shown). Tropopause and near-surface fields match existing standalone MPAS-A simulations through one week (see animation in Szapiro et al. (2017), slide 27). Sea ice motion is consistent in direction and magnitude with (artificially enhanced) atmospheric winds (e.g., Sect. 3.3.2). All of the above are consistent with a successful implementation coupling the atmospheric dynamical core within CAM and to the other components through the central coupler (Craig et al. 2012). Successful use of similar versions (e.g., Zhao et al. (2016)) further verifies the implementation.

3.2 Atmospheric resolution and consistency across scales, latitudes, and vertical levels

Horizontal refinement within the global MPAS mesh permits increased local resolution for features and processes and integration with a coarser domain using less cells than required for a global high-resolution simulation. Previous work substantiates the effectiveness of the approach. In quasi-uniform simulations with MPAS-A, spectra of kinetic energy possess the expected canonical structure in the troposphere and stratosphere using Δx =3- to 15-km grid spacings until filtered beneath an effective model resolution of approximately $6\Delta x$ (Skamarock et al. 2014). Qualitatively, fine-mesh regions have some finer-scale structure, and coarse-mesh regions are less well resolved (Skamarock et al. 2012). Smooth transitions in mesh refinement can eliminate the prominent wave distortions that occur in sharply nested meshes from mismatches in the boundary-update frequency and scales (Park et al. 2014). Since grid convergence does not necessarily occur in physical simulations (Bryan et al. 2003), it is difficult to justify sufficient resolution or explicitly balance resolution, cost, and error. From case study mesh sensitivity experiments (Sect. 2.3.3.1), it is believed that 30-km spacing in the Arctic is sufficient to resolve broad structures in surface and near-tropopause cyclones, without the scale-aware convective parameterizations needed at an order of magnitude smaller scale (e.g., Grell et al. (2014)).

3.3 Consistency and realism of simulated sea ice

Development and testing of CESM-CAM-MPAS as an Earth system model to the breadth and depth invested in CESM1(CAM5) is not feasible for all countries (Bentsen et al. 2013) and certainly not for this thesis. With matching non-atmospheric components and atmospheric physics, CESM-CAM-MPAS would be expected to inherit characteristics of CESM1(CAM5) (Sect. 3.3.1). In addition to the computational verification (Sect. 3.1.2.1),

additional experiments are necessary to evaluate CESM-CAM-MPAS in its own right, albeit necessarily limited in scope. Given the central focus here of sensitivity of Arctic sea ice to atmospheric forcing, two critical aspects are the (1) consistency of the sea ice response with the atmospheric forcing and (2) realism of the simulated ice cover. A case study with perturbed atmospheric resolution is used to test the former (Sect. 3.3.2). Hindcasts and forecasts are used to test the latter (Sect. 3.3.3).

3.3.1 Variability in CESM-LE SIE

If relatively coarse GCMs significantly damp important features and processes (e.g., Sect. 2.3.3.1), we hypothesize that the resulting simulated variability reflects systematic model filters. Here, aspects of the variability resulting from a benchmark climate model configuration closely related to that of CESM-CAM-MPAS are documented. Arctic SIE in the CESM1(CAM5) model also used for the CESM-LE exhibits a realistic annual cycle (Hurrell et al. (2013), Fig. 5; 365-d power in Fig. 3.1). For year-to-year 1979 to 2014 SIE anomalies, member deviations from the ensemble mean March minus September SIE and summer 500 hPa geopotential heights averaged north of 75°N are positively correlated ($p < .001$). This correlation derived from observations of SIE (from Fetterer et al. (2017)) and atmospheric upper-level heights (from Dee et al. (2011)) and in CESM-LE is stronger among years with larger absolute anomalies of sea ice change, with correlations of 0.57 (0.40) for all years in observations (CESM-LE), 0.69 (0.55) in years with absolute SIE change anomalies greater than 0.3M km^2, and 0.84 (0.66) in years with absolute SIE change anomalies greater than 0.6M km^2. That is, observed and modelled year-to-year differences in sea ice loss are consistent with cyclonic (anticyclonic) anomalies in the summer polar tropospheric circulation associated with less (more) sea ice loss. However, there is significantly less power in spectrally-decomposed CESM-LE SIE for periods less than 2 to 3 weeks (Fig. 3.1), concurrent with forcing from synoptic and smaller atmospheric scales (and lack of resolution below 1° for the sea ice and ocean models as well).

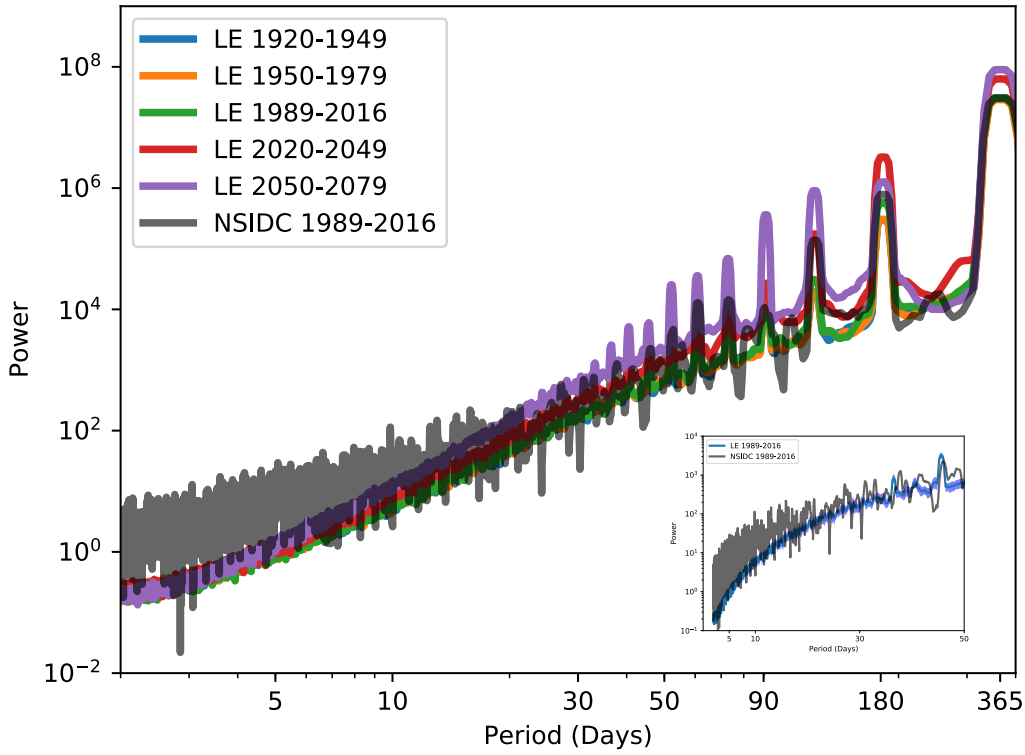

Figure 3.1: *Comparison of daily SIE Fourier-based power spectral density (10^{12} km^4 Hz^{-1}) 1989 to 2016 (gray; Fetterer et al. (2017)) and various CESM-LE year-intervals (colors) for periods less than 400 days. Finite time series have been tapered with a Blackman window (Blackman and Tukey 1958), and power has been smoothed by a 5-point mean. Axes are log-scale. Inset is for 1989 to 2016 with a 99% confidence interval on the CESM-LE mean from bootstrap resampling the mean of the members' powers 1000 times with replacement, plotted linearly in period through 50 days.*

If CESM-CAM-MPAS shares these characteristics, benefiting this work are well-representing the annual cycle of SIE and connections of year-to-year sea ice loss with the anomalies in the polar circulation in summer. Systematic filtering of higher frequency SIE limits its universal utility, reminding of the aphorism that "all models are wrong, but some are useful" (Box 1979). A concern is that systematically filtered higher-frequencies may limit mechanisms contributing to larger-scale sea ice variability (e.g., Roberts et al. (2015)).

3.3.2 Sensitivities of sea ice to atmospheric mesh refinement

To explore if the mesh-sensitivities of the atmospheric component propagate to other components when coupled, CESM-CAM-MPAS is used with the quasi-uniform 60 km and Arctic-refined meshes described previously. With prescribed differences in atmospheric resolution and corresponding dynamics timesteps, 10-d simulations are initialized on 00 UTC 15 August 2006 from ERA-Interim for the atmosphere and an existing restart of CESM-LE member 20 on 31 July 2011 for the other components, here mainly for spun-up and consistent sea ice and ocean states.

Similar to Skamarock et al. (2012), Fig. 12, atmospheric refinement increases resolution of finer-scales and variable intensities of local features (Fig. 3.2.a,b). In particular, vorticity filaments in the refined areas are sharper and more intense (e.g., near the pole and Atlantic coast of the United States). Coupled to the sea ice (Fig. 3.2.c,d), the synoptic-scale sea ice drift is similar, and differences in the local ice velocity are possible from differences in the local structure of the forcing. For example, eccentricity in sea ice motion near 85 °N, 40 °E appears associated with differences between the two simulations in position and timing of a front within the surface cyclone. Note that the above confirms that it is possible to mix separate operational and climate sources of initial conditions and interpret the results physically.

3.3.3 September sea ice outlook

With CESM-CAM-MPAS as a process-based, multi-component, global, and variable-resolution atmosphere model of the Earth system by design, its practical value depends on the resulting simulations being realistic and useful. With Arctic sea ice loss "faster than forecast" (Stroeve et al. 2007) and an unexpected record minimum in 2007, summer loss and September sea ice extent (SIE) minima have emerged as focal points of the Sea Ice Prediction Network (SIPN). Here, submitted forecasts for the SIPN-organized September 2017 Sea Ice Outlook are used for comparative evaluation. Note that the "Sea Ice Outlook provides

an open process for those interested in Arctic sea ice to share predictions and ideas; the Outlook is not an operational forecast" (Stroeve et al. 2017).

3.3.3.1 Configuration and initial conditions

With a combination of initial conditions from multiple sources possible (e.g., Sect. 3.3.2), there are a number of options for initializing simulations. Two considerations are the accuracy (e.g., Anderson and Anderson (1999)) of the initial conditions with respect to nature ("realism") and strong adjustments (e.g., Cosgrove et al. (2003)) early in model integrations ("consistency"). More realistic initial conditions are closer to the historical state. Greater consistency within and between model components involves a shorter spin-up and more physical process-based rates earlier in the simulation. Initializing from external analyses involves adjustment time, likely prohibitively long for oceanic process rates in particular (e.g., Zhang et al. (2007)). An experimental ocean data assimilation system with coupled sea ice (similar to Karspeck et al. (2013)) yielded grossly little sea ice cover, similarly sparse to free-running states from using the same atmospheric forcing of Large and Yeager (2009) (not shown). Even if willing to sacrifice consistency, attempts to correct the sea ice cover by prescribing an external analysis (Zhang and Rothrock 2003) were ineffective, since uncorrected warm upper-ocean temperatures rapidly melt the ice away (not shown).

If any CESM-LE simulations match historical conditions, they would be natural candidates to initialize hindcasts, forecasts, and experiments. Thus, the utility of cold-starting the higher-frequency atmosphere by interpolating external operational analysis for initial conditions and using analog initial conditions from CESM-LE for the other components with longer spin-up was explored. Formally, two states A and B are analogs if their distance is small, $d(A,B) < \varepsilon$, requiring a distance metric d and a tolerance ε. Practically, for a large, under-sampled state space, "there are numerous mediocre analogues but no truly good ones" (Lorenz 1969a). Extrapolating linear and quadratic trends to historical September pan-Arctic SIE 1979 to 2016, a SIE of approximately 4.1 to 4.6 M km^2 would

be expected for September 2017. CESM-LE members cross 4.5 M km^2 between the years of 2012 and 2033. With existing restarts available every 5 years starting in 2006 for the Representative Concentration Pathways 8.5 scenario (Meinshausen et al. 2011), 2021 in the middle of the overlapping period is selected as the CESM-LE simulation year corresponding to a historical 2017. While selecting ensemble members close to the expected SIE is possible, a larger problem is that restarts are not bit identical when using the same model states and CESM-LE code tag but with different compilers and libraries. For example, SIE in restarted member 5 initialized on 1 January 2021 differs from the original by over 2 M km^2 by September 2021. Such differences mute the utility of searching for analogs precisely. A future (strongly-)coupled data assimilation system could improve realism by adjusting model states towards observations and consistency and balance within and among the components (Mulholland et al. 2015).

Limited by storage and compute constraints, an 11 member initial condition ensemble constituted the July and August outlooks for September 2017. A larger ensemble size would be expected to increase forecast skill, particularly important for scenarios with lower inherent predictability (Kumar and Chen 2015) like expected in years with larger anomalies in September SIE (Hamilton and Stroeve 2016). The control member was initialized from GFS analysis for the atmosphere and a restart from member 20 of CESM-LE for the other components. A perturbed atmosphere (using ensemble GFS members 1 to 5) and perturbed non-atmospheric components (CESM-LE members 5 to 9) completed the ensemble. For the first June forecast, only 2 CESM-LE restarts formed the preliminary ensemble. Table 3.1 summarizes the outlook configurations. External forcings (including ozone) were prescribed and common in all members as in CESM-LE (Kay et al. 2015). Restart files for the sea ice component were converted from the CESM-LE version.

Outlook	Atmo ICs	Non-atmo ICs
June	GFS. 00Z 31 May 2017	CESM-LE 5, 20. 00Z 31 May 2021
July, control	GFS. 00Z 30 June 2017	CESM-LE 20. 00Z 30 June 2021
July, Δatmo	GEFS 1-5. 00Z 30 June 2017	CESM-LE 20. 00Z 30 June 2021
July, Δnon-atmo	GFS. 00Z 30 June 2017	CESM-LE 5-9. 00Z 30 June 2021
August, control	GFS. 00Z 31 July 2017	CESM-LE 20. 00Z 31 July 2021
August, Δatmo	GEFS 1-5. 00Z 31 July 2017	CESM-LE 20. 00Z 31 July 2021
August, Δnon-atmo	GFS. 00Z 31 July 2017	CESM-LE 5-9. 00Z 31 July 2021

Table 3.1: *Summary of simulations used in the submitted CESM-CAM-MPAS (2) June, (11) July, and (11) August 2017 Sea Ice Outlooks, with name, atmospheric (atmo) initial conditions (ICs), and ICs for the non-atmospheric models for the sea ice, ocean, land, and river components. Simulations are integrated as if in 2021 through September 2021.*

3.3.3.2 Sea ice outlook forecasts

Each ensemble member's SIE is calculated directly from the September time-mean sea ice concentration, with a 15% threshold for extent. The submitted forecast is the ensemble mean with the ensemble standard deviation as a measure of uncertainty.

Mean forecast errors for September 2017 for the Arctic decrease with shorter forecasts (Fig. 3.3). With standard deviations of 0.5 and 0.6 M km^2 for July and August CESM-CAM-MPAS outlooks, respectively, the observed SIE falls within one standard deviation of the forecast means. While the southern hemisphere is not a focus of this work, it is included in the global simulations. The Antarctic outlook falls within the closest apparent group for all 3 months (Fig. 3.3), lending evidence to the generality of the approach.

Additional experiments in summer 2006, 2007, and 2012 have also been conducted (Table 3.2). Differences between 4-week simulations with atmosphere initialized on 00 UTC 15 August 2006 versus 2007 capture all six of the main low and high tropopause potential temperature regions north of the polar jet (Fig. 3.4), qualitatively better spatially than in intensity. The similarities are perhaps particularly notable since initial conditions for the non-atmospheric components (e.g., sea surface temperatures) are from a free-running climate simulation. For the 2012 case, the simulated early August "Great Arctic cyclone"

Case	Atmo ICs	Non-atmo ICs	End date
2006	ERA-I. 00Z 15 August 2006	CESM-LE 20. 00Z 14 August 2006	12 September 2006
2007	ERA-I. 00Z 15 August 2007	CESM-LE 20. 00Z 14 August 2006	12 September 2006
2012	ERA-I. 00Z 01 August 2012	CESM-LE 20. 00Z 31 July 2011	01 October 2012

Table 3.2: *Summary of additional CESM-CAM-MPAS "hindcast" simulations in summer 2006, 2007, and 2012, with case, atmospheric initial conditions (atmo ICs), non-atmospheric ICs, and end date. The 4-week, 4-week, and 2-month simulations start on the day of the atmospheric initial condition in the year of the end date.*

(Simmonds and Rudeva 2012) reached minimum mean sea level pressure of 964 hPa and drove maximum 6-h mean sea ice velocity of 64 cm s^{-1}. The September mean SIE of 4.35 M km^2 is closer to the observed 3.57 M km^2 than the 5.64 M km^2 of the CESM-LE member used as the restart analog.

3.3.3.3 Spatial probability score of sea ice edge

Pan-Arctic SIE does not consider the spatial distribution of the ice cover. Developed to further forecast verification of the sea ice edge, the spatial probability score (SPS) for contours (Goessling and Jung 2018) combines probabilistic and spatial forecast verification. To evaluate the error and skill in the 15% contour in sea ice concentration (SIC) geographically in aggregate (Eqn. 3.3),

$$SPS = \int_A (P_f(SIC \geq 15\%) - P_o(SIC \geq 15\%))^2 dA \tag{3.3}$$

for forecast P_f and observed P_o probability, respectively. For observed SIC, the MASAM2 daily 4-km product is used (Fetterer et al. 2015). The P_f from the coarser, daily-mean simulated SIC is calculated directly from the 11-member ensemble and then nearest-neighbor regridded (to match the model state's definition) to the fine observational grid (where the reference truth for the sea ice edge exists). Note that this creates more sensitivity to the

observational product used (Zampieri et al. 2018), which may be treated more comprehensively by combining multiple observation products for a non-binary P_o. On the fine calculation grid, only cells where the simulated and observed SIC are both valid are included in the area integral (e.g., not over model land or the observation polar hole).

Daily SPS for the August outlook is shown in Fig. 3.5. Non-conventionally, the forecast error for the sea ice edge decreases with lead time. In contrast, calculated SPS for the restarted CESM-LE member 020 is larger than 1.2 M km^2 for June through September. While the atmospheric dynamical cores are also different, the initialization strategy likely explains the increasing skill. SPS decreases most rapidly in the first week as the sea ice and ocean from free-running CESM-LE states adjust with the atmosphere initialized from operational analysis, which includes assimilated observations. Skillful SPS can be determined in comparison to operational models and reference benchmarks (Zampieri et al. 2018). CESM-CAM-MPAS SPS for one ensemble forecast is generally lower than the 32 days and longer lead times of the 1999 to 2010 means and climatological benchmark (Zampieri et al. (2018), Fig. 2) by mid-September. However, the emergent skill neither falls outside the benchmark's confidence interval nor is less than the annual mean threshold of 0.55 M km^2.

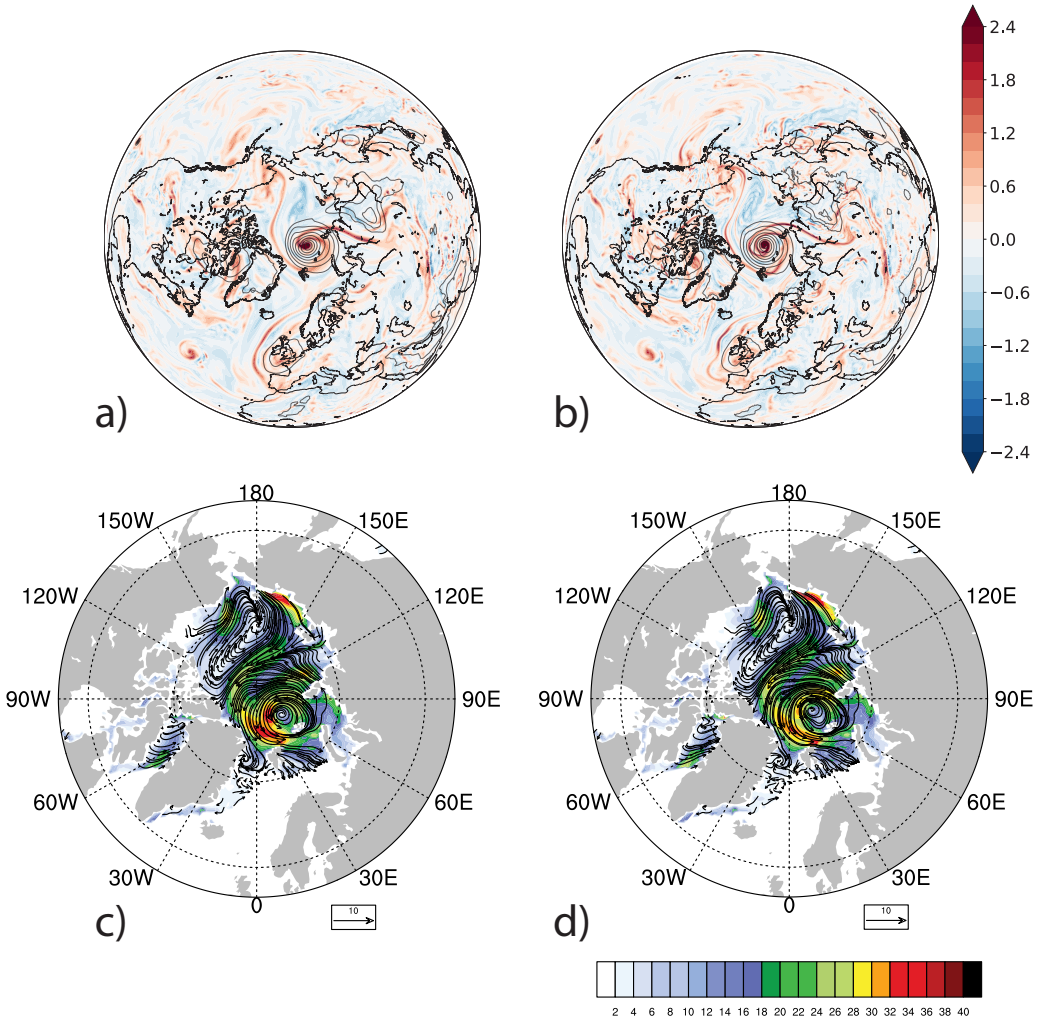

Figure 3.2: *06 UTC 18 August 2006 CESM-CAM-MPAS (a,b) 500 hPa relative vertical vorticity ($2(10)^{-5}$ s^{-1} interval) with mean sea level pressure $\leq$ 1004 hPa (gray contours; 4 hPa interval) for (a) quasi-uniform 60-km mesh and (b) Arctic-refined ~25 to 90 km mesh with the same number of cells. (c,d) 6-hourly mean ice velocity (2 cm s^{-1} interval) for (c) quasi-uniform 60-km and (d) Arctic-refined meshes, respectively.*

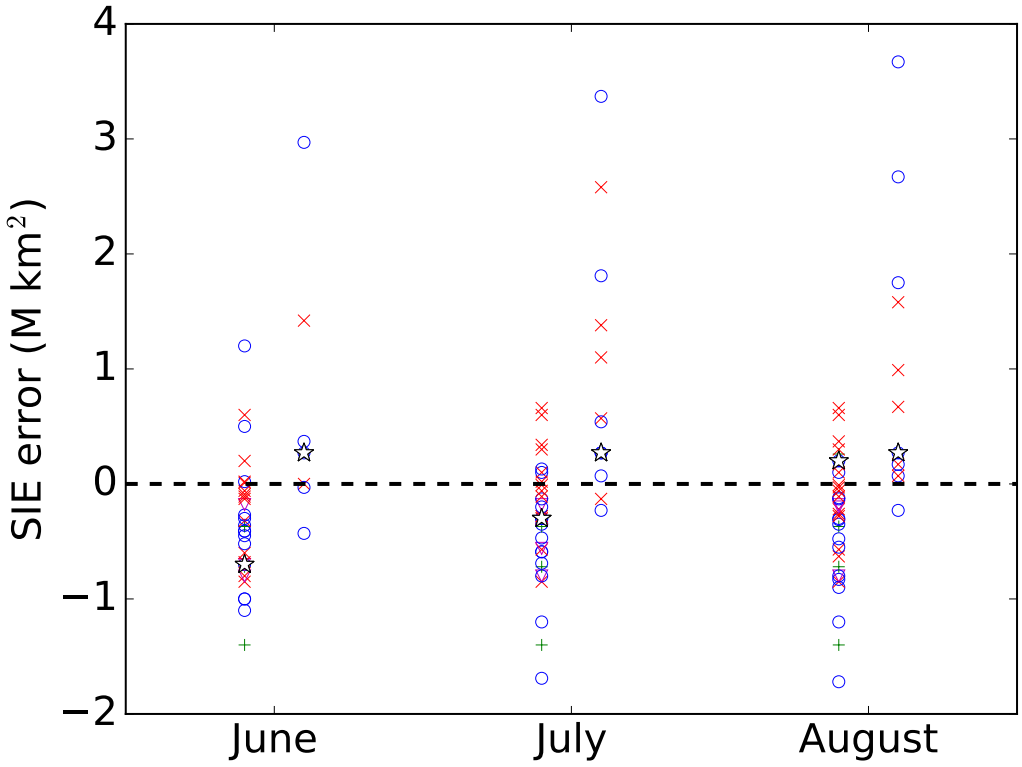

Figure 3.3: *Errors in June, July, and August 2017 Sea Ice Outlooks for September mean (left) Arctic and (right) Antarctic sea ice extent. Submissions are grouped by method with dynamical (blue circle), statistical (red cross), mixed (magenta triangle), and heuristic (green plus) models. Additionally, CESM-CAM-MPAS is starred. Observed September 2017 mean SIE (Fetterer et al. 2017) was 4.8 M km^2 for the Arctic and 17.83 M km^2 for the Antarctic.*

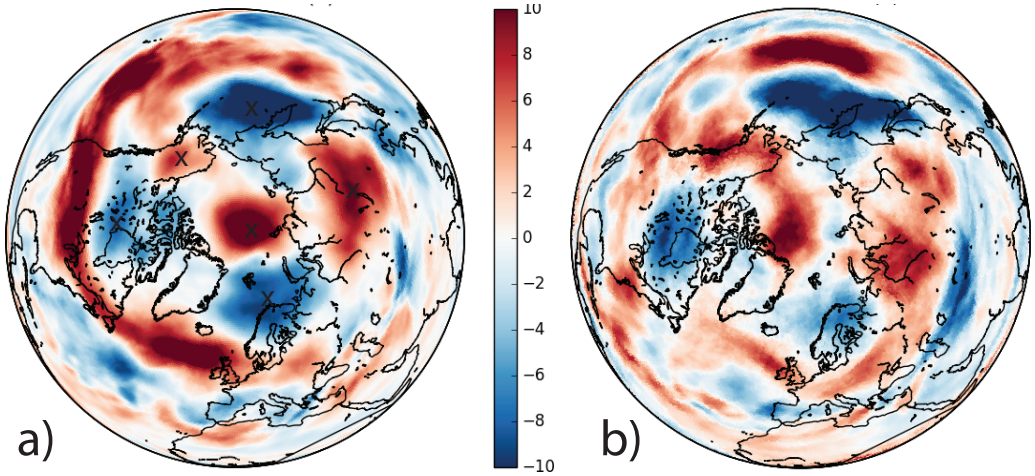

Figure 3.4: *Mean 15 August to 12 September 2007 minus 2006 difference tropopause potential temperature (K) from (a) ERA-Interim and (b) MPAS-CESM simulations. 6 coherent polar anomalies in (a) are marked with 'x'.*

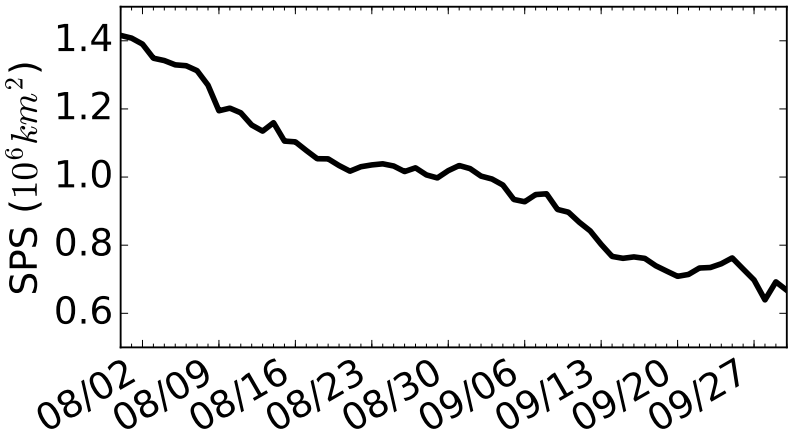

Figure 3.5: *Spatial probability score for August 2017 CESM-CAM-MPAS Sea Ice Outlook of Arctic 15% sea ice concentration.*

3.4 Computational efficiency

From the August 2017 SIO ensemble run on the Yellowstone supercomputer (CISL 2016) with 32×16 processors for each member, compute cost can be estimated for CESM-CAM-MPAS using the Arctic-refined atmospheric mesh with full history output as in CESM-LE with additional MPAS history output. Without further software or processor layout optimization, integration costs 1546 ± 4 compute hours per simulated month (mean and standard deviation, $n = 11$). The SIO simulations were limited by 30000 compute hours per calendar month shared among several development projects. Note that more resources allow for higher resolution, increased complexity, more ensemble members, or more cases.

3.5 Discussion

To test and quantify the impacts of TPVs on Arctic sea ice variability and associated mechanisms, we propose causal TPV-based sensitivity experiments using an Arctic-refined configuration of CESM-CAM-MPAS with mixed historical and analog initial conditions. The rationale is as follows. By construction, CESM-CAM-MPAS is dynamically consistent across components, latitudes, vertical levels, and resolved scales, with process-based exchanges of information between all. Model resolution is a systematic filter on the intensities of model state variables and process rates operating on those states. Variable atmospheric refinement permits efficiently increased local resolution, yielding finer structures with more variable intensities. Refinement in the Arctic permits improved resolution of (the intensities of) local interactions between TPVs, surface cyclones, and sea ice. A global domain provides consistency with the flow outside the Arctic, particularly important for sensitivity experiments possibly modifying the planetary circulation. Mixed historical and analog initial conditions offer flexibility in the flow conditions for causal sensitivity experiments and reduce spin-up times of simulations. Successful forecasts lend credibility to the realism and implications of model experiments. Using a mesh refined in the Arctic, June,

July, and August sea ice outlooks for September 2017 are competitive with the other submissions. Non-conventionally, forecast error of the sea ice edge decreases with lead time with emergent skill, likely driven by the combined historical and analog initialization strategy. Tendency-based TPV modifications are effective at dynamically modifying TPVs with changes in TPV intensity consistent with an added heating rate and directly localized to the TPV by construction.

Additional hindcasts (with perturbed configurations) would further inform the utility and trade-offs of the model design. Sensitivities to resolutions in the non-atmospheric components have not been explored. Of potential interest would be the future of high-frequency sea ice variability, which are similar across time in CESM-LE (Fig. 3.1).

The method of using analog initial conditions is powerful, as it strongly reduces model spin-up time particularly for components with slow adjustment processes. However, differences in the computing environment can cause a restarted simulation not to be bit-reproducible and therefore not necessarily on the trajectory that is expected from the native run. Additional layers of technology (Howe 2012; Jimenez et al. 2015) may offer solutions to address this limitation for future experiments. However, we continue with the legacy of past experiments.

Consistent, coupled processes and sufficient resolution that is computationally efficient permit a wide range of simulations. The impacts of TPV intensity errors on Arctic sea ice variability are a focus of Ch. 4. Moreover, a similar framework could be used to test and further refine connections between TPVs and other features or processes (like mean circulation (Shapiro et al. 1987) or chemical transport (Sprenger et al. 2007)). Direct modifications of other features or processes with coupled, integrated responses throughout the modelled Earth system are similarly possible. Sensitivity experiments conducted with any single model raise concerns over the generality of any results. Constructive combination with statistical, regional, or reduced complexity models are essential for evaluation of inter-model significance.

Chapter 4

Evaluation of impacts of TPVs on Arctic sea ice

To evaluate to what degree and through what mechanisms can TPVs impact variability of Arctic sea ice loss, CESM-CAM-MPAS is used to conduct sensitivity experiments with directly modified TPV intensity. The resulting sensitivities of sea ice to the modifications are quantified and contextualized with respect to reference distributions. Differences in model states and sea ice budgets are used to diagnose the associated mechanisms.

4.1 Causal TPV modification experiments

Table 4.1 summarizes the set of experiments sampling model sensitivities to directly modified TPV intensity. A restart of CESM-LE member 001 initialized on 00 UTC 01 January 2006 is used to branch the other simulations. Non-atmospheric initial conditions for the CESM-CAM-MPAS control and TPV-modification experiments are from the CESM-LE restart on 00 UTC 01 July 2006. Initial near-surface temperatures (Fig. 4.1) and sea ice cover (Fig. 4.2) are reasonable for historical conditions in early July, with hemispheric, latitudinal, land versus sea, and elevation temperature gradients. Sea ice is present throughout much of the Arctic Ocean and thickest near the Canadian Arctic Archipelago and northern Greenland. Atmospheric initial conditions are interpolated from ERA-Interim, from 00 UTC 01 July 2007 to prescribe a realistic initial atmosphere. SIEs are similar between the CESM-LE restart and control simulations (e.g., Table 4.1).

To define TPVs during the model integration, first, a reference dynamic tropopause is defined simply by latitude ϕ, increasing from the pole: $\bar{\theta}_{DT}(\phi) = 310\ K + 0.5(90^\circ - \phi)$. Then, the horizontal extents of TPVs are defined via deviations from the reference tropopause within prescribed geographic regions. Note that the reference tropopause approximates the mean polar tropopause of the control simulation from which it was derived

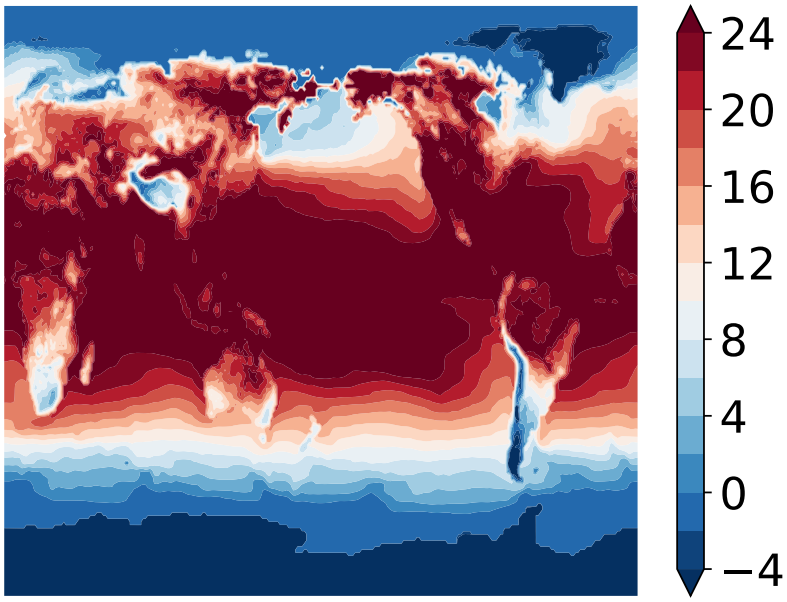

Figure 4.1: *Initial land and sea surface temperatures (°C; 2 °C interval) averaged over the first day of experiment L.P.-10.*

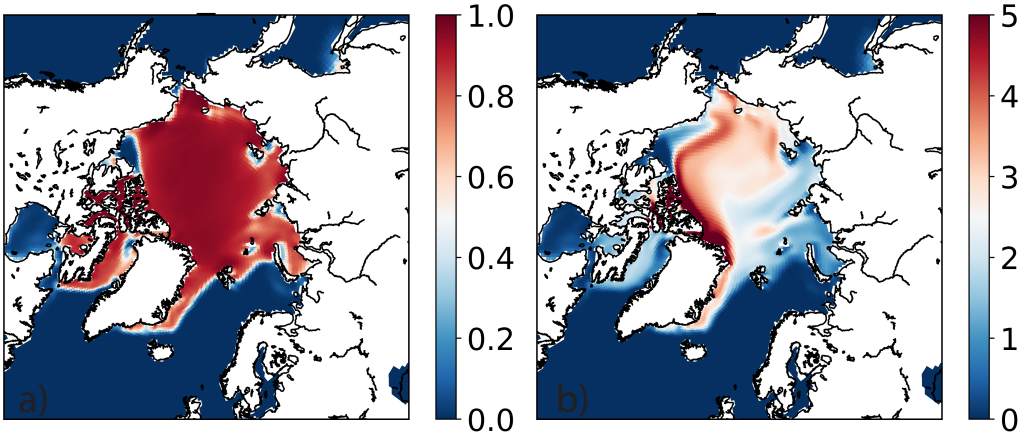

Figure 4.2: *Initial Arctic sea ice (a) concentration (%) and (b) thickness (m) averaged over the first day of experiment L.P.-10.*

(root-mean-square difference to the time-mean, latitude-mean of 0.3 K in $[50, 90]$ °N). In the vertical, tendencies are applied in a thin layer beneath the tropopause: $\theta \in [\theta_{DT} - 10\ K, \theta_{DT})$. Fig. 4.3 illustrates that TPVs after 9 d subject to direct TPV modifications correspond well to the imposed modifications (e.g., strengthening cyclonic TPVs outside of the Arctic generates stronger cyclonic TPVs outside the Arctic (Fig. 4.3.e)). In turn, the atmospheric circulation and weather-of-the-day differ as well. The simplicity of the prescribed TPV definitions and modifications facilitates implementation of comparable, effective modifications across a range of models. Available compute hours, wall-clock hours, and file storage resources particularly constrain the number of experiments.

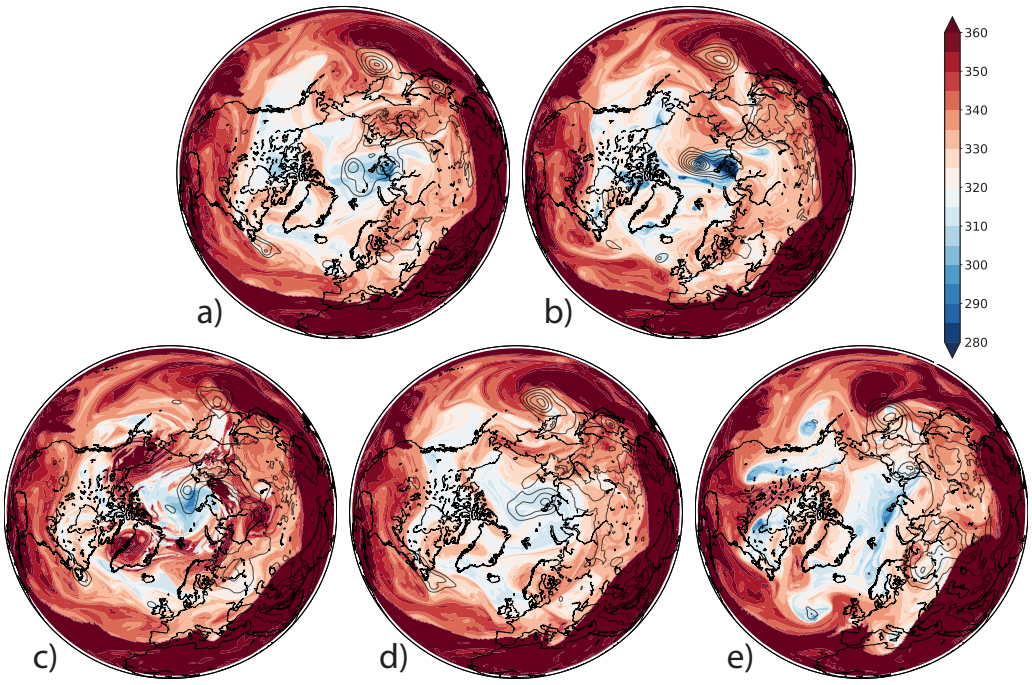

Figure 4.3: *00 UTC 10 July 2006 tropopause potential temperature (K, colors in 5 K intervals) and mean sea level pressure $\leq$ 1004 hPa (hPa, contours in 4 hPa intervals) in TPV modification experiments for (a) control, (b) stronger cyclonic TPVs in the Arctic (L.P.-10), (c) stronger anticyclonic TPVs in the Arctic (H.P.10), (d) weaker cyclonic TPVs in the Arctic (L.P.+10), and (e) stronger cyclonic TPVs outside the Arctic (L.M.-10).*

Time series of simulated SIE (Fig. 4.4) show the July to September melt. Initialized identically, little variability over the first week grows over time to a range of approximately 1 M km^2 by mid-August and 2 M km^2 by the end of September. Sect. 4.1.1 contextualizes the scales of the generated variability in terms of significance.

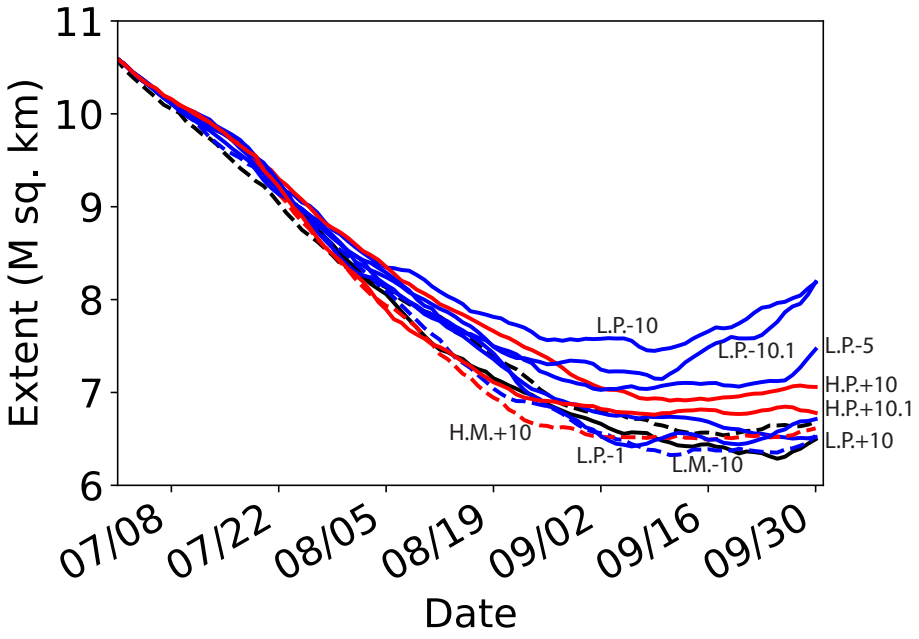

Figure 4.4: *Time series of daily-mean pan-Arctic SIE in TPV intensity modification experiments from 01 July to 01 October 2006. With respect to the (solid black) control and (dashed black) CESM-LE restart, experiments are labelled as in Table 4.1 and coded (blue-lows, red-highs, solid-polar, and dashed-mid-latitude).*

4.1.1 Reference measures of sea ice variability

To interpret sensitivity experiments, it is important to determine whether any resulting differences are significantly large or physically meaningful. The following simple example introduces the method taken here. Consider three rolls from a gambler with a six-sided dice: 1, 2, then 1. For uniform probability faces, the odds that three independent rolls are all no greater than 2 are $\frac{1}{3} \times \frac{1}{3} \times \frac{1}{3} \approx 0.037$. To, say a one-sided $p = 0.05$ level of

significance, analysis of the resulting rolls rejects a hypothesis that the dice is fair. Contextualizing independent samples with expected or reference distributions helps rationalize the extremeness or rarity of events. An analogous approach is taken to contextualize the sensitivity of sea ice in TPV modification experiments using the probability that samples occur within the tails of empirical reference distributions.

4.1.1.1 Observed satellite-era and CESM-LE September SIE

Two reference distributions are used to contextualize the sensitivity of sea ice to TPV perturbations (Fig. 4.5). One is derived from observational record as the year-to-year deviations from a least-squares quadratic-fit of September SIEs from 1979 through 2018. The other is derived from the intrinsic variability of a climate model as deviations of the ensemble member September SIEs from the ensemble mean in 2006. The range of each reference distribution is not small, exceeding 2 M km^2. Together, they are assumed to represent the variability of SIE exhibited under a multitude of drivers.

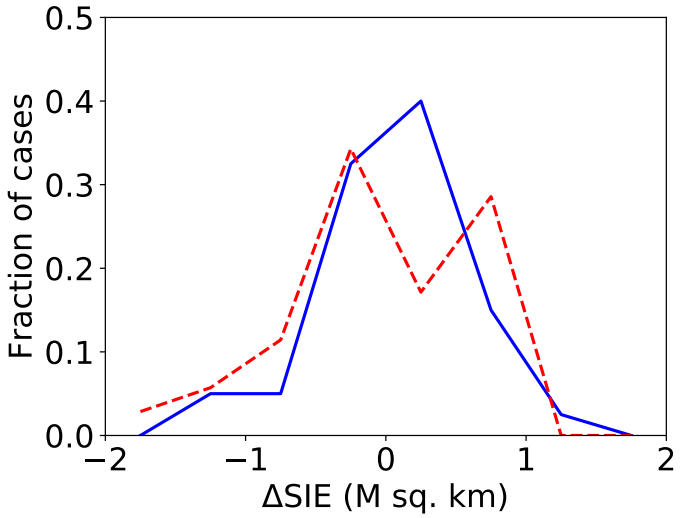

Figure 4.5: *Histograms of anomalous September sea ice extent, from observations (blue) and CESM-LE (red). Observed values are deviations from a quadratic fit of 1979 to 2018. CESM-LE values are deviations from the ensemble mean in 2006. Bins have 0.5 M sq. km equal spacing.*

September ΔSIEs in the two cases with strongly intensified Arctic cyclones (L.P.-10 and L.P.-10.1) are both larger than any observed or ensemble samples ($p = 0$). ΔSIE when intensifying by -5 K d^{-1} instead is larger than 39/40 observed ($p = 0.02$) and 5/35 ensemble samples ($p = 0.14$), a marginal case in terms of significance. Not significant are ΔSIE from strongly intensifying anticyclones in the Arctic ($p = 0.08$ and $p = 0.26$ relative to observations and CESM-LE) and the rest of the individual simulations that fall well within the reference distributions ($p > 0.2$). Further focus here is on the physical mechanisms by which strengthened cyclonic TPVs in the Arctic differentially increase September SIE. Note that the above does not show that the other categories cannot impact sea ice variability. Particularly if employing more simulations, $p^n < p_0$ is a helpful condition for estimating the number of independent samples n needed for a single experiment with significance p to reach a level of significance p_0, but the statistical power of the test decreases as more samples are needed.

Description	TPV modification – extent	TPV modification – tendency	September SIE (M sq. km)
Restart of CESM-LE member 001	None	None	6.68
Control	None	None	6.56
Intensify Arctic cyclones (L.P.-10.1)	$\theta_{DT} \leq \bar{\theta}_{DT} - 5$K. $\phi \geq 65$ °N	-10.1 K d^{-1}	7.99
Intensify Arctic cyclones (L.P.-10)	$\theta_{DT} \leq \bar{\theta}_{DT} - 5$K. $\phi \geq 65$ °N	-10 K d^{-1}	7.94
Intensify Arctic cyclones (moderate) (L.P.-5)	$\theta_{DT} \leq \bar{\theta}_{DT} - 5$K. $\phi \geq 65$ °N	-5 K d^{-1}	7.29
Intensify Arctic anticyclones (H.P.+10)	$\theta_{DT} \geq \bar{\theta}_{DT} + 5$K. $\phi \geq 65$ °N	+10 K d^{-1}	7.09
Intensify Arctic anticyclones (H.P.+10.1)	$\theta_{DT} \geq \bar{\theta}_{DT} + 5$K. $\phi \geq 65$ °N.	+10.1 K d^{-1}	7.07
Weaken Arctic cyclones (L.P.+10)	$\theta_{DT} \leq \bar{\theta}_{DT} - 5$K. $\phi \geq 65$ °N	+10 K d^{-1}	6.77
Intensify Arctic cyclones (weak) (L.P.+5)	$\theta_{DT} \leq \bar{\theta}_{DT} - 5$K. $\phi \geq 65$ °N	-1 K d^{-1}	6.67
Intensify extra-Arctic anticyclones (H.M.+10)	$\theta_{DT} \geq \bar{\theta}_{DT} + 5$K. $\phi \leq 60$ °N.	+10 K d^{-1}	6.59
Intensify extra-Arctic cyclones (L.M.-10)	$\theta \leq \bar{\theta}_{DT} - 5$K. $\phi \leq 60$ °N	-10 K d^{-1}	6.50

Table 4.1: *Summary of TPV intensity-modification experiments, listing a brief description, horizontal extent and tendency of TPV modification, and September sea ice extent calculated as area in the northern-hemisphere of time-mean sea ice concentration of at least 15%. CESM-CAM-MPAS simulations are configured with an Arctic-refined atmospheric mesh. Sensitivity experiments are sorted by SIE. Parenthesized short names in the descriptions stand for Lows/Highs.Polar/Midlatitude.Tendency.*

4.2 Impacts of cyclonic TPVs in the Arctic on mean sea ice state and associated linkages

Among the experiments above, strengthening cyclonic TPVs in the Arctic by $\lesssim -5$ K d^{-1} causes significantly less summer SIE loss. Decomposed differences in simulation-mean sea ice states and tendencies for mass, momentum, and energy (Figs. 4.6, 4.7, 4.8, and 4.9) reveal spatially coherent patterns for where, how, and why. Note that fluxes to the sea ice and ocean are distinct from energy exchanged only with the sea ice, which entangles the flux rates with area-weighting by sea ice concentration. While the latter are the ingredients of sea ice budgets, they tend to highlight differences in sea ice concentration rather than differences in the forcings (not shown), which are the focus here.

Focusing on experiment L.P.-10, stronger polar cyclonic TPVs increase concentration in the marginal areas, except for decreases in [30,90] °E (Fig. 4.6.a) and a broad, smaller magnitude area of reduced concentration in the central Arctic. Changes in sea ice thickness spatially correlate with changes in concentration but with more pronounced magnitudes in the central Arctic and north of Greenland (Fig. 4.6.b). Snow depth on sea ice is generally greater (Fig. 4.6.c).

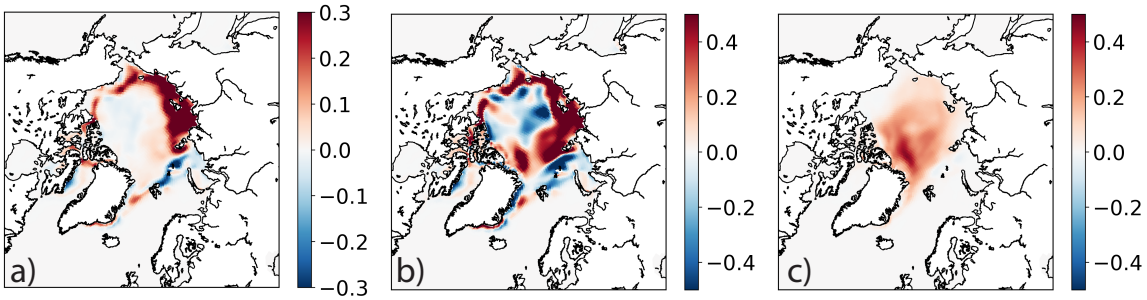

Figure 4.6: *Mean difference (July through September 2006) of intensified cyclonic TPVs in the Arctic (L.P.-10) minus control for (a) sea ice concentration (fraction), (b) sea ice thickness (m), and (c) snow depth on sea ice (m)*

Differences in thermodynamic tendencies generally increase sea ice concentration, except for the periphery of marginal areas and north of Severnaya Zemlya (Fig. 4.7.a). Differences in dynamic tendencies exhibit dipoles as well as broad loss of differential export throughout the central Arctic (Fig. 4.7.b). Increased thermodynamic loss near the margins may be a product of longer melting of more ice furnished by dynamics. Regions with

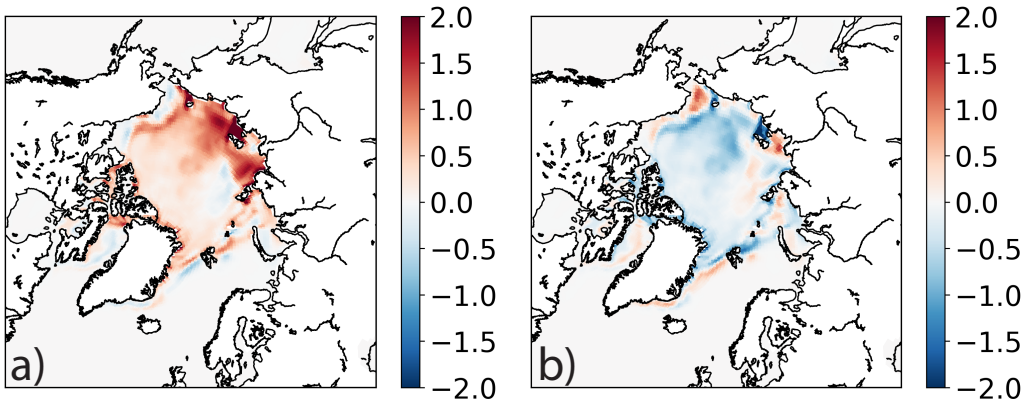

Figure 4.7: *Mean difference (July through September 2006) of intensified cyclonic TPVs in the Arctic (L.P.-10) minus control for sea ice concentration tendency (% d^{-1}) from (a) thermodynamic and (b) dynamic processes.*

differential dynamic SIC gain also have increased ice convergence (Fig. 4.8). Reduced drift from the East Siberian Sea and enhanced divergence with the mean cyclone match the reduced concentration in the central Arctic and enhanced outside.

Differences in the surface energy budget are dominated by oceanic, radiative, and lesser sensible and latent heat fluxes (Fig. 4.9). Reduced upward fluxes from the ocean to the ice, e.g., near the coastline of the eastern Arctic (Fig. 4.9.c), are consistent with strongly increased fluxes through thin ice (Maykut 1978). That is, maintained ice cover can maintain ice cover by limiting melting from ocean heat fluxes. Generally reduced downwelling longwave radiation (Fig. 4.9.d) corresponds to cooler columns (Fig. 4.11), while areas with less upwelling longwave radiation (Fig. 4.9.e) correspond to increased ice cover. Downwelling shortwave radiation (Fig. 4.9.f) generally is the dual of downwelling longwave radiation,

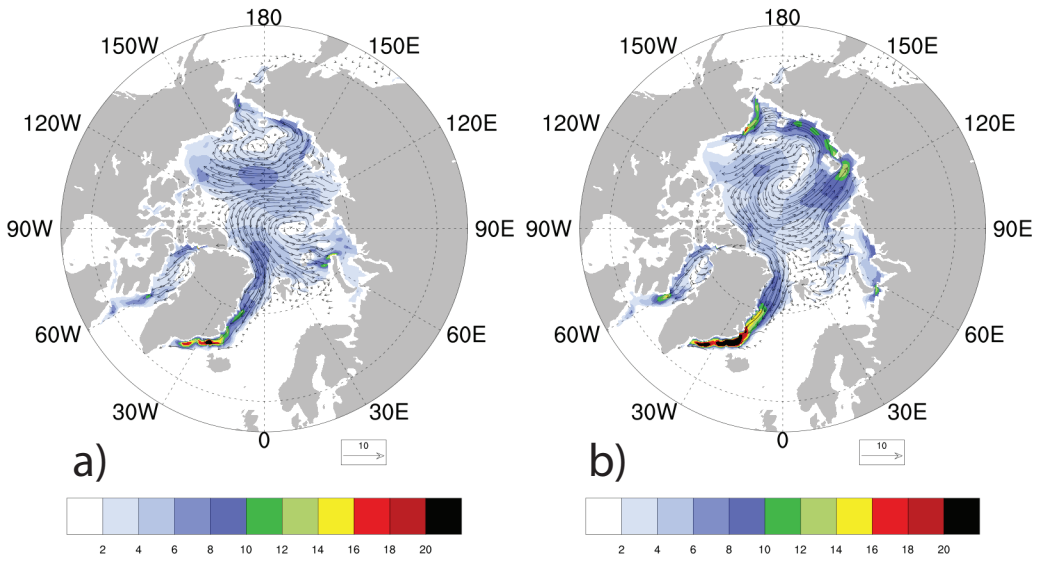

Figure 4.8: *Mean (July through September 2006) sea ice motion (cm s^{-1}) of (a) control and (b) intensified cyclonic TPVs in the Arctic (L.P.-10).*

suggesting competing effects of cloud cover. More directly important for the sea ice heat budget is that differences in downwelling shortwave radiation do not correspond to differences in absorbed shortwave radiation (Fig. 4.9.g), likely more driven by changes in surface optical properties of ice versus ocean.

Accumulated differences in the time-mean atmosphere correspond well. Over the Laptev Sea (Fig. 4.10) with increased SIC in L.P.-10, temperature is cooler from the surface through 350 hPa, the free troposphere is more stable, dewpoint depressions are similar, and winds are northwesterly versus southwesterly in L.P.-10 with respect to the control. Mean surface temperature below freezing and winds moving ice from the central Arctic both enhance local ice coverage. The local column is part of broader differences in the circulations, with mean surface and tropopause cyclones to the east and anticyclones to the west (Fig. 4.11). Table 4.2 shows sample Pearson correlation coefficients in the time-mean differences of L.P.-10 minus L.P.-1 among cells north of 70 °N. Note that while L.P.-1 is used as a reference since the CAM output files from control have been purged from the file

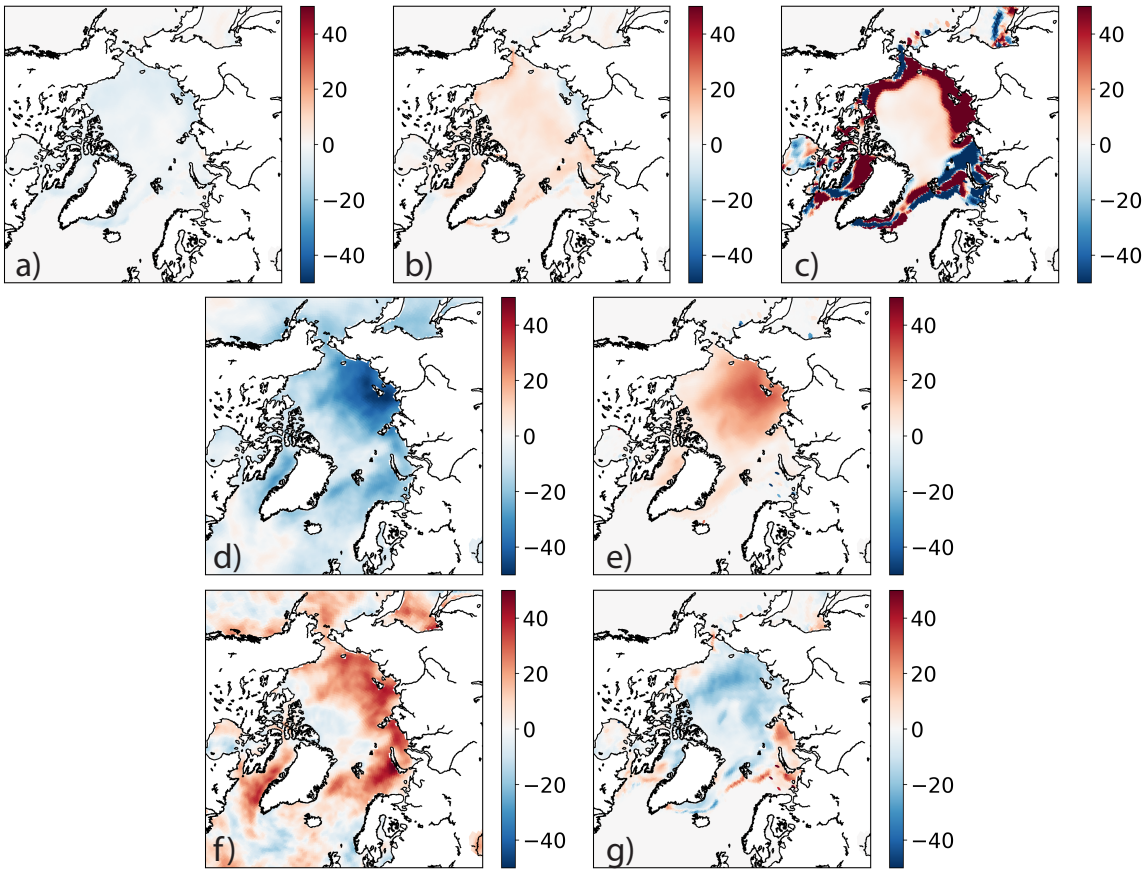

Figure 4.9: *Mean difference (July through September 2006) of intensified cyclonic TPVs in the Arctic (L.P.-10) minus control for components of the surface energy budget (W m^{-2}), (a) latent heat flux, (b) sensible heat flux, (c) ocean heat flux, (d) downwelling longwave radiation, (e) upwelling longwave radiation, (f) downwelling shortwave radiation, and (g) absorbed shortwave radiation. Directional fluxes are positive downwards by convention.*

system, L.P.-1 and control are spatially similar with respect to L.P.-10 in terms of differential sea ice loss and circulation (not shown). Especially given the coherent synoptic regions in the differential circulation, it is difficult to estimate an independent sample size from the 32241 polar cells and the significance of the correlations. There are differences outside the Arctic as well, including a prominent mean anticyclone over the north Pacific. Such extra-Arctic sensitivities are allowed to evolve in the global simulation, rather than prescribed in a regional Arctic LAM experiment. Driven by changes in TPV intensity, impacts on

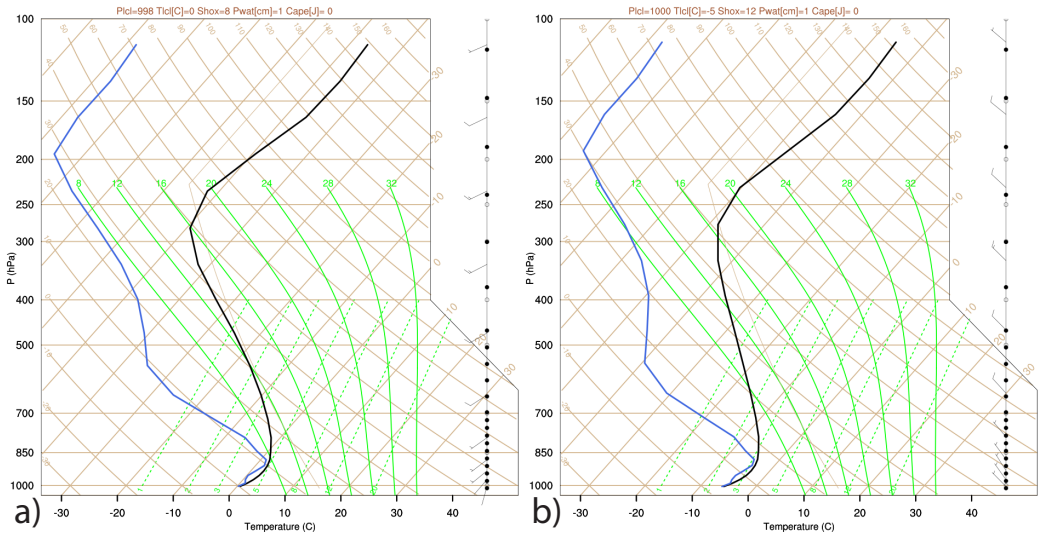

Figure 4.10: *Time-mean skew T - log p diagrams at 76 °N, 130 °E in the Laptev Sea for the (a) control and (b) L.P.-10 experiment. In September, the location is nearly ice-free in the control while ice-covered in L.P.-10.*

temperature, pressure, clouds, radiation, and sea ice propagate throughout the model state dynamically.

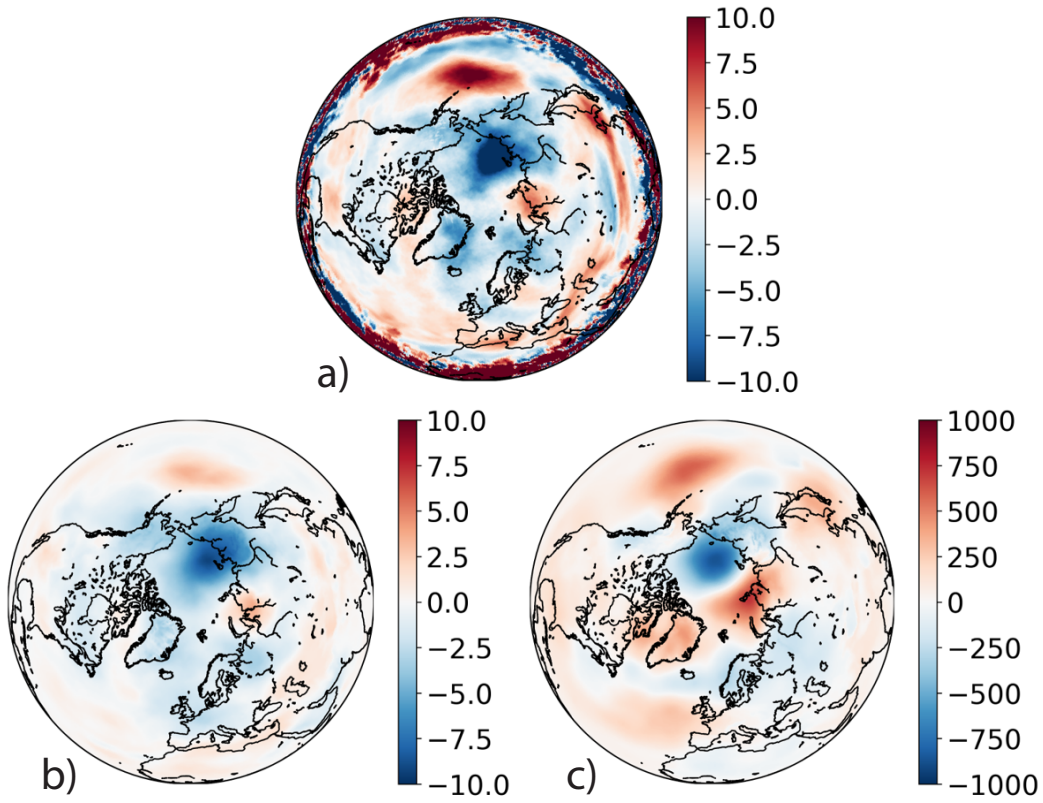

Figure 4.11: *Mean difference (July through September 2006) of intensified cyclonic TPVs in the Arctic (L.P.-10) minus control for (a) dynamic tropopause potential temperature (K), (b) 850 hPa temperature (K), and (c) mean sea level pressure (Pa).*

Name	CLDTOT	FLDS	FSDS	ICEFRAC	TGCLDIWP	TGCLDLWP	TREFHT
CLDTOT	1.0	0.6	-0.7	-0.2	0.1	0.5	0.1
FLDS	-	1.0	-0.8	-0.4	-0.1	0.8	0.7
FSDS	-	-	1.0	0.4	0.1	-0.9	-0.4
ICEFRAC	-	-	-	1.0	-0.2	-0.3	-0.4
TGCLDIWP	-	-	-	-	1.0	-0.3	-0.1
TGCLDLWP	-	-	-	-	-	1.0	0.4

Table 4.2: *Sample Pearson correlations of time-mean L.P.-10 minus L.P.-1 north of 70 °N among total cloud fraction, downwelling longwave radiation, downwelling shortwave radiation, fractional sea ice coverage, column ice water path, column liquid water path, and 2 m temperature. Names are as in CAM. Table is symmetric.*

4.3 Integrated perspective

Since large modifications (heating rates of ± 10 K d^{-1}) near the tropopause of cyclones outside the Arctic or anti-cyclones do not generate significant SIE sensitivities in individual simulations, cyclonic TPVs in the Arctic are considered separately. More intense cyclonic TPVs in the Arctic are capable of causing less sea ice loss by impacting the mass, momentum, and energy of Arctic sea ice. The artificial intensification sufficient to realize significant sensitivity in individual simulations for July through September 2006 is near -5 K d^{-1}. This is larger than composite mean diabatic heating rates within TPVs of O(1 K d^{-1}) (Cavallo and Hakim 2010). It is not beyond the range of errors in TPV intensification exhibited by operational forecasts (Sect. 2.3.1). Corresponding to a direct energy input of O(1 W m^{-2}) or less to the Earth system (Sect. 2.4.3), impacts can be evident within a season.

While formulation of the experiments throughout as deviations eliminates needing to know the CESM-CAM-MPAS model climate, the employed method to evaluate significance implicitly assumes that sea ice variability in CESM-CAM-MPAS is not considerably larger than the reference distributions. Reasonable CESM-CAM-MPAS sea ice forecasts, comparable reference distributions, and shared model components support the assumption.

The pathways and linkages through which TPV impacts operate deepen the results. Dynamically, TPVs can maintain SIE by differentially exporting sea ice from the central Arctic to the periphery. Thermodynamically, while sensitivities to TPVs can modify atmospheric pressure, wind, temperature, and clouds, couplings through changes in the sea ice state appear to dominate net surface heat fluxes. Maintained ice cover reduces upward ocean heat fluxes and reflects incoming shortwave radiation leading to further maintenance. While process budgets diagnose the relative roles of factors, the causality of individual mechanisms are neither isolated nor tested in integrated differences. The explanatory power of the TPV modification experimental framework is in both for the input perturbation.

Stronger TPVs are expected to lead to stronger surface cyclones (Eady 1949; Hoskins et al. 1985), evidenced as well in MPAS-A and CESM-CAM-MPAS TPV modification experiments. Strong surface cyclones generally reduce SIC locally in summer (Kriegsmann and Brümmer 2014). However, results show stronger cyclonic TPVs in the Arctic causing less summer SIE loss. If all are true, a reconciling factor is where the intense TPVs transit. Analogous to the linkages between sea ice loss and the summer polar circulation, intense cyclonic TPVs over the central Arctic may be smaller-scale versions akin to summer 2006, while TPVs on the periphery of the sea ice edge may link an amplified polar jet to marginal sea ice loss like in summer 2007, all else equal. Since the tested local modifications to direct trajectories of TPVs were not effective, targeted testing of the hypothesis would likely require modifying the environment in which TPVs flow.

Ultimately, nature's "true" sensitivity of sea ice to TPVs is arguably unknowable, since history provides but one realization. Moreover, the derived relationships are conditional on the experimental design, prompting a number of questions for further work. Are the same effects produced by structurally different input perturbations, say to moisture, isolated to the core or periphery of a TPV, or to only extreme TPVs? Do the sea ice and ocean states condition the response, say with thinner ice in the future perhaps more responsive in magnitude but less significant in sensitivity? Do different model formulations and process resolutions reproduce similar sensitivities? Note that similar experiments with intensified cyclonic TPVs in the Arctic initialized on 01 August 2006, 15 August 2006, and 01 August 2021 also lead to greater September SIE than their respective controls (not shown).

Chapter 5

Conclusions

Historical events like in summer 2006 show potentially long-lived, coherent vortices based on the tropopause tightly coupled to near-surface forcing appearing to impact Arctic sea ice variability among a multitude of other interactions. The central focus of this thesis is causal testing and dynamical understanding of the degree and mechanisms through which TPVs impact summer Arctic sea ice loss. Sect. 5.1 highlights results from the previous chapters. Sect. 5.2 synthesizes and provides directions for future work.

5.1 Key points

Ch. 2 explores characteristics of modelled TPVs. Three key points are:

- Tracking with a more restrictive definition of lifetime and more robust, variable size, individual cyclonic TPVs in ERA-Interim can exceed radii of 1000 km, amplitudes of 40 K, and lifetimes of 2 months, coincide with multi-day extreme sea ice loss, and contribute seasonal-scale geographic anomalies.

- ECMWF ensemble forecasts exhibit a systematic model error of weak TPV intensification relative to ERA-Interim analysis, where errors in individual forecasts can exceed 3 K d^{-1}.

- TPVs in experiments with a hierarchy of model complexity exhibit little sensitivity to physics options and larger differences in structure and process rates to model states and horizontal mesh spacing, with finer features evident at higher resolution.

Ch. 3 develops a framework more suitable for evaluating the impacts of TPVs on summer Arctic sea ice loss. Three key points regarding CESM-CAM-MPAS are:

- A global, Arctic-refined atmospheric configuration efficiently provides needed local resolution to TPVs with two-way feedbacks to the polar circulation and beyond.

- Coupling with an Earth system model evolves sea ice through process-based exchanges. With mixed historical and analog initial conditions intended to balance considerations of realism and consistency, summer simulations capture mean polar circulation anomalies and yield competitive September sea ice extent forecasts with skill for the sea ice edge.

- An effective, localized tendency-based modification strategy permits sensitivity experiments to quantify causal responses throughout the Earth system to input TPV perturbations.

Ch. 4 evaluates the impacts of TPVs on summer "2006" Arctic sea ice loss using integrated dynamical sensitivity experiments. Three key points are:

- Strong intensification of cyclonic TPVs in the Arctic can cause less summer sea ice loss.

- Multi-scale, thermodynamic, mechanical, and multi-component mechanisms contribute to differences in sea ice mass, momentum, and energy, with reduced upward surface ocean heat fluxes the largest of the factors associated with maintaining ice cover.

- The artificial intensification sufficient to realize sensitivity significant with respect to historical and internal variability in individual simulations of July through September 2006 is near -5 K d^{-1}.

5.2 Synthesis

In sensitivity experiments using a dynamical coupled Earth system model, directly introduced intensity errors in individual upper-level cyclones in the Arctic can lead to less

summer sea ice loss than in the satellite-era record and sampled internal climate model variability. The scale of input perturbations needed to significantly change the trajectory of a fundamental component of the Earth system is within the order of errors exhibited by operational forecasts. Characteristics and roles of TPV shape and place and integrated atmosphere-sea ice-ocean coupling emerge as important factors and direct future work.

The shape and place of TPVs condition their characteristics and impacts. Within vortices, a coherent core region can be dominated by diabatic EPV tendencies and wind shear-influenced edge by frictional tendencies. With maintenance tied to the coherent structure, individual vortices can traverse the Arctic for months. Their paths and associated anomalies define the diagnosed, aggregated impacts geographically. For sea ice, sensitivities to more intense cyclonic TPVs in the Arctic can cause extremely less summer sea ice loss. The same large modifications to cyclones outside the Arctic or anti-cyclones do not generate significant SIE sensitivities in individual simulations. Given apparent systematic errors for TPVs and their linkages in ECMWF forecasts and simulations at CESM-LE scales, errors in these benchmark configurations raise concerns and possibilities for improving representations of TPVs with further propagating sensitivities.

Atmosphere, sea ice, and ocean interactions are central to how intense cyclonic TPVs in the Arctic can reduce summer sea ice loss. In response to perturbations input near the tropopause, driving differences in surface ocean heat fluxes and absorbed radiation to marginal sea ice concentration feedback with the sea ice cover and overlying atmosphere. These couplings raise concerns about studies that decouple the components, e.g., without consistently evolving atmosphere (Zhang et al. 2013) or sea ice and ocean budgets (Wernli and Papritz 2018). Even with coupled components, smoothing evident in finer features and higher frequencies suggest errors in representing the range of multi-scale interactions. While the energy or variability at fine scales may be smaller (e.g., Fig. 3.1 or Skamarock (2011)), systematic errors in transient TPVs at O(100 km) and larger scales can generate historic sea ice sensitivities.

5.2.1 Future directions for process and prediction studies

A general perspective guiding this work is that causal, dynamical linkages help disentangle, evaluate, and clarify interactions throughout the coupled Earth system. Applying the perspective to improve initialization, process representation, and dynamical understanding are available avenues for future work.

Sea ice forecast skill depends on sea ice initialization (e.g., Blockley and Peterson (2018)). Climate analogs do not provide particularly accurate historical initial conditions. Likely as a result, non-conventionally, skill for the sea ice edge in conducted CESM-CAM-MPAS forecasts can increase with lead time. However, perturbing the model towards more accurate initial conditions can entangle the physical processes and state-adjustments within the model-generated tendencies. Significant adjustments limit use as a process model, particularly for Earth system components with longer adjustment timescales from slower processes. Coupled data assimilation may offer more consistent and accurate initial model states (e.g., Zhang et al. (2007)). The exhibited linkages between TPVs and sea ice further confirm that both process-rates and uncertainties are coupled throughout the Earth system. Leveraging these connections may allow fuller use of observations or direct new ones. Repeated, in situ sampling within a TPV may be possible for weeks with drifting balloons (e.g., Angell (1961)). Observed sea ice drift can inform atmosphere and ocean forcing (Eq. 3.2), particularly in freer drifting marginal areas. Both could be incorporated into strategies targeting areas for model improvement (Klinker and Sardeshmukh 1992; Cavallo et al. 2016).

Static variable-resolution offers the ability to couple different scales, regimes, and geographic areas with some flexibility to achieve desired efficiency and consistency. While meshes can be designed to suit specified objectives or constraints (e.g., Baker (1997)), the optimal meshes for Earth system simulations are not solved problems. In practice, sampling of uncertainty (e.g., through ensembles), spatial resolution (e.g., grid spacing), and

process complexity (e.g., physics parameterizations and couplings) are balanced with limited resources.

To complement other approaches, CESM-CAM-MPAS is perhaps best contextualized within more general model hierarchies (e.g., Held (2005)) as complexly coupled with horizontally-resolved (sub)synoptic features and coarsely-resolved processes. The model allows for a range of controlled experiments. Serreze et al. (2016) raise concerns over the degree to which details in broad summer polar circulation patterns qualify expectations of anomalous September SIE. Further isolating the roles of individual mechanisms already represented (e.g., clouds on surface forcing (Intrieri et al. 2002)) may benefit from further process or feature denial/modification experiments. Reproducing pathways with complementary models would increase confidence in their realism and robustness. As the Arctic warms, the marginal ice zone widens (Strong et al. 2017). Not or coarsely represented in these CESM-CAM-MPAS simulations are wave coupling, sea ice floe dynamics, and ocean eddies (e.g., Johannessen et al. (1987); Wadhams et al. (1988)) that play larger roles with less pack ice.

While TPV–sea ice linkages are the focus here, impacts of TPVs on surface cyclones, polar jet amplification, stratosphere–troposphere exchange, oceanic circulations, and more can be explored with similar forward sensitivity analysis. Direct perturbations elsewhere (e.g., other features, processes, or regions) are also possible, with climate geoengineering and coupled data assimilation among the multitude of applications.

Bibliography

Anderson, J. L., and S. L. Anderson, 1999: A monte carlo implementation of the nonlinear filtering problem to produce ensemble assimilations and forecasts. *Mon. Wea. Rev.*, **127 (12)**, 2741–2758.

Añel, J. A., J. C. Antuña, L. de la Torre, J. M. Castanheira, and L. Gimeno, 2008: Climatological features of global multiple tropopause events. *J. Geophys. Res.*, **113 (D7)**.

Angell, J., 1961: Use of constant level balloons in meteorology. *Advances in geophysics*, Vol. 8, Elsevier, 137–219.

Arrigo, K. R., and Coauthors, 2012: Massive phytoplankton blooms under Arctic sea ice. *Science*, **336 (6087)**, 1408–1408.

Asplin, M. G., R. Galley, D. G. Barber, and S. Prinsenberg, 2012: Fracture of summer perennial sea ice by ocean swell as a result of Arctic storms. *J. Geophys. Res.*, **117 (C6)**.

Baker, T. J., 1997: Mesh adaptation strategies for problems in fluid dynamics. *Finite Elements in Analysis and Design*, **25 (3-4)**, 243–273.

Barnes, E. A., and J. A. Screen, 2015: The impact of Arctic warming on the midlatitude jet-stream: Can it? Has it? Will it? *Wiley Interdisciplinary Reviews: Climate Change*, **6 (3)**, 277–286.

Bauer, P., A. Thorpe, and G. Brunet, 2015: The quiet revolution of numerical weather prediction. *Nature*, **525 (7567)**, 47.

Béguin, A., O. Martius, M. Sprenger, P. Spichtinger, D. Folini, and H. Wernli, 2012: Tropopause level rossby wave breaking in the northern hemisphere: a feature-based validation of the ECHAM5-HAM climate model. *Int. J. Climatol.*

Bentsen, M., and Coauthors, 2013: The Norwegian earth system model, NorESM1-M—Part 1: Description and basic evaluation of the physical climate. *Geosci. Model Dev*, **6 (3)**, 687–720.

Blackman, R. B., and J. W. Tukey, 1958: The measurement of power spectra from the point of view of communications engineering—part i. *Bell System Technical Journal*, **37 (1)**, 185–282.

Blockley, E. W., and K. A. Peterson, 2018: Improving Met Office seasonal predictions of Arctic sea ice using assimilation of CryoSat-2 thickness. *The Cryosphere*, **12 (11)**, 3419–3438.

Bloom, S., L. Takacs, A. Da Silva, and D. Ledvina, 1996: Data assimilation using incremental analysis updates. *Mon. Wea. Rev.*, **124 (6)**, 1256–1271.

Boisvert, L. N., A. A. Petty, and J. C. Stroeve, 2016: The impact of the extreme winter 2015/16 Arctic cyclone on the Barents–Kara seas. *Mon. Wea. Rev.*, **144 (11)**, 4279–4287.

Bougeault, P., and Coauthors, 2010: The THORPEX interactive grand global ensemble. *Bull. Amer. Meteor. Soc.*, **91 (8)**, 1059–1072.

Bourassa, M. A., and Coauthors, 2013: High-latitude ocean and sea ice surface fluxes: Challenges for climate research. *Bull. Amer. Meteor. Soc.*, **94 (3)**, 403–423.

Box, G. E., 1979: Robustness in the strategy of scientific model building. *Robustness in statistics*, Elsevier, 201–236.

Browning, K., A. Thorpe, A. Montani, D. Parsons, M. Griffiths, P. Panagi, and E. Dicks, 2000: Interactions of tropopause depressions with an ex–tropical cyclone and sensitivity of forecasts to analysis errors. *Mon. Wea. Rev.*, **128 (8)**, 2734–2755.

Brümmer, B., and H. Hoeber, 1999: A mesoscale cyclone over the Fram Strait and its effects on sea ice. *J. Geophys. Res.*, **104 (D16)**, 19 085–19 098.

Brunet, G., and Coauthors, 2010: Collaboration of the weather and climate communities to advance subseasonal-to-seasonal prediction. *Bull. Amer. Meteor. Soc.*, **91 (10)**, 1397–1406.

Bryan, G. H., J. C. Wyngaard, and J. M. Fritsch, 2003: Resolution requirements for the simulation of deep moist convection. *Mon. Wea. Rev.*, **131 (10)**, 2394–2416.

Catto, J. L., L. C. Shaffrey, and K. I. Hodges, 2010: Can climate models capture the structure of extratropical cyclones? *J. Climate*, **23 (7)**, 1621–1635.

Cavalieri, D. J., B. A. Burns, and R. G. Onstott, 1990: Investigation of the effects of summer melt on the calculation of sea ice concentration using active and passive microwave data. *J. Geophys. Res.*, **95 (C4)**, 5359–5369.

Cavallo, S. M., J. Berner, and C. Snyder, 2016: Diagnosing model errors from time-averaged tendencies in the weather research and forecasting (WRF) model. *Mon. Wea. Rev.*, **144 (2)**, 759–779.

Cavallo, S. M., J. Dudhia, and C. Snyder, 2011: A multilayer upper-boundary condition for longwave radiative flux to correct temperature biases in a mesoscale model. *Mon. Wea. Rev.*, **139 (6)**, 1952–1959.

Cavallo, S. M., and G. J. Hakim, 2009: Potential vorticity diagnosis of a tropopause polar cyclone. *Mon. Wea. Rev.*, **137 (4)**, 1358–1371.

Cavallo, S. M., and G. J. Hakim, 2010: Composite structure of tropopause polar cyclones. *Mon. Wea. Rev.*, **138 (10)**, 3840–3857.

Cavallo, S. M., and G. J. Hakim, 2013: Physical mechanisms of tropopause polar vortex intensity change. *J. Atmos. Sci.*, **70 (11)**, 3359–3373.

Chelton, D., 2001: *Report of the high-resolution ocean topography science working group meeting*. Oregon State University, College of Oceanic and Atmospheric Sciences.

Christiansen, J. S., C. W. Mecklenburg, and O. V. Karamushko, 2014: Arctic marine fishes and their fisheries in light of global change. *Global change biology*, **20 (2)**, 352–359.

CISL, 2016: Computational and Information Systems Laboratory, Yellowstone: IBM iDataPlex System (NCAR Community Computing). *Boulder, CO: National Center for Atmospheric Research*, URL http://n2t.net/ark:/85065/d7wd3xhc.

Collins, W. D., and Coauthors, 2004: Description of the NCAR community atmosphere model (CAM 3.0). *NCAR Tech. Note NCAR/TN-464+ STR*, **226**.

Colony, R., and A. Thorndike, 1984: An estimate of the mean field of Arctic sea ice motion. *J. Geophys. Res.*, **89 (C6)**, 10 623–10 629.

Comiso, J. C., C. L. Parkinson, R. Gersten, and L. Stock, 2008: Accelerated decline in the Arctic sea ice cover. *Geophys. Res. Lett.*, **35 (1)**.

Cosgrove, B. A., and Coauthors, 2003: Land surface model spin-up behavior in the North American Land Data Assimilation System (NLDAS). *J. Geophys. Res.*, **108 (D22)**.

Craig, A. P., M. Vertenstein, and R. Jacob, 2012: A new flexible coupler for earth system modeling developed for CCSM4 and CESM1. *The International Journal of High Performance Computing Applications*, **26 (1)**, 31–42.

Crépin, A.-S., M. Karcher, and J.-C. Gascard, 2017: Arctic climate change, economy and society (ACCESS): Integrated perspectives. *Ambio*, **46 (3)**, 341–354.

Davies, H. C., 1976: A lateral boundary formulation for multi-level prediction models. *Quart. J. Roy. Meteor. Soc.*, **102 (432)**, 405–418.

Davis, C. A., and K. A. Emanuel, 1991: Potential vorticity diagnostics of cyclogenesis. *Mon. Wea. Rev.*, **119 (8)**, 1929–1953.

Dee, D. P., and Coauthors, 2011: The ERA-Interim reanalysis: Configuration and performance of the data assimilation system. *Quart. J. Roy. Meteor. Soc.*, **137 (656)**, 553–597.

Ding, Q., and Coauthors, 2017: Influence of high-latitude atmospheric circulation changes on summertime Arctic sea ice. *Nature Climate Change*, **7 (4)**, 289.

Durran, D. R., and M. Gingrich, 2014: Atmospheric predictability: Why butterflies are not of practical importance. *J. Atmos. Sci.*, **71 (7)**, 2476–2488, doi:10.1175/JAS-D-14-0007.1.

Eady, E. T., 1949: Long waves and cyclone waves. *Tellus*, **1 (3)**, 33–52.

Enderlin, E. M., I. M. Howat, S. Jeong, M.-J. Noh, J. H. Van Angelen, and M. R. Van Den Broeke, 2014: An improved mass budget for the Greenland ice sheet. *Geophys. Res. Lett.*, **41 (3)**, 866–872.

Fang, Z., and J. M. Wallace, 1994: Arctic sea ice variability on a timescale of weeks and its relation to atmospheric forcing. *J. Climate*, **7 (12)**, 1897–1914.

Fetterer, F., K. Knowles, W. Meier, M. Savoie, and A. Windnagel, 2017: Sea ice index, version 3, updated daily. *NSIDC: National Snow and Ice Data Center*, doi:https://doi.org/10.7265/N5K072F8.

Fetterer, F., J. Stewart, and W. Meier, 2015: Masam2: Daily 4 km Arctic sea ice concentration, version 1. *Boulder, Colorado USA. NSIDC: National Snow and Ice Data Center*, doi:https://doi.org/10.7265/N5ZS2TFT.

Frank, M., 2019: Atmospheric conditions preceding very rapid sea ice loss events. M.S. thesis, University of Oklahoma, Norman, Oklahoma, USA.

Friehe, C. A., and K. F. Schmitt, 1976: Parameterization of air-sea interface fluxes of sensible heat and moisture by the bulk aerodynamic formulas. *J. Phys. Oceanogr.*, **6 (6)**, 801–809.

Gautier, D. L., and Coauthors, 2009: Assessment of undiscovered oil and gas in the Arctic. *Science*, **324 (5931)**, 1175–1179.

Gettelman, A., P. Hoor, L. Pan, W. Randel, M. I. Hegglin, and T. Birner, 2011: The extratropical upper troposphere and lower stratosphere. *Rev. Geophys.*, **49 (3)**.

Giorgi, F., and W. J. Gutowski Jr, 2015: Regional dynamical downscaling and the CORDEX initiative. *Annual Review of Environment and Resources*, **40**, 467–490.

Goessling, H., and T. Jung, 2018: A probabilistic verification score for contours: Methodology and application to Arctic ice-edge forecasts. *Quart. J. Roy. Meteor. Soc.*

Grams, C. M., and Coauthors, 2011: The key role of diabatic processes in modifying the upper-tropospheric wave guide: a North Atlantic case-study. *Quart. J. Roy. Meteor. Soc.*, **137 (661)**, 2174–2193.

Graversen, R. G., T. Mauritsen, S. Drijfhout, M. Tjernström, and S. Mårtensson, 2011: Warm winds from the pacific caused extensive Arctic sea-ice melt in summer 2007. *Climate Dyn.*, **36 (11-12)**, 2103–2112.

Grebmeier, J. M., S. E. Moore, J. E. Overland, K. E. Frey, and R. Gradinger, 2010: Biological response to recent pacific Arctic sea ice retreats. *Eos, Trans. Amer. Geophys. Union*, **91 (18)**, 161–162.

Greenert, J. W., 2014: The United States Navy Arctic Roadmap for 2014 to 2030. Tech. rep., Office of the Chief of Naval Operations, Washington D.C.

Grell, G. A., S. R. Freitas, and Coauthors, 2014: A scale and aerosol aware stochastic convective parameterization for weather and air quality modeling. *Atmos. Chem. Phys*, **14 (10)**, 5233–5250.

Guemas, V., and Coauthors, 2016: A review on Arctic sea-ice predictability and prediction on seasonal to decadal time-scales. *Quart. J. Roy. Meteor. Soc.*, **142 (695)**, 546–561.

Guoxiong, W., C. Yaping, and T. Xiaojing, 1995: Moist potential vorticity and slantwise vorticity development. *Acta Meteorologica Sinica*, **4**.

Gupta, A. S., L. C. Muir, J. N. Brown, S. J. Phipps, P. J. Durack, D. Monselesan, and S. E. Wijffels, 2012: Climate drift in the CMIP3 models. *J. Climate*, **25 (13)**, 4621–4640.

Hacker, J., W. Angevine, and K. Arsenault, 2009: A description of the WRFv3.1 single-column model, available online at http://www.mmm.ucar.edu/wrf/users/workshops/WS2009/presentations/5B-03.pdf.

Hagos, S., L. R. Leung, Q. Yang, C. Zhao, and J. Lu, 2015: Resolution and dynamical core dependence of atmospheric river frequency in global model simulations. *J. Climate*, **28 (7)**, 2764–2776.

Hakim, G. J., 2000: Climatology of coherent structures on the extratropical tropopause. *Mon. Wea. Rev.*, **128 (2)**, 385–406.

Hakim, G. J., and A. K. Canavan, 2005: Observed cyclone–anticyclone tropopause vortex asymmetries. *J. Atmos. Sci.*, **62 (1)**, 231–240.

Hamill, T. M., 2001: Interpretation of rank histograms for verifying ensemble forecasts. *Mon. Wea. Rev.*, **129 (3)**, 550–560.

Hamilton, L. C., and J. Stroeve, 2016: 400 predictions: the SEARCH sea ice outlook 2008–2015. *Polar Geography*, **39 (4)**, 274–287.

Hartmann, D. L., 2004: Atmospheric general circulation and climate. *Global physical climatology*, Academic Press, London, chap. 6, 136–169.

Heinemann, G., 2003: Forcing and feedback mechanisms between the katabatic wind and sea ice in the coastal areas of polar ice sheets. *The Global Atmosphere and Ocean System*, **9 (4)**, 169–201.

Held, I. M., 2005: The gap between simulation and understanding in climate modeling. *Bull. Amer. Meteor. Soc.*, **86 (11)**, 1609–1614.

Holland, M. M., C. M. Bitz, and B. Tremblay, 2006: Future abrupt reductions in the summer arctic sea ice. *Geophys. Res. Lett.*, **33 (23)**.

Holland, M. M., C. M. Bitz, B. Tremblay, D. A. Bailey, and Coauthors, 2008: The role of natural versus forced change in future rapid summer Arctic ice loss. *Arctic Sea Ice Decline: Observations, Projections, Mechanisms, and Implications, Geophys. Monogr. Ser*, **180**, 133–150.

Holton, J. R., and G. J. Hakim, 2013: *An introduction to dynamic meteorology*. Academic press.

Hong, S.-Y., and J.-O. J. Lim, 2006: The WRF single-moment 6-class microphysics scheme (WSM6). *J. Korean Meteor. Soc*, **42 (2)**, 129–151.

Hong, S.-Y., Y. Noh, and J. Dudhia, 2006: A new vertical diffusion package with an explicit treatment of entrainment processes. *Mon. Wea. Rev.*, **134 (9)**, 2318–2341.

Hoskins, B. J., M. McIntyre, and A. W. Robertson, 1985: On the use and significance of isentropic potential vorticity maps. *Quart. J. Roy. Meteor. Soc.*, **111 (470)**, 877–946.

Howe, B., 2012: Virtual appliances, cloud computing, and reproducible research. *Computing in Science & Engineering*, **14 (4)**, 36–41.

Hunke, E. C., and W. H. Lipscomb, 2010: CICE: the Los Alamos sea ice model documentation and software user's manual version 4.1. *T-3 Fluid Dynamics Group, Los Alamos National Laboratory*, **LA-CC-06-012**.

Hurrell, J. W., and Coauthors, 2013: The community earth system model: a framework for collaborative research. *Bull. Amer. Meteor. Soc.*, **94 (9)**, 1339–1360.

Iacono, M. J., J. S. Delamere, E. J. Mlawer, M. W. Shephard, S. A. Clough, and W. D. Collins, 2008: Radiative forcing by long-lived greenhouse gases: Calculations with the AER radiative transfer models. *J. Geophys. Res.*, **113 (D13)**.

International Arctic Science Committee, 2018: Multidisciplinary drifting observatory for the study of Arctic climate implementation plan.

Intrieri, J., C. Fairall, M. Shupe, P. Persson, E. Andreas, P. Guest, and R. Moritz, 2002: An annual cycle of arctic surface cloud forcing at SHEBA. *J. Geophys. Res.*, **107 (C10)**, SHE–13.

IPCC, 2007: *Climate Change 2007: The Physical Science Basis. Contribution of Working Group I to the Fourth Assessment Report of the Intergovernmental Panel on Climate Change*. Cambridge University Press.

Itkin, P., and Coauthors, 2017: Thin ice and storms: Sea ice deformation from buoy arrays deployed during N-ICE2015. *J. Geophys. Res.*, **122 (6)**, 4661–4674.

Ivanova, A., 2013: The tropopause: Variety of definitions and modern approaches to identification. *Russian Meteorology and Hydrology*, **38 (12)**, 808.

Ivanova, N., and Coauthors, 2015: Inter-comparison and evaluation of sea ice algorithms: towards further identification of challenges and optimal approach using passive microwave observations. *The Cryosphere*, **9 (5)**, 1797–1817.

Jahn, A., J. E. Kay, M. M. Holland, and D. M. Hall, 2016: How predictable is the timing of a summer ice-free Arctic? *Geophys. Res. Lett.*, **43 (17)**, 9113–9120.

Jimenez, I., C. Maltzahn, A. Moody, K. Mohror, J. Lofstead, R. Arpaci-Dusseau, and A. Arpaci-Dusseau, 2015: The role of container technology in reproducible computer systems research. *2015 IEEE International Conference on Cloud Engineering (IC2E)*, IEEE, 379–385.

Johannessen, J., and Coauthors, 1987: Mesoscale eddies in the Fram Strait marginal ice zone during the 1983 and 1984 Marginal Ice Zone Experiments. *J. Geophys. Res.*, **92 (C7)**, 6754–6772.

Ju, L., T. Ringler, and M. Gunzburger, 2011: Voronoi tessellations and their application to climate and global modeling. *Numerical Techniques for Global Atmospheric Models*, Springer, 313–342.

Judt, F., 2018: Insights into atmospheric predictability through global convection-permitting model simulations. *J. Atmos. Sci.*, **75 (5)**, 1477–1497.

Jun, S.-Y., S.-J. Choi, and B.-M. Kim, 2018: Dynamical core in atmospheric model does matter in the simulation of Arctic climate. *Geophys. Res. Lett.*

Jung, T., S. Gulev, I. Rudeva, and V. Soloviov, 2006: Sensitivity of extratropical cyclone characteristics to horizontal resolution in the ECMWF model. *Quart. J. Roy. Meteor. Soc.*, **132 (619)**, 1839–1857.

Jung, T., and Coauthors, 2016: Advancing polar prediction capabilities on daily to seasonal time scales. *Bull. Amer. Meteor. Soc.*, **97 (9)**, 1631–1647.

Kain, J. S., and J. M. Fritsch, 1993: Convective parameterization for mesoscale models: The Kain-Fritsch scheme. *The representation of cumulus convection in numerical models*, Springer, 165–170.

Karspeck, A. R., S. Yeager, G. Danabasoglu, T. Hoar, N. Collins, K. Raeder, J. Anderson, and J. Tribbia, 2013: An ensemble adjustment Kalman filter for the CCSM4 ocean component. *J. Climate*, **26 (19)**, 7392–7413.

Kattsov, V. M., V. E. Ryabinin, J. E. Overland, M. C. Serreze, M. Visbeck, J. E. Walsh, W. Meier, and X. Zhang, 2010: Arctic sea-ice change: a grand challenge of climate science. *Journal of Glaciology*, **56 (200)**, 1115–1121.

Kawaguchi, Y., J. K. Hutchings, T. Kikuchi, J. H. Morison, and R. A. Krishfield, 2012: Anomalous sea-ice reduction in the Eurasian Basin of the Arctic ocean during summer 2010. *Polar Science*, **6 (1)**, 39–53.

Kay, J., and Coauthors, 2015: The community earth system model (CESM) large ensemble project: A community resource for studying climate change in the presence of internal climate variability. *Bull. Amer. Meteor. Soc.*, **96 (8)**, 1333–1349.

Kay, J. E., T. L'Ecuyer, A. Gettelman, G. Stephens, and C. O'Dell, 2008: The contribution of cloud and radiation anomalies to the 2007 Arctic sea ice extent minimum. *Geophys. Res. Lett.*, **35 (8)**.

Kew, S. F., M. Sprenger, and H. C. Davies, 2010: Potential vorticity anomalies of the lowermost stratosphere: A 10-yr winter climatology. *Mon. Wea. Rev.*, **138 (4)**, 1234–1249.

Kidston, J., A. A. Scaife, S. C. Hardiman, D. M. Mitchell, N. Butchart, M. P. Baldwin, and L. J. Gray, 2015: Stratospheric influence on tropospheric jet streams, storm tracks and surface weather. *Nature Geoscience*, **8 (6)**, 433.

Klemp, J., J. Dudhia, and A. Hassiotis, 2008: An upper gravity-wave absorbing layer for NWP applications. *Mon. Wea. Rev.*, **136 (10)**, 3987–4004.

Klinker, E., and P. D. Sardeshmukh, 1992: The diagnosis of mechanical dissipation in the atmosphere from large-scale balance requirements. *J. Atmos. Sci.*, **49 (7)**, 608–627.

Knudsen, E. M., Y. J. Orsolini, T. Furevik, and K. I. Hodges, 2015: Observed anomalous atmospheric patterns in summers of unusual Arctic sea ice melt. *J. Geophys. Res.*, **120 (7)**, 2595–2611.

Krejcie, R. V., and D. W. Morgan, 1970: Determining sample size for research activities. *Educational and psychological measurement*, **30 (3)**, 607–610.

Kriegsmann, A., and B. Brümmer, 2014: Cyclone impact on sea ice in the central Arctic ocean: a statistical study. *The Cryosphere*, **8 (1)**, 303–317.

Kumar, A., and M. Chen, 2015: Inherent predictability, requirements on the ensemble size, and complementarity. *Mon. Wea. Rev.*, **143 (8)**, 3192–3203.

Kwok, R., 2002: Sea ice concentration estimates from satellite passive microwave radiometry and openings from sar ice motion. *Geophys. Res. Lett.*, **29 (9)**, 25–1.

Kwok, R., 2018: Arctic sea ice thickness, volume, and multiyear ice coverage: losses and coupled variability (1958–2018). *Environmental Research Letters*, **13 (10)**, 105 005.

Kwok, R., G. Spreen, and S. Pang, 2013: Arctic sea ice circulation and drift speed: Decadal trends and ocean currents. *J. Geophys. Res.*, **118 (5)**, 2408–2425.

Kwok, R., and D. Sulsky, 2010: Arctic Ocean sea ice thickness and kinematics: Satellite retrievals and modeling. *Oceanography*, **23 (4)**, 134–143.

Laing, A., and J.-L. Evans, 2011: Introduction to Tropical Meteorology. [Online; accessed 20-January-2014], http://www.meted.ucar.edu/tropical/textbook_2nd_edition/print_1.htm.

Laprise, R., and Coauthors, 2008: Challenging some tenets of regional climate modelling. *Meteorology and Atmospheric Physics*, **100 (1-4)**, 3–22.

Large, W. G., and S. Yeager, 2009: The global climatology of an interannually varying air–sea flux data set. *Climate Dyn.*, **33 (2-3)**, 341–364.

Leduc, M., and R. Laprise, 2009: Regional climate model sensitivity to domain size. *Climate Dyn.*, **32 (6)**, 833–854.

Lee, C. M., S. Cole, M. Doble, S. Harper, J. MacKinnon, and Coauthors, 2016: Stratified ocean dynamics of the Arctic: Science and experiment plan. Tech. rep., Applied Physics Laboratory, University of Washington, Seattle.

Legras, B., D. G. Dritschel, and P. Caillol, 2001: The erosion of a distributed two-dimensional vortex in a background straining flow. *Journal of Fluid Mechanics*, **441**, 369–398.

Lin, S.-J., 2004: A "vertically lagrangian" finite-volume dynamical core for global models. *Mon. Wea. Rev.*, **132 (10)**, 2293–2307.

Lorenz, E. N., 1969a: Atmospheric predictability as revealed by naturally occurring analogues. *J. Atmos. Sci.*, **26 (4)**, 636–646.

Lorenz, E. N., 1969b: The predictability of a flow which possesses many scales of motion. *Tellus*, **21 (3)**, 289–307.

Lovecraft, A. L., 2013: The human geography of Arctic sea ice: introduction. *Polar Geography*, **36 (1-2)**, 1–4.

Mariotti, A., B. Legras, and D. G. Dritschel, 1994: Vortex stripping and the erosion of coherent structures in two-dimensional flows. *Physics of Fluids*, **6 (12)**, 3954–3962.

Markus, T., J. C. Stroeve, and J. Miller, 2009: Recent changes in Arctic sea ice melt onset, freezeup, and melt season length. *J. Geophys. Res.*, **114 (C12)**.

Maslanik, J., 1992: Effects of weather on the retrieval of sea ice concentration and ice type from passive microwave data. *International Journal of Remote Sensing*, **13 (1)**, 37–54.

Maslowski, W., J. Clement Kinney, M. Higgins, and A. Roberts, 2012: The future of Arctic sea ice. *Annual Review of Earth and Planetary Sciences*, **40**, 625–654.

Mauritzen, C., and S. Häkkinen, 1997: Influence of sea ice on the thermohaline circulation in the Arctic-North Atlantic Ocean. *Geophys. Res. Lett.*, **24 (24)**, 3257–3260.

Maykut, G. A., 1978: Energy exchange over young sea ice in the central Arctic. *J. Geophys. Res.*, **83 (C7)**, 3646–3658.

Mcnutt, S. L., and J. E. Overland, 2003: Spatial hierarchy in Arctic sea ice dynamics. *Tellus A: Dynamic Meteorology and Oceanography*, **55 (2)**, 181–191.

McPhee, M., 2008: *Air-ice-ocean interaction: Turbulent ocean boundary layer exchange processes*. Springer Science & Business Media.

McPhee, M., R. Kwok, R. Robins, and M. Coon, 2005: Upwelling of Arctic pycnocline associated with shear motion of sea ice. *Geophys. Res. Lett.*, **32 (10)**.

Meier, W. N., and Coauthors, 2014: Arctic sea ice in transformation: A review of recent observed changes and impacts on biology and human activity. *Reviews of Geophysics*, **52 (3)**, 185–217.

Meinshausen, M., and Coauthors, 2011: The RCP greenhouse gas concentrations and their extensions from 1765 to 2300. *Climatic Change*, **109 (1-2)**, 213.

Melia, N., K. Haines, and E. Hawkins, 2016: Sea ice decline and 21st century trans-Arctic shipping routes. *Geophys. Res. Lett.*, **43 (18)**, 9720–9728.

Melnikov, A., 1997: *Arctic Sea Ice Ecosystem*. CRC Press.

Mercator, G., 1595: Septentrionalium terrarum descriptio. doi:10.14288/1.0224509.

Michalakes, J., and Coauthors, 2015: AVEC Report: NGGPS Level-1 Benchmarks and software evaluation. Tech. rep., NGGPS Dynamical Core Test Group.

Miguez-Macho, G., G. L. Stenchikov, and A. Robock, 2004: Spectral nudging to eliminate the effects of domain position and geometry in regional climate model simulations. *J. Geophys. Res.*, **109 (D13)**.

Mlawer, E. J., S. J. Taubman, P. D. Brown, M. J. Iacono, and S. A. Clough, 1997: Radiative transfer for inhomogeneous atmospheres: RRTM, a validated correlated-k model for the longwave. *J. Geophys. Res.*, **102 (D14)**, 16 663–16 682.

Morgan, M. C., and J. W. Nielsen-Gammon, 1998: Using tropopause maps to diagnose midlatitude weather systems. *Mon. Wea. Rev.*, **126 (10)**, 2555–2579.

Morrison, H., G. Thompson, and V. Tatarskii, 2009: Impact of cloud microphysics on the development of trailing stratiform precipitation in a simulated squall line: Comparison of one-and two-moment schemes. *Mon. Wea. Rev.*, **137 (3)**, 991–1007.

Muench, R. D., P. H. LeBlond, and L. E. Hachmeister, 1983: On some possible interactions between internal waves and sea ice in the marginal ice zone. *J. Geophys. Res.*, **88 (C5)**, 2819–2826.

Mulholland, D. P., P. Laloyaux, K. Haines, and M. A. Balmaseda, 2015: Origin and impact of initialization shocks in coupled atmosphere–ocean forecasts. *Mon. Wea. Rev.*, **143 (11)**, 4631–4644.

Murphy, J. M., D. M. Sexton, D. N. Barnett, G. S. Jones, M. J. Webb, M. Collins, and D. A. Stainforth, 2004: Quantification of modelling uncertainties in a large ensemble of climate change simulations. *Nature*, **430 (7001)**, 768.

Mysak, L. A., and S. A. Venegas, 1998: Decadal climate oscillations in the arctic: A new feedback loop for atmosphere-ice-ocean interactions. *Geophys. Res. Lett.*, **25 (19)**, 3607–3610.

Nakanishi, M., and H. Niino, 2004: An improved Mellor–Yamada level-3 model with condensation physics: Its design and verification. *Boundary-Layer Meteorology*, **112 (1)**, 1–31.

Nansen, F., 1897: *Farthest North*, Vol. 1. Harper & Brothers.

National Snow and Ice Data Center, 2018: All About Sea Ice. Accessed 25 December 2018, /cryosphere/seaice/index.html.

Neale, R. B., and Coauthors, 2010: Description of the NCAR community atmosphere model (CAM 5.0). *NCAR Tech. Note NCAR/TN-486+ STR*, **1 (1)**, 1–274.

Nieto, R., M. Sprenger, H. Wernli, R. Trigo, and L. Gimeno, 2008: Identification and climatology of cut-off lows near the tropopause. *Annals of the New York Academy of Sciences*, **1146 (1)**, 256–290.

Nutter, P., D. Stensrud, and M. Xue, 2004: Effects of coarsely resolved and temporally interpolated lateral boundary conditions on the dispersion of limited-area ensemble forecasts. *Mon. Wea. Rev.*, **132 (10)**, 2358–2377.

Oberkampf, W. L., and C. J. Roy, 2010: *Verification and validation in scientific computing*. Cambridge University Press.

Olason, E., and D. Notz, 2014: Drivers of variability in arctic sea-ice drift speed. *J. Geophys. Res.*, **119 (9)**, 5755–5775.

Onarheim, I. H., T. Eldevik, L. H. Smedsrud, and J. C. Stroeve, 2018: Seasonal and regional manifestation of Arctic sea ice loss. *J. Climate*, **31 (12)**, 4917–4932.

Ono, J., J. Inoue, A. Yamazaki, K. Dethloff, and H. Yamaguchi, 2016: The impact of radiosonde data on forecasting sea-ice distribution along the northern sea route during an extremely developed cyclone. *Journal of Advances in Modeling Earth Systems*, **8 (1)**, 292–303.

Ottino, J. M., and J. Ottino, 1989: *The kinematics of mixing: stretching, chaos, and transport*, Vol. 3. Cambridge university press.

Overland, J., J. A. Francis, R. Hall, E. Hanna, S.-J. Kim, and T. Vihma, 2015: The melting Arctic and midlatitude weather patterns: Are they connected? *J. Climate*, **28 (20)**, 7917–7932.

Pang, H., and G. Fu, 2017: Case study of potential vorticity tower in three explosive cyclones over Eastern Asia. *J. Atmos. Sci.*, **74 (5)**, 1445–1454.

Park, S.-H., J. B. Klemp, and W. C. Skamarock, 2014: A comparison of mesh refinement in the global MPAS-A and WRF models using an idealized normal-mode baroclinic wave simulation. *Mon. Wea. Rev.*, **142 (10)**, 3614–3634.

Pedlosky, J., 2013: *Geophysical fluid dynamics*. Springer Science & Business Media.

Peralta-Ferriz, C., and R. A. Woodgate, 2015: Seasonal and interannual variability of pan-Arctic surface mixed layer properties from 1979 to 2012 from hydrographic data, and the dominance of stratification for multiyear mixed layer depth shoaling. *Progress in Oceanography*, **134**, 19–53.

Perovich, D. K., 2005: On the aggregate-scale partitioning of solar radiation in Arctic sea ice during the Surface Heat Budget of the Arctic Ocean (SHEBA) field experiment. *J. Geophys. Res.*, **110 (C3)**.

Petterssen, S., and S. J. Smebye, 1971: On the development of extratropical cyclones. *Quart. J. Roy. Meteor. Soc.*, **97 (414)**, 457–482.

Petty, A. A., J. K. Hutchings, J. A. Richter-Menge, and M. A. Tschudi, 2016: Sea ice circulation around the Beaufort Gyre: The changing role of wind forcing and the sea ice state. *J. Geophys. Res.*, **121 (5)**, 3278–3296.

Polashenski, C., D. Perovich, and Z. Courville, 2012: The mechanisms of sea ice melt pond formation and evolution. *J. Geophys. Res.*, **117 (C1)**.

Porter, D. F., J. J. Cassano, M. C. Serreze, and D. N. Kindig, 2010: New estimates of the large-scale Arctic atmospheric energy budget. *J. Geophys. Res.*, **115 (D8)**.

Provenzale, A., 1999: Transport by coherent barotropic vortices. *Annual review of fluid mechanics*, **31 (1)**, 55–93.

Pyle, M. E., D. Keyser, and L. F. Bosart, 2004: A diagnostic study of jet streaks: Kinematic signatures and relationship to coherent tropopause disturbances. *Mon. Wea. Rev.*, **132 (1)**, 297–319.

Rasmussen, E., 1985: A case study of a polar low development over the Barents Sea. *Tellus A*, **37 (5)**, 407–418.

Razavi, S., and H. V. Gupta, 2015: What do we mean by sensitivity analysis? The need for comprehensive characterization of "global" sensitivity in earth and environmental systems models. *Water Resources Research*, **51 (5)**, 3070–3092.

Reigstad, M., T. Eldevik, and S. Gerland, 2017: The Nansen Legacy. Scientific exploration and sustainable management beyond the ice edge. Overall Project plan.

Rigor, I. G., J. M. Wallace, and R. L. Colony, 2002: Response of sea ice to the Arctic oscillation. *J. Climate*, **15 (18)**, 2648–2663.

Ringler, T., J. Thuburn, J. Klemp, and W. Skamarock, 2010: A unified approach to energy conservation and potential vorticity dynamics for arbitrarily-structured c-grids. *Journal of Computational Physics*, **229 (9)**, 3065–3090.

Roberts, A., and Coauthors, 2015: Simulating transient ice-ocean Ekman transport in the Regional Arctic System Model and Community Earth System Model. *Annals of Glaciology*, **56 (69)**, 211–228.

Rothrock, D. A., Y. Yu, and G. A. Maykut, 1999: Thinning of the Arctic sea-ice cover. *Geophys. Res. Lett.*, **26 (23)**, 3469–3472.

Rummukainen, M., 2010: State-of-the-art with regional climate models. *Wiley Interdisciplinary Reviews: Climate Change*, **1 (1)**, 82–96.

Rutledge, G. K., J. Alpert, and W. Ebisuzaki, 2006: NOMADS: A climate and weather model archive at the National Oceanic and Atmospheric Administration. *Bull. Amer. Meteor. Soc.*, **87 (3)**, 327–342.

Saffin, L., J. Methven, and S. Gray, 2016: The non-conservation of potential vorticity by a dynamical core compared with the effects of parametrized physical processes. *Quart. J. Roy. Meteor. Soc.*, **142 (696)**, 1265–1275.

Screen, J. A., I. Simmonds, and K. Keay, 2011: Dramatic interannual changes of perennial Arctic sea ice linked to abnormal summer storm activity. *J. Geophys. Res.*, **116 (D15)**.

Serreze, M., 2009: Northern hemisphere cyclone locations and characteristics from NCEP/NCAR reanalysis data, version 1. *Boulder, Colorado USA. NSIDC: National Snow and Ice Data Center*, doi:https://doi.org/10.5067/XEPCLZKPAJBK.

Serreze, M. C., and R. G. Barry, 2011: Processes and impacts of Arctic amplification: A research synthesis. *Global Planet. Change*, **77 (1-2)**, 85–96.

Serreze, M. C., and J. Stroeve, 2015: Arctic sea ice trends, variability and implications for seasonal ice forecasting. *Philos. Trans. Roy. Soc. London*, **373 (2045)**, 20140 159.

Serreze, M. C., J. Stroeve, A. P. Barrett, and L. N. Boisvert, 2016: Summer atmospheric circulation anomalies over the arctic ocean and their influences on september sea ice extent: A cautionary tale. *J. Geophys. Res.*, **121 (19)**, 11–463.

Shapiro, M., T. Hampel, and A. Krueger, 1987: The Arctic tropopause fold. *Mon. Wea. Rev.*, **115 (2)**, 444–454.

Simmonds, I., and I. Rudeva, 2012: The great Arctic cyclone of August 2012. *Geophys. Res. Lett.*, **39 (23)**.

Simmonds, I., and I. Rudeva, 2014: A comparison of tracking methods for extreme cyclones in the Arctic basin. *Tellus A: Dynamic Meteorology and Oceanography*, **66 (1)**, 25 252.

Skamarock, W. C., 2011: Kinetic energy spectra and model filters. *Numerical Techniques for Global Atmospheric Models*, Springer, 495–512.

Skamarock, W. C., J. B. Klemp, M. G. Duda, L. D. Fowler, S.-H. Park, and T. D. Ringler, 2012: A multiscale nonhydrostatic atmospheric model using centroidal Voronoi tesselations and C-grid staggering. *Mon. Wea. Rev.*, **140 (9)**, 3090–3105.

Skamarock, W. C., S.-H. Park, J. B. Klemp, and C. Snyder, 2014: Atmospheric kinetic energy spectra from global high-resolution nonhydrostatic simulations. *J. Atmos. Sci.*, **71 (11)**, 4369–4381.

Skamarock, W. C., and Coauthors, 2008: A description of the advanced research WRF version 3. Tech. rep., National Center For Atmospheric Research, Mesoscale and Microscale Meteorology Division.

Small, R. J., and Coauthors, 2014: A new synoptic scale resolving global climate simulation using the community earth system model. *Journal of Advances in Modeling Earth Systems*, **6 (4)**, 1065–1094.

Spreen, G., L. Kaleschke, and G. Heygster, 2008: Sea ice remote sensing using AMSR-E 89-GHz channels. *J. Geophys. Res.*, **113 (C2)**.

Sprenger, M., H. Wernli, and M. Bourqui, 2007: Stratosphere-troposphere exchange and its relation to potential vorticity streamers and cutoffs near the extratropical tropopause. *J. Atmos. Sci.*, **64 (5)**, 1587–1602.

Squire, V., 2007: Of ocean waves and sea-ice revisited. *Cold Regions Science and Technology*, **49 (2)**, 110–133.

Steeneveld, G., B. Van de Wiel, and A. Holtslag, 2006: Modelling the Arctic stable boundary layer and its coupling to the surface. *Boundary-layer meteorology*, **118 (2)**, 357–378.

Stensrud, D. J., 2009: *Parameterization schemes: keys to understanding numerical weather prediction models*. Cambridge University Press.

Stroeve, J., M. M. Holland, W. Meier, T. Scambos, and M. Serreze, 2007: Arctic sea ice decline: Faster than forecast. *Geophys. Res. Lett.*, **34 (9)**.

Stroeve, J., and Coauthors, 2017: Sea ice outlook june report. SIPN, URL https://www.arcus.org/sipn/sea-ice-outlook/2017/june, [Online; posted 30-June-2017].

Strong, C., D. Foster, E. Cherkaev, I. Eisenman, and K. M. Golden, 2017: On the definition of marginal ice zone width. *J. Atmos. Oceanic Technol.*, **34 (7)**, 1565–1584.

Sutherland, P. C., 1852: *Journal of a Voyage in Baffin's Bay and Barrow Straits in the Years 1850-1851*, Vol. 2. Longman, Brown, Green, and Longmans.

Szapiro, N., and S. Cavallo, 2018: TPVTrack v1.0: a watershed segmentation and overlap correspondence method for tracking tropopause polar vortices. *Geosci. Model Dev.*, **11 (12)**, 5173–5187.

Szapiro, N., S. Cavallo, W. Skamarock, and S.-H. Park, 2017: Arctic extended-range predictions with MPAS and MPAS-CESM, 24th Conference on Numerical Weather Prediction. Available at https://bit.ly/2XdBv4t.

Tao, W., J. Zhang, and X. Zhang, 2017: The role of stratosphere vortex downward intrusion in a long-lasting late-summer Arctic storm. *Quart. J. Roy. Meteor. Soc.*, **143 (705)**, 1953–1966.

Tewari, M., and Coauthors, 2004: Implementation and verification of the unified NOAH land surface model in the WRF model. *20th conference on weather analysis and forecasting/16th conference on numerical weather prediction*, Vol. 1115.

Thorpe, A. J., 1986: Synoptic scale disturbances with circular symmetry. *Mon. Wea. Rev.*, **114 (7)**, 1384–1389.

Thuburn, J., T. D. Ringler, W. C. Skamarock, and J. B. Klemp, 2009: Numerical representation of geostrophic modes on arbitrarily structured c-grids. *Journal of Computational Physics*, **228 (22)**, 8321–8335.

Tiedtke, M., 1989: A comprehensive mass flux scheme for cumulus parameterization in large-scale models. *Mon. Wea. Rev.*, **117 (8)**, 1779–1800.

Tilinina, N., S. K. Gulev, and D. H. Bromwich, 2014: New view of Arctic cyclone activity from the Arctic system reanalysis. *Geophys. Res. Lett.*, **41 (5)**, 1766–1772.

Torbert, S., 2016: *Applied Computer Science*. Springer, doi:10.1007/978-3-319-30866-1.

Torn, R. D., and G. J. Hakim, 2008: Ensemble-based sensitivity analysis. *Mon. Wea. Rev.*, **136 (2)**, 663–677.

Tripathi, O. P., and Coauthors, 2015: The predictability of the extratropical stratosphere on monthly time-scales and its impact on the skill of tropospheric forecasts. *Quart. J. Roy. Meteor. Soc.*, **141 (689)**, 987–1003.

Tschudi, M., C. Fowler, J. Maslanik, J. Stewart, and W. Meier, 2016: Polar pathfinder daily 25 km EASE-grid sea ice motion vectors, version 3. *NASA National Snow and Ice Data Center Distributed Active Archive Center*, doi:https://doi.org/10.5067/O57VAIT2AYYY.

Turner, D., A. Merrelli, D. Vimont, and E. Mlawer, 2012: Impact of modifying the longwave water vapor continuum absorption model on community earth system model simulations. *J. Geophys. Res.*, **117 (D4)**.

Ullrich, P. A., and Coauthors, 2017: DCMIP2016: a review of non-hydrostatic dynamical core design and intercomparison of participating models. *Geoscientific Model Development*, **10 (12)**, 4477.

Vavrus, S., M. M. Holland, and D. A. Bailey, 2011: Changes in Arctic clouds during intervals of rapid sea ice loss. *Climate Dyn.*, **36 (7-8)**, 1475–1489.

Wadhams, P., V. A. Squire, D. J. Goodman, A. M. Cowan, and S. C. Moore, 1988: The attenuation rates of ocean waves in the marginal ice zone. *J. Geophys. Res.*, **93 (C6)**, 6799–6818.

Wang, J., J. Zhang, E. Watanabe, M. Ikeda, K. Mizobata, J. E. Walsh, X. Bai, and B. Wu, 2009: Is the dipole anomaly a major driver to record lows in Arctic summer sea ice extent? *Geophys. Res. Lett.*, **36 (5)**.

Wedi, N., and Coauthors, 2015: *The modelling infrastructure of the Integrated Forecasting System: Recent advances and future challenges*. 44th session of ECMWF's Scientific Advisory Committee.

Wernli, H., and L. Papritz, 2018: Role of polar anticyclones and mid-latitude cyclones for Arctic summertime sea-ice melting. *Nature Geoscience*, **11 (2)**, 108.

WGASF, 2000: Final report of the joint WCRP/SCOR working group on air-sea fluxes: Intercomparison and validation of ocean-atmosphere energy flux fields. Tech. rep., World Climate Research Programme.

Williamson, D. L., 2002: Time-split versus process-split coupling of parameterizations and dynamical core. *Mon. Wea. Rev.*, **130 (8)**, 2024–2041.

Wirth, V., M. Riemer, E. K. Chang, and O. Martius, 2018: Rossby wave packets on the midlatitude waveguide – a review. *Mon. Wea. Rev.*, **146**, 1965–2001.

Yamagami, A., M. Matsueda, and H. L. Tanaka, 2018: Predictability of the 2012 great Arctic cyclone on medium-range timescales. *Polar Science*, **15**, 13–23.

Yamazaki, A., J. Inoue, K. Dethloff, M. Maturilli, and G. König-Langlo, 2015: Impact of radiosonde observations on forecasting summertime Arctic cyclone formation. *J. Geophys. Res.*, **120 (8)**, 3249–3273.

Zampieri, L., H. F. Goessling, and T. Jung, 2018: Bright prospects for Arctic sea ice prediction on subseasonal time scales. *Geophys. Res. Lett.*, 1–8.

Zängl, G., and K. P. Hoinka, 2001: The tropopause in the polar regions. *J. Climate*, **14 (14)**, 3117–3139.

Zarzycki, C. M., M. N. Levy, C. Jablonowski, J. R. Overfelt, M. A. Taylor, and P. A. Ullrich, 2014: Aquaplanet experiments using CAM's variable-resolution dynamical core. *J. Climate*, **27 (14)**, 5481–5503.

Zhang, C., Y. Wang, and K. Hamilton, 2011a: Improved representation of boundary layer clouds over the southeast Pacific in ARW-WRF using a modified Tiedtke cumulus parameterization scheme. *Mon. Wea. Rev.*, **139 (11)**, 3489–3513.

Zhang, J., R. Lindsay, A. Schweiger, and I. Rigor, 2012: Recent changes in the dynamic properties of declining Arctic sea ice: A model study. *Geophys. Res. Lett.*, **39 (20)**.

Zhang, J., R. Lindsay, A. Schweiger, and M. Steele, 2013: The impact of an intense summer cyclone on 2012 Arctic sea ice retreat. *Geophys. Res. Lett.*, **40 (4)**, 720–726.

Zhang, J., and D. Rothrock, 2003: Modeling global sea ice with a thickness and enthalpy distribution model in generalized curvilinear coordinates. *Mon. Wea. Rev.*, **131 (5)**, 845–861.

Zhang, S., M. Harrison, A. Rosati, and A. Wittenberg, 2007: System design and evaluation of coupled ensemble data assimilation for global oceanic climate studies. *Mon. Wea. Rev.*, **135 (10)**, 3541–3564.

Zhang, Y., D. J. Seidel, J.-C. Golaz, C. Deser, and R. A. Tomas, 2011b: Climatological characteristics of Arctic and Antarctic surface-based inversions. *J. Climate*, **24 (19)**, 5167–5186.

Zhao, C., and Coauthors, 2016: Exploring the impacts of physics and resolution on aquaplanet simulations from a nonhydrostatic global variable-resolution modeling framework. *Journal of Advances in Modeling Earth Systems*, **8 (4)**, 1751–1768.

Appendix A

Derivation of Ertel's potential vorticity

We begin with Cauchy's equation of motion (at small but still differentiable scale) for a parcel subject to body and surface forces in an inertial frame of reference

$$\rho \frac{Du_i}{Dt} = \rho g_i + \frac{\partial \tau_{ij}}{\partial x_j} \tag{A.1}$$

for dry air density ρ, velocity u, time t, gravity g, stress τ, and spatial axis x. Note that anything else in the fluid (e.g. hydrometeors) must act as a passive tracer in terms of momentum. Assuming Newtonian stress-strain and Stokes' hypothesis for pressure,

$$\rho \frac{Du_i}{Dt} = \rho g_i - \frac{\partial p}{\partial x_i} - \frac{2}{3}\frac{\partial}{\partial x_i}(\mu \frac{\partial u_i}{\partial x_j}) + 2\frac{\partial}{\partial x_j}(\mu e_{ij}) \tag{A.2}$$

for pressure p, viscosity μ, and strain tensor e. Since viscosity isn't constant spatially, the last two terms are difficult. We rewrite the viscous terms

$$\rho \frac{Du_i}{Dt} = \rho g_i - \frac{\partial p}{\partial x_i} + F_i \tag{A.3}$$

into a so-called frictional forcing F, further parameterized in applications.

Incorporating the "vector invariant" form of advection and gravitational potential Π,

$$\frac{\partial u}{\partial t} + (\nabla \times u) \times u + \nabla((u \cdot u)/2) = -\nabla \Pi - \frac{1}{\rho}\nabla p + F/\rho \tag{A.4}$$

Now take $\nabla\times$ (A.4), noting that it's a linear operation, $\nabla \times \nabla \text{scalar} = 0$, and $\nabla \times u = \omega$.

$$\frac{\partial \omega}{\partial t} + \nabla \times (\omega \times u) + \cancel{\nabla \times \nabla((u \cdot u)/2) + \Pi)} = -\nabla \times (\frac{1}{\rho}\nabla p) + \nabla \times (F/\rho) \tag{A.5}$$

$$\frac{\partial \omega}{\partial t} + \omega \nabla \cdot u - \cancel{u \nabla \cdot \omega} + (u \cdot \nabla)\omega - (\omega \cdot \nabla)u = -\nabla \times (\frac{1}{\rho}\nabla p) + \nabla \times (F/\rho) \tag{A.6}$$

$$\frac{D\omega}{Dt} + \omega \nabla \cdot u - (\omega \cdot \nabla)u = \frac{\nabla \rho \times \nabla p}{\rho^2} - \frac{1}{\rho}\cancel{\nabla \times \nabla p} + \nabla \times (F/\rho) \tag{A.7}$$

If there are no sources or sinks of mass for the parcel,

$$\frac{D\rho}{Dt} = -\rho \nabla \cdot u \tag{A.8}$$

a la Reynolds' Transport Theorem.

Now, following the derivation in Pedlosky (2013) (apparently originating with a collaboration between Ertel and Rossby in the 1930s):

$$\frac{D\omega}{Dt} - \frac{\omega}{\rho}\frac{D\rho}{Dt} - (\omega \cdot \nabla)u = \frac{\nabla \rho \times \nabla p}{\rho^2} + \nabla \times (F/\rho) \tag{A.9}$$

$$\frac{D}{Dt}\frac{\omega}{\rho} = \frac{1}{\rho}\frac{D\omega}{Dt} - \frac{\omega}{\rho^2}\frac{D\rho}{Dt} = (\frac{\omega}{\rho} \cdot \nabla)u + \frac{\nabla \rho \times \nabla p}{\rho^3} + \frac{1}{\rho}\nabla \times (F/\rho) \tag{A.10}$$

Consider λ s.t. $\frac{D\lambda}{Dt} = \psi$. For example, for potential temperature $\lambda = \theta, \psi = \frac{D\theta}{Dt}$ and $\psi = 0$ iff adiabatic. Then,

$$\frac{D}{Dt}\frac{\partial\lambda}{\partial x_i} = \frac{\partial}{\partial t}\frac{\partial\lambda}{\partial x_i} + u_j\frac{\partial}{\partial x_j}\frac{\partial\lambda}{\partial x_i} = \frac{\partial}{\partial x_i}\frac{\partial\lambda}{\partial t} + u_j\frac{\partial}{\partial x_i}\frac{\partial\lambda}{\partial x_j} \tag{A.11}$$

$$= \frac{\partial}{\partial x_i}\frac{\partial\lambda}{\partial t} + \frac{\partial}{\partial x_i}u_j\frac{\partial\lambda}{\partial x_j} - \frac{\partial u_j}{\partial x_i}\frac{\partial\lambda}{\partial x_j} = \frac{\partial}{\partial x_i}\frac{D\lambda}{Dt} - \frac{\partial u_j}{\partial x_i}\frac{\partial\lambda}{\partial x_j} \tag{A.12}$$

$$= \frac{\partial\psi}{\partial x_i} - \frac{\partial u_j}{\partial x_i}\frac{\partial\lambda}{\partial x_j} \tag{A.13}$$

$$\omega_i\frac{D}{Dt}\frac{\partial\lambda}{\partial x_i} = \omega_i\frac{\partial\psi}{\partial x_i} - \omega_i\frac{\partial u_j}{\partial x_i}\frac{\partial\lambda}{\partial x_j} \rightarrow \omega\cdot\frac{D}{Dt}\nabla\lambda = \omega\cdot\nabla\psi - \omega\cdot\nabla u\cdot\nabla\lambda \tag{A.14}$$

Now take $\nabla\lambda\cdot(A.10) + (A.14)/\rho$

$$\nabla\lambda\cdot\frac{D}{Dt}\frac{\omega}{\rho} + \frac{\omega}{\rho}\cdot\frac{D}{Dt}\nabla\lambda = \nabla\lambda\cdot(\frac{\omega}{\rho}\cdot\nabla)u + \nabla\lambda\cdot\frac{\nabla\rho\times\nabla p}{\rho^3} + \tag{A.15}$$
$$\nabla\lambda\cdot\frac{1}{\rho}\nabla\times(F/\rho) + \frac{\omega}{\rho}\cdot\nabla\psi - \frac{\omega}{\rho}\cdot\nabla u\cdot\nabla\lambda$$

$$\frac{D}{Dt}(\frac{\omega}{\rho}\cdot\nabla\lambda) = \frac{\omega}{\rho}\cdot\nabla\psi + \nabla\lambda\cdot\frac{\nabla\rho\times\nabla p}{\rho^3} + \frac{\nabla\lambda}{\rho}\cdot\nabla\times(F/\rho) \tag{A.16}$$

For $\lambda = \lambda(\rho, p), \nabla\lambda\cdot\nabla\rho\times\nabla p = 0$. For $T = T(\rho, p)$ as in the ideal gas law, $\lambda = \theta$ is one such choice. Finally,

$$\frac{D}{Dt}(\frac{\omega}{\rho}\cdot\nabla\theta) = \frac{\omega}{\rho}\cdot\nabla\frac{D\theta}{Dt} + \frac{\nabla\theta}{\rho}\cdot\nabla\times(F/\rho) \tag{A.17}$$

Appendix B

Summary of personal contributions

Development of the tools used in this work benefited from previous work and acknowledged collaborations. As requested, a summary of my personal contributions is included below.

For TPVTrack, I am the developer and main tester. For MPAS-A, I began in 2012 as an early tester. Through use, I helped with identifying or fixing bugs in the grid generation code, sea ice and sea surface temperature initialization/updating, transport of additional tracers, and radiation data files. I also generated new grids (e.g., a mid-latitude refined mesh and bipolar mesh with refinement over the Arctic and Antarctic). Building from Cavallo and Hakim (2009), I implemented potential vorticity diagnostics and budgets. I designed and implemented the TPV modifications. For MPAS-A within CESM, I contributed to initialization strategies and setting up the "trigrid" configuration where the land model is on a different grid than the atmosphere. I also added the potential vorticity diagnostics and TPV modifications, adapted from the stand-alone MPAS-A.